Snow Properties Retrieval Using Passive Microwave Observations

by

Nastaran Saberi

A thesis
presented to the University of Waterloo
in fulfillment of the
thesis requirement for the degree of
Doctor of Philosophy
in
Geography

Waterloo, Ontario, Canada, 2019

Examining Committee Membership

The following served on the Examining Committee for this thesis. The decision of the Examining Committee is by majority vote.

External Examiner: Jennifer M. Jacobs
Professor, Dept. of Civil and Environmental Engineering,
University of New Hampshire

Supervisor: Richard Kelly
Professor, Dept. of Geography Environmental Management,
University of Waterloo

Internal Members: Ellsworth LeDrew
Professor, Dept. of Geography Environmental Management,
University of Waterloo
Claude Duguay
Professor, Dept. of Geography Environmental Management,
University of Waterloo

Internal-External Member: Andrea Scott
Assistant Professor, Dept. of System Design,
University of Waterloo

Other Member(s): Chris Derksen
Research Scientist, Cryosphere and Climate Interaction,
Environment and Climate Change Canada

I hereby declare that this document consists of works that I was the sole author and the works I was a co-author. Please refer to the statement of contribution for details. This is a true copy of the thesis, including any required final revisions, as accepted by my examiners.

I understand that my thesis may be made electronically available to the public.

Abstract

Seasonal snow cover, the second-largest component of the cryosphere, is crucial in controlling the climate system, through its important role in modifying Earth's albedo. The temporal variability of snow extent and its physical properties in the seasonal cycle also make up a significant element to the cryospheric energy balance. Thus, seasonal snow cover should be monitored not only for its climatological impacts but also for its role in the surface-water supply, ground-water recharge, and its insolation properties at local scales. Snowpack physical properties strongly influence the emissions from the substratum, making feasible snow property retrieval by means of the surface brightness temperature observed by passive microwave sensors. Depending on the observing spatial resolution, the time series records of daily snow coverage and a snowpacks most-critical properties such as the snow depth and snow water equivalent (SWE) could be helpful in applications ranging from modeling snow variations in a small catchment to global climatologic studies. However, the challenge of including spaceborne snow water equivalent (SWE) products in operational hydrological and hydroclimate modeling applications is very demanding with limited uptake by these systems. Various causes have been attributed to this lack of uptake but most stem from insufficient SWE accuracy. The root causes of this challenge includes the coarse spatial resolution of passive microwave (PM) observations that observe highly aggregated snowpack properties at the spaceborne scale, and inadequacies during the retrieval process that are caused by uncertainties with the forward emission modeling of snow and challenges to find robust parameterizations of the models. While the spatial resolution problem is largely in the realm of engineering design and constrained by physical restrictions, a better understanding of the whole range of retrieval methodologies can provide the clarity needed to move the thinking forward in this important field.

Following a review on snow depth and SWE retrieval methods using passive microwave remote sensing observations, this research employs a forward emission model to simulate snowpacks emission and compare the results to the PM airborne observations. Airborne radiometer observations coordinated with ground-based *in situ* snow measurements were acquired in the Canadian high Arctic near Eureka, NT, in April 2011. The observed brightness temperatures (T_b) at 37 GHz from typical moderate density dry snow in mid-latitudes decreases with increasing snow water equivalent (SWE) due to the volume scattering of the ground emissions by the overlying snow. At a certain point, however, as SWE increases, the emission from the snowpack offsets the scattering of the sub-nivean emission. In tundra snow, the Tb slope reversal occurs at shallower snow thicknesses. While it has been postulated that the inflection point in the seasonal time series of observed Tb V 37 GHz of tundra snow is controlled by the formation of a thick wind slab layer, the simulation of this effect has yet to be confirmed. Therefore, the Dense Media Radiative Transfer Theory for Multi Layered (DMRT-ML) snowpack is used to predict the passive microwave response from airborne observations over shallow, dense, slab-layered tundra snow. The DMRT-ML was parameterized with the *in situ* snow measurements using a two-layer snowpack and run in two configurations: a depth hoar and a wind slab dominated pack.

Snow depth retrieval from passive microwave observations without *a priori* information is a highly underdetermined system. An accurate estimate of snow depth necessitates *a priori* information of snowpack properties, such as grain size, density, physical temperature and stratigraphy, and, very importantly, a minimization of this a prior information requirement. In previous studies, a Bayesian Algorithm for Snow Water Equivalent (SWE) Estimation (BASE) have been developed, which uses the Monte Carlo Markov Chain (MCMC) method to estimate SWE for taiga and alpine snow from 4-frequency ground-based radiometer T_b. In our study, BASE is used in tundra snow for datasets of 464 footprints in the Eureka region coupled with airborne passive microwave observations—the same field study that forward modelling was evaluated. The algorithm searches optimum posterior probability distribution of snow properties using a cost function between physically based emission simulations and T_b observations. A two-layer snowpack based on local snow cover knowledge is assumed to simulate emission using the Dense Media Radiative Transfer-Multi Layered (DMRT-ML) model.

Overall, the results of this thesis reinforce the applicability of a physics-based emission model in SWE retrievals. This research highlights the necessity to consider the two-part emission characteristics of a slab-dominated tundra snowpack and suggests performing inversion in a Bayesian framework.

Acknowledgements

I would like to express my gratitude to my PhD advisor, Dr. Richard Kelly for his support during the roller coaster of emotions in my PhD life. I never felt I was alone in this challenging journey, because by encouraging me to build on tiny achievements, he helped me to reach my wildest goals. I would also like to my PhD committee members Drs. Ellsworth Ledrew (Geography and Environmental Management), Claude Duguay (Geography and Environmental Management), Chris Dersken (Environment Canada), and Andrea Scott (System Design) for their continued support.

Thank you to my young scholarly friends in The Interdisciplinary Centre on Climate Change (IC3) group and in particular, Vicky Vanthof, Qinghuan Li, and Margot Flemming.

This research was supported by the Japan Aerospace Exploration Agency through the GCOM-W1/AMSR2 project and by the National Science and Engineering Research Council of Canada. The Eureka snow and airborne radiometer measurements were supported by Environment Canada as part of the PAMARCMIP 2011 campaign. Thanks to Chris Derksen, Peter Toose, Arvids Silis, Stephen Howell and Dave Halpin for the work in collecting the snow survey data, and Mike Harwood, Walter Strapp and Ken Asmus for their help in conducting the airborne radiometer surveys.

Dedication

This dissertation is dedicated to my beloved mother Shahnaz, my lovely husband Amin, and my little son Artin.

Table of Contents

List of Tables

List of Figures

Abbriviations and Nomenclature

ε” Imaginary component of complex relative permittivity

ε' Real component of complex relative permittivity

AMSR-E Advanced Microwave Scanning Radiometer for EOS

AMSR2 Advanced Microwave Scanning Radiometer 2

DMRT Dense Media Radiative Transfer

DMRT-ML Dense Media Radiative Transfer-Multi layered

HUT Helsinki University of Technology

IFOV Instantaneous Field Of View

MCMC Monte Carlo Markov Chain

PM Passive Microwave

QCA Quasi Crystalline Approximation

QCA-CP Quasi Crystalline Approximation-Coherent Potential

SD Snow Depth

SSA Specific Surface Area

SSMI Special Sensor Microwave/Image

SWE Snow Water Equivalent

Statement of Contributions

Along with the general introductory chapter, this manuscript-style thesis contains three papers that have been published in or under review by peer-reviewed journals. The first paper, Chapter 4, a literature review paper on Snow Depth (SD) retrievals, has been submitted to International Journal of Remote Sensing. The second paper, now published in Remote Sensing journal, is presented in Chapter 5. The third paper, on inversion problem, is submitted to IEEE Transactions on Geoscience and Remote Sensing journal.

All of the presented works are the result of collaborations between the author of this thesis—as a corresponding writer and main contributor—and other significant co-authors. Chapter 4 is a collaborative work by Nastaran Saberi, who designed the study framework; Richard Kelly, who co-developed the framework of this study and significantly revised the manuscript written by Nastaran Saberi; and, Margot Flemming and Qinghuan, who contributed valuable thoughts throughout the writing process. The original written manuscript was created by Nastaran Saberi and the text has been edited by Richard Kelly.

Chapter 5 is the result of a collaboration for which, Nastaran Saberi analyzed the data and designed the study framework of study; Chris Derksen and Peter Toose designed the experiments; Peter Toose performed the experiments; Richard Kelly co-developed the framework and significantly revised the manuscript written by Nastaran Saberi; and, Alex Roy, Chris Derksen, and Peter Toose contributed valuable edits and suggestions throughout the modeling and writing process. The original written manuscript and plots and maps are the work of Nastaran Saberi, with editing help by the coauthors.

Chapter 6 is again a collaborative work. Nastaran Saberi analyzed the data and designed the study framework; Richard Kelly co-developed the framework and significantly revised the manuscript written by Nastaran Saberi; and Jinmei Pan, Michael Durand, and Josline Goh contributed valuable suggestions throughout the modeling process. The original written manuscript and plots and maps have been created by Nastaran Saberi and the text has been edited by the coauthors.

All papers are reprinted in the form they were submitted for publication.

Chapter 1

General Introduction

1.1 Motivation

Snow cover affects the climate system through its important role in modifying the Earth's albedo. In addition, modeling a hydrological system at local to regional scales for various applications such as snow runoff models requires accurate snow cover extent (SCE) and snow depth (SD) as controlling geophysical variables. Seasonal snow cover dynamics necessitates the mapping and measuring of snow properties in short time-steps so as to obtain accurate modeling and conclusively address the importance of the physical property retrieval of seasonal snow cover.

Remote sensing provides frequent observations at small scales, allowing modeling of the snowpack variability at these scales [54], whereas this variability cannot be captured by relying only on ground-based measurements. Among various available sensors and platforms for earth surface monitoring, Passive Microwave (PM) radiometry has been known as a powerful tool for snow mass retrieval for more than four decades. Extensive ground-based radiometry of a snowpack in different conditions (e.g., [139, 171, 155]) has resulted in current physical properties emission models for snowpack. Furthermore, the availability of *in situ* measurements helps to evaluate emission models' accuracy and sensitivity to each parameter. Despite the extensive efforts of researchers to provide accurate SWE retrieval using PM, current SWE products still do not meet the minimum operational accuracy requirement for hydrological applications (±15%)[14].

Emission models of snowpacks have been employed in various ground-based experiments; however, only a limited number of studies focus on retrievals using remote sensing observations through physical emission models. The scaling process is another challenge that impacts the accuracy of retrievals. Generalizing *in situ* measurements for snowpack emission modeling and for the evaluation of retrievals is a very important analysis that is mostly undermined. Several studies have confirmed that grain size is the most-influential component of the microwave signature in emission modeling. Using an appropriate grain size and growth rate to represent snowpack evolution leads to improved simulations. In addition, a snowpack is not a homogeneous medium, and its microstructural properties vary from layer to layer. This heterogeneity should be considered in a remote sensing observation footprint. On the other hand, adding unnecessary details of the stratigraphy to the model should be avoided as it leads to a high correlated simulations and observations, with no real justification.

The complexities of applicable theories in physical emission models are barriers for hydrologists to couple their knowledge of snow hydrology to electromagnetic modeling. The same issue has arisen with Machine Learning (ML) techniques applied as inversion methods to observations. To date, a tractable and reproducible retrieval framework that integrates *in situ* measurements, a snowpack microstructure using climatology information or field measurements, and PM observations has not been proposed. This work delivers a thorough and critical review of retrievals, then, using extensive datasets it focuses on the applicability of a forward emission model and an innovative inversion approach to support the present need for snow property retrieval.

1.2 Research questions

The research questions that have formed the foundation and direction of this research, and that individually are the focus of three research papers are as follows:

1. Building on the literature devoted to estimating SD and SWE using spaceborne observations, how passive microwave observations are used to estimate SWE in terrestrial snow-covered landscapes? This inquiry highlights existing explanations of microwave and ice particles interactions, and addresses limitations of available retrieval methodologies.

2. In a case study having airborne/spaceborne observations of snowpacks coinciding with intensive *in situ* measurements, under what circumstances can we effectively simulate emissions using a forward emission model. How can field knowledge be integrated into the emission modeling, and how can the *in situ* measurements be generalized to suit the scale of observations?

3. How can we estimate snowpack properties using PM remote sensing observations and a probabilistic retrieval approach based on generalized prior information of a snowpack?

1.3 Research Scope

Various methods are available for mapping snow properties. The approaches to characterizing terrestrial seasonal snow accumulation, SCE and SWE, been developed largely using *in situ* measurements, numerical models, and remote sensing observations. Among remote sensing methods, several numerical models, including empirical, semi-empirical and physically-based models have been developed to estimate SWE from passive microwave remote sensing instruments. This current research focuses on developing an approach for snow properties retrieval using spaceborne radiometry as the main source of observations.

1.4 Objectives

A primary goal has been set to develop an approach for using a physical emission model for snow properties retrieval, specifically in tundra snow, with spaceborne radiometry as the main source of observations. This approach involves understanding the generalization process of snowpack key parameters in the physical emission model and the application of inverse modeling to retrieve snowpack physical properties such as snow water equivalent (SWE). The three core elements of this SWE retrieval are:

1. Through an extensive literature review, to study available methodologies for retrieving snow mass from PM observations, while critically reviewing and discussing research gaps in SWE retrieval frameworks;
2. Evaluating applicability of forward emission modeling at airborne radiometry scales.
3. To employ a Bayesian inversion method to derive SWE from PM observations.

1.5 Thesis structure

This manuscript-based thesis is structured as seven chapters. This current (first) chapter presents the general introduction, with the rational and defined objectives of the work.

Chapter 2 provides an understanding of seasonal snow physical properties as a requirement to understand and develop methods to retrieve snowpack properties using passive microwave remote sensing observations. Chapter 3 delivers the fundamental of PM remote sensing as well as reviewing basics of emission modeling of snowpack. These background chapters provide fundamentals of the work while connecting the remaining chapters.

The forth chapter describes and discusses SWE retrieval methods using passive microwave remote sensing. This chapter has been submitted to International Journal of Remote Sensing.

Chapter 5 addresses the second objective of this thesis, with an explanation of the ground-based datasets in the Eureka region that are used to model the passive microwave response of shallow, dense, slab-layered tundra snow. PM airborne and spaceborne observations are employed to evaluate the modeling accuracy. This work has been published in the peer-reviewed Journal Remote Sensing: Saberi, N., Kelly, R., Toose, P., Roy, A., & Derksen, C. (2017). Modeling the Observed Microwave Emission from Shallow Multi-Layer Tundra Snow Using DMRT-ML. Remote Sensing, 9(12), 1327.

Chapter 6 addresses the third objective of this thesis with the application of an inversion method of Monte Carlo Markov Chain (MCMC) to employ the generalized microstructure of snowpack in the same study area in the form of prior information. This paper has been submitted to IEEE Transactions on Geoscience and Remote Sensing journal.

The final chapter (chapter 7) summarises the research, and discusses its limitations as well as future directions for applied research. It should be noted that all three papers are presented in their original published or submitted format, which leads to some repetition of fundamental introductory material and common methodological discussions.

Chapter 2

Seasonal terrestrial snowpacks

Understanding the processes controlling a snowpack and its physical stages during the accumulation and melt seasons provides knowledge for emission modeling of the snowpack in snow-affected watersheds. Modeling microwave and snow grains interactions in a given snowpack allows retrieving snowpack properties using remote sensing (RS) observations at frequency channels that are sensitive to changes in snowpack properties. This chapter provides a general understanding of seasonal snow physical microstructure and its evolution. This knowledge can help in better understanding and therefore developing better methods to retrieve snowpack properties using PM observations.

2.1 Snow crystal morphology - in the atmosphere

Snow crystals in the atmosphere emerge in different structures. A general classification of snow crystals includes dendrites, plates, needles and columns. These different structures are mainly controlled by temperature and humidity. Pioneer scientists in snow crystal morphology studies, Nakaya and Marshall [147], presented a comprehensive morphology diagram of different crystalline structures' formation, gained using laboratory experiment. They concluded that this morphology is a function of the temperature and excess vapor density that is required to keep snow crystals in an equilibrium condition. Figure 2.1 shows the cloud temperature and supersaturation conditions required for different snow crystals formations in the atmosphere.

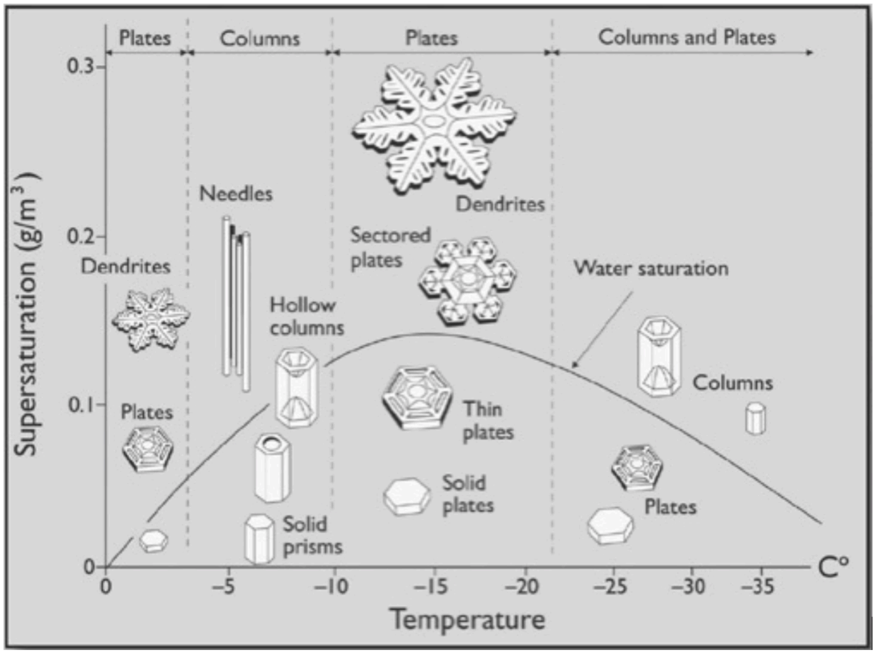

Figure 2.1: Morphology of snow crystals in the air as a function of temperature and supersaturation [125]

2.2 Snow grain morphology - on the ground

A snowpack is a porous medium consisting of ice particles and air at a temperature below the melting point of ice. As the season progresses, at the melting point, the snowpack properties alter to a state containing water in the spaces among granules [44]. A dry snowpack is not a homogeneous medium, and a stratigraphy exists in its structure. Precipitated snowflakes' physical characteristics are more or less similar, but grain shapes and sizes change rapidly after accumulation and settling due to gravity, wind and metamorphism. Each layer contains different grain shapes and sizes, densities, temperatures, cohesions, hardnesses and liquid water content (LWC). Studying snowpack-microwave interactions requires knowledge of the snow properties in each layer to model wave interactions during transformations.

The need for a united language for snow measurements and classification of grain shapes has resulted in the international classification for seasonal terrestrial snow [31, 235]. Morphological classification shapes with three to five subclasses [235][1], included rounded grains, faceted crystals, depth hoar, surface hoar, melt forms and ice formations. Snow grains are subclassified as precipitation particles, decomposing and fragmented precipitation particles, rounded grains, faceted crystals, cup-shaped crystals and depth hoar, feathery crystals, ice masses, surface deposited and crusts, and wet grains. Almost all of these crystal shapes are formed by metamorphic processes.

Snowpack metamorphism imposes changes in the microstructural properties of the snowpack. Coupling *a priori* knowledge of a multi-layered snowpack and its evolution to PM remote sensing observations increases the accuracy of retrievals. The main characteristics and physical processes involved in the formation of snow layers are explained next.

2.2.1 Evolution of terrestrial seasonal snowpack

The accumulation of precipitated snowflakes, the resulting snowpack densification and snow flake arm breakoffs due to gravity and then redistribution by wind, are accompanied by rapid transitions of the snowpack hydrological and microstructural properties. This transition changes the snowpack structure, grain shape, size, cohesion and liquid water content dynamically [31, 157]. Thermodynamic processes with key controllers of thermal conductivity and heat capacity in a snowpack determine snow evolution throughout a

---

[1] International classification of snow was updated later by Fierz et al. [62].

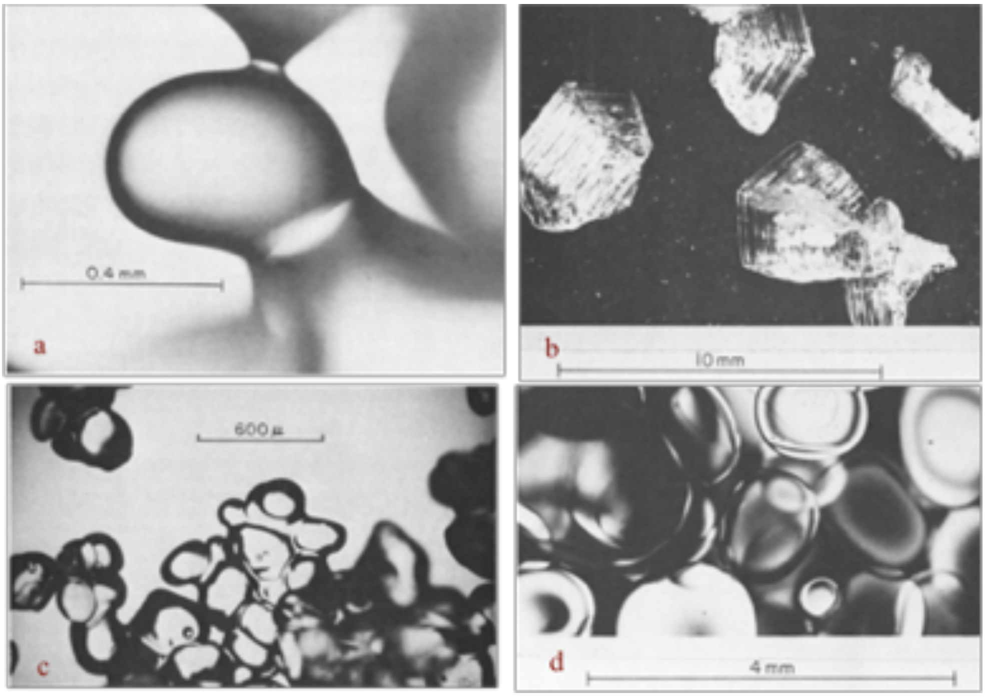

Figure 2.2: (a) Dry snow in equilibrium state. (b) Dry snow in kinetic growth condition. (c) Tightly packed snow crystals in wet snow low LWC. (d) Wet snow with high LWC containing rounded ice particles [30, 31]

season. Furthermore, in a snowpack whose temperature is generally close to the triple point—where all three phases exist in the snowpack, the temperature is 0.01, and vapor pressure is 6.1112 hPa—there is a dynamic mass exchange among the ice, air and water [7]. This evolution is explained by metamorphism in three types: destructive, constructive and melt [31]. Considering a snowpack as dry or wet depending on whether it is in a melting condition, dry snow undergoes the first two, but wet snow only undergoes the metamorphic process of melt. Rounded and faceted grains as a result of metamorphic processes can be seen in a dry snowpack, while wet snow contains either packed clusters of grains with lower LWC or rounded independent particles with high LWC of the snowpack [30, 31]. These four states are shown in Figure 2.2.

As a result of limitations in brightness temperature sensitivity to the physical properties of wet snow [155, 154], this document considers only dry snowpack in emission modeling and SWE retrieval techniques. Therefore, only the processes during destructive and constructive metamorphism are reviewed.

Destructive metamorphism

In an equilibrium state between ice and air in a dry snowpack, when there is a quasi-uniform temperature in the snowpack, mass exchange between ice and air is facilitated by the presence of vapor saturation [7, 157]. This vapor pressure in a dry snowpack is present as a result of a large specific area of ice and air interfaces. Due to higher vapor pressure around convex grains than concave ones, a local pressure gradient is created. Vapor diffusion towards concave areas is generated as a result of this pressure gradient. This vapor diffusion is compensated for by sublimation in convex regions and deposition in concave ones, which together maintain the equilibrium condition [7, 32, 44, 157].

Destructive metamorphism is initiated approximately four days after snowpack accumulation, under a small temperature gradient, where the substratum's temperature minus air temperature at a one-centimeter depth is less than -0.25°/cm [31, 69]. The formation of round, well-bonded grains and grain growth at a slow rate (∼0.008 mm per day) are processes in this phase that result in snowpack densification [31].

Constructive metamorphism

Under a large temperature gradient condition, higher than -0.25°/cm, constructive (kinetic growth) metamorphism takes place [41, 196]. In this process, a fast growth rate forms faceted crystals and depth hoar. This grain growth results from a high temperature and vapor pressure gradient. Vapor diffusion toward colder crystals is partially compensated for by sublimation from warmer and recrystallization in colder regions at the base or top layers of the snowpack (while the top layer of snow is cold, surface hoar is formed) [7]. As a result of this kinetic growth condition, the specific area decreases. Spherical representation of grains is not valid for faceted and depth hoar layers, and these grain types cause more ambiguity if spherical grains are assumed in an emission model. Specific surface area as a grain representation can partially solve this problem [158].

Transformations between the six main classes from international snow classification [62]—in the presence of temperature gradient and liquid water content—are summarized by Armstrong and Brun [7] and presented in Figure 2.3. Fresh snow with more convex surfaces under a low temperature gradient (∼-0.05°/cm) metamorphoses to rounded, decomposed and fragmented particles. A sustained low-temperature gradient condition forms rounded grains. Under a high temperature gradient (higher than -0.15°/cm), faceted crystals and then depth hoar are formed. The cup-shaped crystals classified in melt forms by Fierz et al. [62] are transformed from rounded grains or depth hoar as a result of a high temperature gradient.

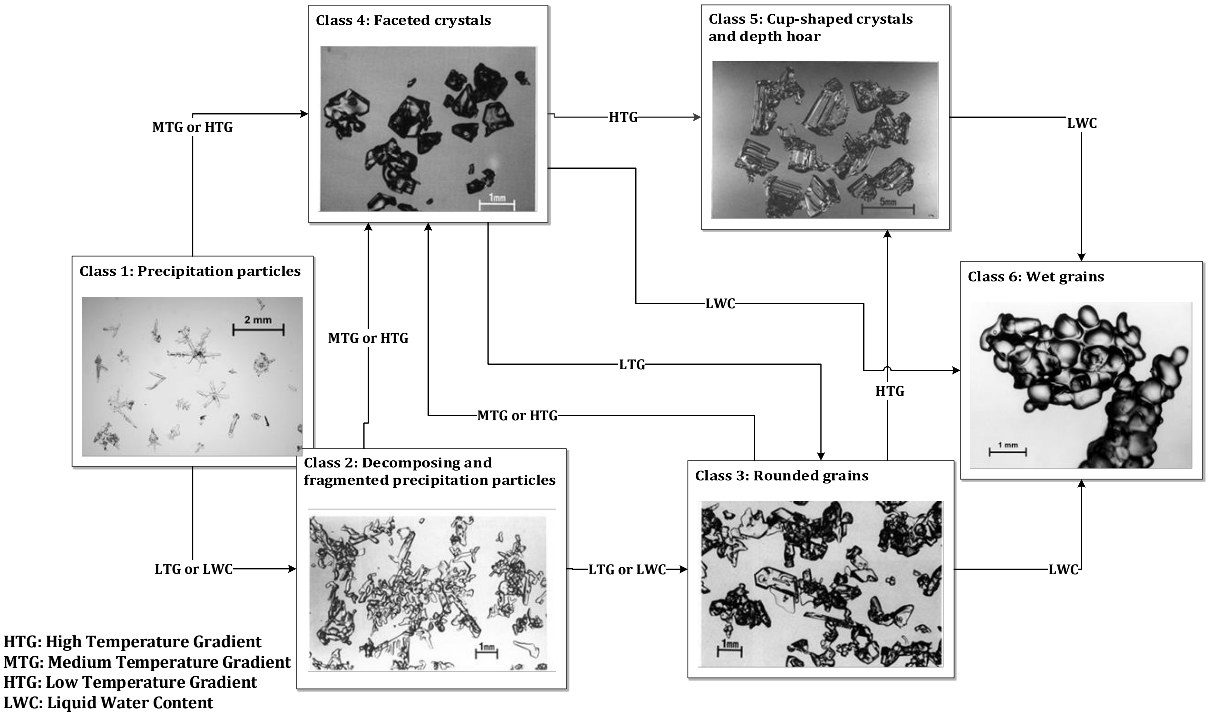

Figure 2.3: Snow metamorphic transformations under a low-to-high range of temperature gradients and the presence/non presence of liquid water content [7]

2.3 Tundra snow

The microstructure properties of layers in a settled seasonal snowpack are spatially variable. Precipitated snow, depending on wind distribution pattern, topography and land cover, accumulates in different depths and stratigraphy. This spatial heterogeneity is controlled by large-scale environmental factors such as wind and topography, and factors that influence internal snowpack evolution such as temperature gradients [195]. Sturm et al. [199] made a thorough study of seasonal snowpack classification based on physical properties of snow, including textural and stratigraphic characteristics, and also three climate variables—wind, precipitation and air temperature—as the most significant factors that control snowpack properties. Figure 2.4 shows an updated version of snow classes by Sturm et al. [200] in North America that is provided in an improved spatial resolution of 1 km compared to the 25 km grid cells in the previous version.

In the current research, snow properties retrieval is employed in a field study of arctic tundra snow. Based on Dichotomous key used by Liston [126], tundra snow places in a category of snowpacks in regions with low air temperature, low topographic variability and high wind speed. In terms of spatial variations, the peak of spatial variability in seasonal tundra snow—studied by Liston [126]—is reported as 100 m that is explained by wind drift structures at the same scale, whereas in a 10 m scale, uniform patterns are observed. Sturm and Benson [195] observed the stratigraphy of tundra snow using long profiles of snowpits and mapped these transects of multi-layered snowpacks to study heterogeneity of arctic snow layers. Using the 100 m long, stratigraphic profile generalized the arctic tundra as three layers of recent, wind lab, and depth hoar. Their analysis of stratified layers at 100 m to 100,000 m scales showed that: 1) heterogeneity of stratigraphy do not vary significantly at this range of scale, 2) landscape and weather interactions impact the stratigraphy at these scales, and 3) the method of cross correlating sparse snowpit data to represent stratigraphy, influences the accuracy of analysis at theses scales.

2.4 Summary

The microstructural properties of seasonal terrestrial snow as well as its evolution through the season have been reviewed. The snowpack evolution and transition to melt form is mostly controlled by temperature and the pressure gradient that is induced by the low conductivity of the snow medium. Positive values of net radiation and heat flux from the substratum (towards the snowpack surface) are the most important contributors to the temperature gradient between snow and the substratum. Understanding the snowpack

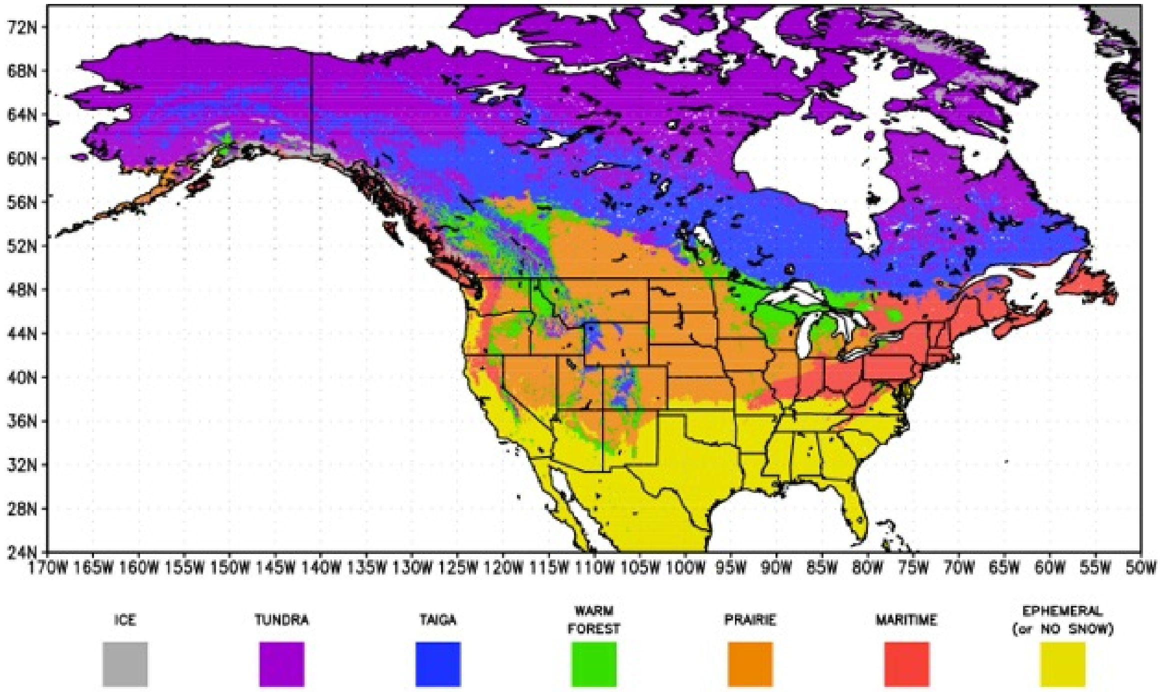

Figure 2.4: Sturm seasonal snow cover classes in North America based on climate variables and *in situ* measurements [200]

properties and metamorphic processes helps to improve our knowledge in modeling snow grains and microwave interactions. Furthermore, remote sensing observations provided by prior information such as grain size and density are significant data sources for snowpack physical properties retrieval. These prior information on grain growth and densification approximations are based on statistical analysis of extensive field measurements provided by historical climatologic variables. Further details on the importance of integrating prior information in the retrieval process is discussed in chapter 6.

Next chapter discusses fundamentals of emission processes through a snowpack, available emission models and their key elements, as well as introducing a few spaceborne radiometers.

Chapter 3

Passive microwave radiometry of snow

Almost a century after the first use of remote sensing technology in aerial photography, microwave remote sensing was implemented in the 1960s [218]. Penetration through clouds and observation during the night are two major benefits of using the microwave spectrum, which falls between ∼0.3-40 GHz (0.75-100 cm) for active systems and 1-200 GHz (15 mm-30 cm) for passive sensing techniques. In active systems, energy is transmitted and the backscattered energy from the earth is received; in the radiometry, emitted energy from the earth is observed.

Channel frequencies used in PM sensors are selected with respect to atmospheric windows that allow the wave to transmit and be observed by the sensor. On the other hand, for atmosphere related applications, the frequencies are used where atmospheric transmission is less. For instance, oxygen absorption is high at 60 GHz and 118.8 GHz [54] and frequencies in the 50-60 GHz range are useful for retrieving atmospheric temperatures [218]. In addition, using frequencies at ∼22 GHz and ∼180 GHz allows obtaining information about water vapor absorption due to the high amount of absorption in these frequencies [218, 54].

PM radiometry allows collecting information from the subsurface. Wave penetration in the medium or bulk material rises with wavelength increase, and the amount of penetration varies for different materials. Moisture decreases the penetration depth. For instance, 10 GHz penetration in sand or clay with a moisture level higher than 0.2 g/cm^3 is less than 1 cm; however, in dry sand or clay, penetration reaches to layers at 10 m depth. In longer waves of 1.3 GHz, the penetration depth in dry sand or clay is higher than 50 m [218]. Wave penetration in a snowpack follows the same principal. Figure 3.1, taken from Mätzler [139], shows penetration in a dry (upper figure) and a wet (lower figure) snowpack, respectively. Penetration depths are estimated using a microwave emission model of a multi-layered snowpack (MEMLS). The presented graphs show penetration depths of 1-10 m in dry snow and less than 10 cm in wet snow in frequency range of 10-37 GHz (the most sensitive range for surface properties retrieval using PM remote sensing).

Penetration depth shows the sensitivity of a frequency channel to a snowpack medium as a volume scatterer or its substratum as a surface scatterer. For properties retrieval of a deep snowpack, 10 & 37 GHz and 10 & 19 GHz are appropriate pair frequencies, while 19 & 37 GHz can be used for a shallower snowpack [100, 35].

This chapter discusses physical processes involved in PM remote sensing as well as observation systems with a focus on land brightness temperature estimation. Microwave interactions within a medium and the concept of radiative transfer theory are explained as an introduction for emission modeling, which is discussed accordingly.

3.1 Brightness temperature characteristics of a scene

Incident sun radiation absorbed by the Earth's surface is transformed into thermal energy and then emitted in the form of electromagnetic waves into the atmosphere. The theory of radiative transfer (RT) explains the aforementioned processes. This section discusses equations related to the brightness temperature observed by PM sensors, and electromagnetic interactions within the material (based on equations presented by [218]). It should be noted that brightness (K) in microwave terminology is the equivalent term for the radiance in optical remote sensing applications. This term defines the radiated power per unit of solid angle and unit of area (W $sr^{-1}m^{-2}$).

Assuming a radiometer with a receiving aperture and an emitting surface, the power P (Watt) intercepted by a receiver would be the product of the power's density by the aperture area. Considering an antenna's radiation-receiving pattern from all directions and a predefined frequency range, we have:

$$P = \frac{A_r}{2} \int_{f}^{f+\Delta f} \iint_{4\pi} B_f(\theta, \varphi) F_n(\theta, \varphi) d\Omega df \tag{3.1}$$

where B_f (W $m^{-2}sr^{-1}Hz^{-1}$) is the spectral brightness from emitting sources; F_n is the normalized emission pattern of the antenna, in both the θ and φ directions; $d\Omega$ is a differential solid angle in the direction of θ and φ. Therefore, the integral of the source brightness

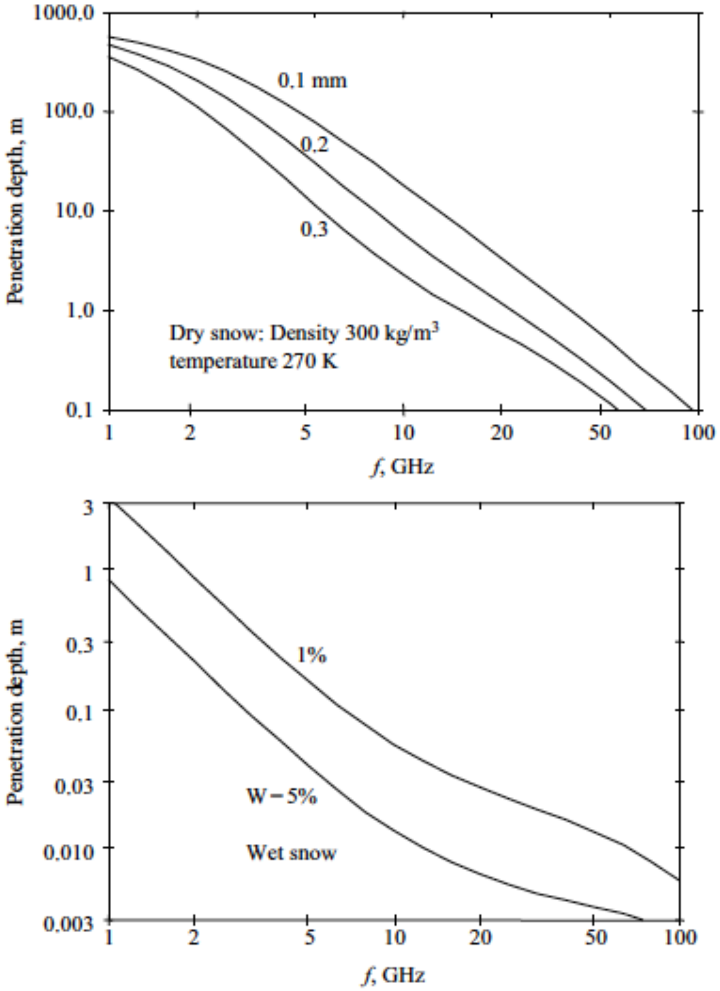

Figure 3.1: Penetration depth of different frequencies in dry snow, with exponential correlation lengths of 0.1 (fresh snow), 0.2 (fine-grained snow) and 0.3 (depth hoar) and in wet snow, with a correlation length of 0.3 [139]

multiplied by the radiation-receiving pattern by the antenna from all 4Π stradian directions and a predefined frequency range produces the power received by the antenna. Radiation can be explained either in waveform or by the quantum theory of radiation. In the latter concept, B_f for a blackbody, a perfect absorber and emitter, has been explained by Plank's radiation law [218]:

$$B_f = \frac{2hf^3}{c^2}\left(\frac{1}{e^{hfKT} - 1}\right) \tag{3.2}$$

where h is the Plank's constant (6.63×10^{-34} J); f (Hz) is frequency; c is speed of light ($3\times108ms^{-1}$); T (K) is the blackbody equivalent radiometric temperature; and K is the Boltzmann's constant ($1.38\times10^{-23}Jk^{-1}$). A useful approximation of Plank's law for the microwave region with 1-3% deviation from Plank's formula is the Rayleigh-Jeans approximation [1], where $hf/kT << 1$, spectral brightness is driven by [2]

$$B_f = \frac{2f^2KT}{c^2} = \frac{2KT}{\lambda^2} \tag{3.3}$$

If B_f from equation 3.2 is inserted in 3.1, we can obtain the relation between the blackbody temperature and the power received by the antenna. The simplified formula results in a relation between the effective temperature observed by a receiver, which can be written as in Elachi and Van Zyl [54]:

$$P = KT_{eq}\Delta f \tag{3.4}$$

where T_{eq} is the effective temperature observed by the receiver. Assuming a lossless antenna and a blackbody, both inside a chamber, T_{eq} is the constant temperature of the blackbody and P is the power received by the lossless antenna [218]). For a natural material, an equivalent radiometric temperature for a blackbody T_b, brightness temperature, and a parameter to quantify the material's capability in emitting emissivity, ε is considered. Then, assuming an antenna with a gain pattern and a natural medium, T_{eq} is a function of surface temperature, normalized surface emissivity and normalized antenna gain [54]. The relation between surface physical temperature, surface emissivity, observed temperature,

---

[1] For short wavelengths where $hf/kT >> 1$, Wien radiation law is obtained: $B_f = \frac{2h}{c^2}f^3e^{-hf/kT}$

[2] Computing the integral of B_f over all frequencies, Stephan-Boltzmann law is obtained by $B = \frac{\sigma T^4}{\pi}$, where σ is the Stephan-Boltzmann constant and equals $5.673\times10^{-8}W.m^{-2}.K^{-4}.sr^{-1}$. This law explains that blackbody brightness is dependent to the fourth power of temperature.

and antenna gain pattern results in obtaining the emission properties of the surface. However, an observed temperature contains energy emitted from multiple sources. Modeling the contribution of other sources to obtain the surface emission component is discussed next.

3.2 Brightness temperature observations

For all materials, there is a direct relationship between the physical temperature and the brightness temperature radiation, which can be explained by the higher resonance in molecules at higher temperatures leading to more radiation. The emission quantity also depends on the geometric and dielectric properties (roughness and composition) of the medium or surface [218]. In PM remote sensing, the observed T_b sensitivity to the surface kinetic temperature is much less than its sensitivity to the surface composition or roughness [54]. This high sensitivity allows the modeling of surface physical properties using PM observations.

To model surface emissions using PM observations, assume a lossless sensor, an emitting surface, and the atmosphere between them. There are three observation sources: atmospheric self-emission (T_{UP}), terrain self-emission (T_{Surf}), and scattered downward atmospheric contribution (T_{SC}). The terrain self-emission and downwelling atmospheric contribution are attenuated by atmospheric loss, explained either by a loss factor (L_a) or atmospheric transmissivity ($e^{-\tau}$)[3]. Other contributors such as cosmic emission and emission by the background (to the target and then incident to the senor) can be disregarded according to relative magnitude assessment of the components [186]. Thus, the apparent temperature observed at the spaceborne PM radiometer is modeled as

$$T_{AP} = (R \times T_{SC} + (1 - R)T_{suff})\, e^{-\tau} + T_{up} \tag{3.5}$$

where R is the surface reflectivity, assuming that there is no transmissivity into the surface ($\varepsilon + R = 1$). The appropriate frequency channels located in microwave atmospheric windows (where atmospheric transmissivity τ is ∼1) are employed in surface-properties-retrieval methods using PM observations. Peaks of atmospheric absorption caused by water vapor and oxygen occur at 22.4 GHz & ∼180 GHz and 60 GHz & 118.8 GHz, respectively. At a temperature of 273 K and pressure of 0.1 bar, water vapor with a density of 1 gr m^{-3} has ∼0.001 dB km^{-1} absorption rate at ∼36 GHz, while at the higher pressure of 1 bar

---

[3] There is also cosmic emission contribution that is relatively very small.

(sea level), this absorption rises to ∼0.01 dB $km-1$ [54]. However, the atmospheric transmission at the frequency channels of interest (at 10 GHz, 19 GHz and 36 GHz) is higher than 95% [218]; in the distance between spaceborne sensors and earth, the atmosphere's impact should be considered.

Atmospheric contribution is estimated by temperature sounding, classified into three major groups: occultation, scattering, and emission, with respect to appropriate techniques for modeling atmosphere constituents' interactions with microwaves [54]. Atmospheric radiosound profiles at local scales can be used to calibrate surface properties retrieval by emission models. For instance, in experiments conducted by Picard et al. [155], satellite and ground based brightness temperature were compared using temperature and moisture radiosound profiles. This experiment was set up to evaluate an atmospheric model (self-emission and transmissivity of atmosphere) used in the Helsinki University of Technology (HUT) snow emission model. Atmospheric effect as an emitter and absorber in land observation frequencies was measured by Qiu et al. [163]. In this experiment, HUTRAD radiometry data, balloon sonde atmospheric data, and AMSR-E observation were used to obtain atmospheric contributions in snow emission modeling. The results show differences of ∼20 K for 36.5 GHz and ∼8 K for 19 GHz between HUTRAD and AMSR2 observations, which reflects the aggregated contribution of atmospheric upwelling emission and attenuation. Furthermore, variations of atmospheric contribution highlight the importance of atmospheric modeling at local scales.

An emission in a granular medium such as a snowpack is either absorbed or scattered by grains. Reflection, refraction and transmission are other wave interactions between distinct layers. The dielectric properties of a medium as well as its composition define its emissivity.

3.2.1 Emissivity

The emissivity of an object describes how close its radiation potential is to a blackbody radiation. It is obtained by

$$e(\theta, \phi) = \frac{B(\theta, \phi)}{B_{bb}} = \frac{T_{suf}(\theta, \phi)}{T} \tag{3.6}$$

where (θ,ϕ) is the direction; B is the brightness of a natural material; T_{surf} is its radiometric brightness temperature; B_{bb} is blackbody brightness; and T is its physical temperature[4]. Using brightness values of the same polarization, emissivity can be computed in that polarization. Due to emissivity's independency of physical temperature, using emissivity rather than brightness temperature to obtain a medium physical properties is highly preferable.

Considering downwelling sky radiation, T_{SC} from ground based measurements[5], for surface emissivity we have [139]:

$$e = \frac{T_{surf} - T_{sc}}{T_{phys} - T_{sc}} \tag{3.7}$$

where T_{phys} is the surface physical temperature. For a non-isothermal medium such as snow, dividing brightness temperature into physical temperature cannot derive emissivity. Snowpack emissivity is derived by using one minus the reflected fraction of sky in a downward direction under two different conditions, e.g. 100 K and 0 K [230]:

$$e_s = 1 - \frac{T_b\left(T_{sc} = 100K\right) - T_B\left(T_{sc} = 0K\right)}{100K} \tag{3.8}$$

Next, the dielectric properties of snow, the most important parameter in defining emissivity and wave interactions within the snowpack, are discussed.

Dielectric properties of snow

Microwave interactions in a medium are relevant to its geometrical structure and electromagnetic properties. The relative permittivity of a medium or its effective complex dielectric constant (often used in RS literature) is the ratio of polarization capability in the electric field to the response of a vacuum or free space to polarization in the same condition (vacuum complex dielectric constant equals 8.85×10^{-12} Farad.m^{-1}). In other words, relative permittivity explains the response of the medium to the electric charge by dipole reorientation of its positive poles aligned with the electric field direction and negative poles in the opposite direction. It also describes the flux amount after interactions with the medium by

$$D = \varepsilon_r \times E \tag{3.9}$$

---

[4] From the above equation, it is concluded that the emissivity of the ideal blackbody equals one, and a non-emitting material has zero emissivity.

[5] PAMIR and RASAM instruments have been used in extensive experiments, resulting in a data catalogue for modeling emissivity applications. It can be found in [139]- Appendix A: Surface emissivity data from microwave experiments at the University of Bern.

where $E(Vm^{-1})$ is the electric field and D is displacement field or out flux (Cm^{-2}) from a material with a permittivity of $\varepsilon_r(Fm^{-1})$. ε_r is defined in a complex form

$$\varepsilon_r = \varepsilon_r' + j\varepsilon_r'' \tag{3.10}$$

where ε' is the real part of permittivity, the polarization ability of a material to respond to an electromagnetic field, which describes the radiation scattering; $j^2 = -1$; and ε_r'' is the imaginary part of the dielectric constant—the dielectric loss factor that quantifies energy attenuation.

Assuming a layer of snowpack containing air, ice crystals, and liquid water, each particle has a special dielectric characteristic. Air/atmosphere has a permittivity that is close to one ($1 < \varepsilon_r < 1.001$) [133]. Water is a dielectric material due to its asymmetric negative and positive formation (oxygen and hydrogen, respectively) in an electric field ($\varepsilon_r \approx 40$ in $0°C$ at 10 GHZ). Ice has a very low dielectric loss and a permittivity of ∼3.1 that is independent of frequency.

In a simplified model where snowpack is considered as a homogenous medium, the snowpack dielectric constant is estimated by a weighted average of the air, ice, and water particles dielectric properties. Under a heterogeneous medium assumption, internal scattering is also considered [133]. In the case of dry snow, ice particles in the air as background are assumed, resulting in a simpler solution.

Empirical relations supported by different theories and derived by experiments [133, 34, 210] relate real and imaginary parts of ice and water permittivity to wave frequency and physical properties such as porosity, density and temperature. Dry snow experimental results by Hallikainen [85] have shown that permittivity in the range of 3-37 GHz is independent from temperature and has a linear relation with snow density ($\varepsilon_r' = 1 + 1.83\rho$). Similar empirical relations between dry snow permittivity and its density have been derived from different experimental studies (e.g., Mätzler [133] equation[6]). In terms of dielectric loss, dry snow can be considered transparent, as loss factor has been reported by Mätzler [133] to have very small impact (∼0.001), in the range of 3-37 GHz.

Next, is an introduction to radiative transfer theory, which supports the basis of emission modeling.

---

[6] $\varepsilon_r' = 1 + \frac{1.6\rho}{1-0.35\rho}$

3.2.2 Radiative Transfer Theory

Radiative transfer theory relates incident radiation to the sensor and transferred emitted radiation from the surface after it interacts with the medium. Using the radiative transfer equations to obtain the radiance at a certain location is under the assumption of incoherent interactions between wave and matter. Interactions between radiation and the matter include emission, extinction (scattering and absorption) and transmission [218]. A differential equation 3.11 that relates brightness increment dB to extinct and emitted brightness increments through a cylindrical object defines the radiation transfer. Then expansion of this equation with the introduction of other parameters such as source functions and an optical length results in deriving the equation of transfer.

$$\frac{dB}{d\tau} + B = J \tag{3.11}$$

In equation 3.11, J equals $(1-a)J_a + aJ_s$ ($a = K_s/K_e$ a ratio of scattering coefficient K_s to extinction coefficient K_e, J_a: absorbtion source function and J_s: scattering source function), $d\tau$ is an increment of optical depth and equals $k_e dr$ (d_r is an increment of distance in dB direction) [218].

The extinction coefficient (nepers.m^{-1}), also known as the power attenuation coefficient, defines energy loss through the medium, which can be in the form of scattering (Ks) or absorption ($K_a = K_e - K_s$) [218]. For a snowpack, these parameters, as well as the phase function[7] can be derived using different empirical, semi-empirical and theoretical models such as SFT (strong fluctuation theory), MEMLS (microwave emission of multi layered snowpack), DMRT (dense media radiative transfer), etc. The radiative transfer solution has also been included in these models. Depending on the model and background theories, different requirements are needed to compute the extinction and scattering coefficients; e.g., in DMRT theory, the dielectric properties of the snow are required.

Using the explained replacements and integration by distance, the solution for the scalar equation of transfer will be [218]:

$$B(r) = B(0)e^{-\tau(0,r)} + \int_0^r K_e(r')\,J(r')\,e^{-\tau(r',r)}dr' \tag{3.12}$$

where $B(r)$ is the brightness in a distance of r from defined zero coordinates in $\hat{r}$ direction; $B(0)$ is the brightness in the boundary; $K_e(r')J(r')dr'$ is the emission increment at r' in $\hat{r}$ direction; $e^{-\tau(r',r)}$ is the medium extinction between r' in the medium and $\hat{r}$ at the

---

[7] The phase function explains the angular distribution of a bodys radiation.

observation point, and $\tau(r', r)$ is the optical depth between r' and r. This equation explains that radiation from a layer of material consists of two terms: the first is substratum brightness multiplied by the extinction effect of the layer ($e^{-\tau(0,r)}$), and the second is scattered emission within the material.

To simulate the emission of a snowpack, one of the main steps is solving the equation of radiative transfer from the substratum up to the air and snow interface. Different radiative transfer models are available, based on assumptions and theories being used for computation of the equation unknowns such as the extinction, the scattering, phase functions, and transmission in each layer of the snowpack. Snowpack emission models are discussed in 3.3.

3.3 Radiative transfer modelling of a snowpack

Electromagnetic radiation passing through a dry snowpack medium can be modeled by scattering, absorption, reflection, refraction and transmission. Three different groups, empirical, semi-empirical and physical emission models, have been developed to estimate snowpack physical parameters. These models are selected due to being extensively applied in current studies, and the reasonable fit between emission simulations and the snowpack properties measurements using these models coupled with either spaceborne or ground-based radiometry observations (e.g. [176, 120, 204, 182]). This section reviews three snowpack emission models: the emission model of Helsinki University of Technology (HUT), the microwave emission model of layered snowpacks (MEMLS), and the dense media radiative transfer theory for a multi-layered snowpack (DMRT-ML). The first two can be classified as semi-empirical emission models as they employ empirical relations for some required inputs, while DMRT-ML is considered as a physical model [205]. A retrieval methodology using HUT model is explained to elaborate on an example for SWE retrieval method. Retrievals are discussed in the next chapter in more details.

Chosen emission models have been comparatively reviewed. In addition, snowpack grain modeling, as the most challenging component of an emission model, is studied to consider the influence of different representations for snowpack grains used in the discussed emission models.

3.3.1 HUT

The Helsinki University of Technology (HUT) snow emission model was developed by Pulliainen et al. [162]. This semi-physical two flux-model is coupled to a Bayesian approach to obtain the maximum likelihood estimate of SWE and grain size, using modeled and observed T_b at 19 and 37 GHz frequencies, as well as *a priori* SWE information [160]. Atmospheric, forest cover and substratum contributions to the observed brightness temperature are also considered using empirical formulas [9, 161, 226].

In HUT model, a radiative transfer equation is defined with an assumption that scattering is propagated mostly in the forward direction. For a snowpack with a depth of d, at an incidence angle of θ, the emission right below the snow-air surface is [162]:

$$T_b\left(d^-,\theta\right) = T_{bgs} + T_{Bs} = T_b\left(0^+,\theta\right)e^{-(k_e-qk_s)\sec\theta d} + \frac{k_aT_s}{k_e-qk_s}\left(1-e^{-(k_e-qk_s)\sec\theta d}\right) \quad (3.13)$$

where T_{bgs} is the ground microwave emission affected by snowpack; T_{bs} is the snowpack self emission; $T_b\left(0^+,\theta\right)$ is soil emission just above the soil-snow interface; k_e, k_s, and k_a are extinction, scattering, and absorption coefficients, respectively; and q is the fraction of scattered intensity towards the antenna and equals 0.96 in all frequencies according to experiments by Hallikainen et al. [87] and Mätzler [133]. k_e is estimated as a function of snow grain size (D_{max}: maximum length (Diameter) of dominant particles) based on formulas presented in Hallikainen et al. [87]'s study. Using snow's dielectric properties derived by Mätzler [133], k_a is calculated. A semi-empirical soil reflectivity model presented by Wegmuller and Matzler [226] is used to derive $T_b\left(0^+,\theta\right)$. This soil reflectivity model requires the dielectric properties of soil.

HUT models atmospheric transmissivity, upwelling and downwelling atmospheric brightness temperature components, and land cover effects in mixed pixels. In so doing, it uses a simple model that assumes pixels are covered by forest and/or snow, and each land cover (snow/forest) has an emission contribution of coverage fraction multiplied by the emitted radiation. Forest canopy emission and consequently ground emissivity are empirically modeled considering the coverage fractions and forest canopy loss factor $L_{can}(1/t_{can} canopy attenuation)$. The empirical formulas derived from experiments by Kruopis et al. [108] are used in HUT for t_{can} calculation. Consequently, T_{bf} is derived by

$$T_{bf} = \left[1-\frac{1}{L_{can}^2}\Gamma_{sg}\right]T_{phys} \quad (3.14)$$

where Γ_{sg} is the snow cover reflectivity $(1 - e_{snow})$, and T_{phys} is the surface physical temperature[8]. Then, ground emissivity e_{gnd} is obtained by:

$$e_{gnd} = \left[1 - \frac{1}{L_{can}^2}\Gamma_{sg}\right] f_f + (1 - \Gamma_{sg})(1 - f_f) \tag{3.15}$$

where f_f is the forest fraction in a pixel. Consequently, the observed T_b is modeled by

$$T_b = t\left[f_f T_{bf} + (1 - f_f) T_{bs}\right] + T_{atm} \uparrow + t(1 - e_{gnd}) \cdot [T_{atm} \downarrow + t2.7K] \tag{3.16}$$

where t is the atmospheric transmissivity, $T_{atm} \uparrow$ and $[T_{atm} \downarrow$ are upwelling and downwelling atmospheric brightness temperatures, respectively. For SWE retrieval, snow grain size and SWE are optimized by minimizing a cost function of modeled and simulated T_b. A Maximum Likelihood (ML) estimate of snow grain size and SWE is obtained in an iterative process when the cost function is minimized. In an experiment conducted by Pulliainen and Hallikainen [160], the predefined information for snow and substratum properties included a density of 250 kgm^{-3}, a snow grain size of 1200 , depth of 1.2 m and effective soil roughness of 3.0 mm. Pulliainen and Hallikainen [160] stated that the root mean squared error (RMSE) of 30 mm in the SWE estimate using SSM/I and the HUT model was obtained without using any ground observations to train the model. Pulliainen [159] developed the HUT model by the assimilation of daily snow depth data obtained by weather stations as well as assimilation of interpolated SWE for all other snow pixels as *a priori* SWE into the HUT model. This methodology is employed in the GlobSnow SWE product [201].

HUT has also been adapted for a multi-layered snowpack by Lemmetyinen et al. [117]. This model assumes smooth snow layer interfaces and lambertian scattering in up and down directions (2-flux).

3.3.2 MEMLS

MEMLS is a microwave emission model in the 5-100 GHz range, based on radiative transfer for a multi-layered snowpack. It was developed by Mätzler and Wiesmann [140] and Wiesmann and Mätzler [230] based on the field experiments of Mätzler [138] (which updated his 1996 experiments). The first version of MEMLS modelled emission from different types of snow grains with a correlation length of 0.05 to 0.3 mm. This model was then

---

[8] An angular correction of $\cos\theta / \cos\theta'$ should be applied to the coefficients that are derived in the incidence angle of θ (θ' is the incidence angle in the second experiment).

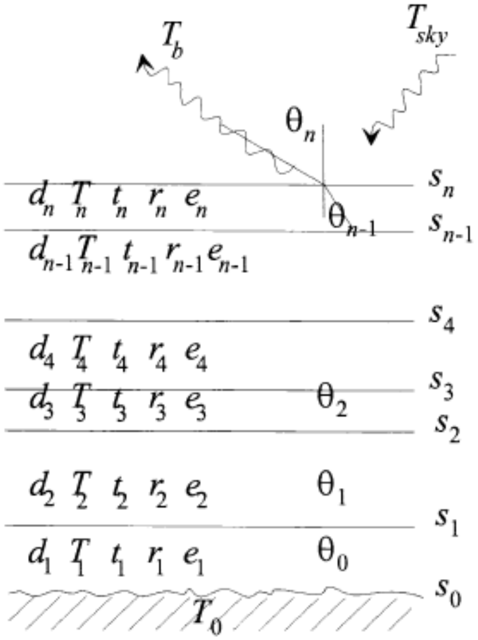

Figure 3.2: MEMLS n-layer snowpack and modeled components [230]

modified for bigger snow grains with a correlation length up to 0.6 mm. This semi-physical model simulates emission from a layered snowpack and its substratum. The substratum is presented by its temperature and reflectivity, and its roughness properties are disregarded [226]. Figure 3.2 presents MEMLS components in an n-layer snowpack. For each layer, the thickness, d, the temperature, T, the transmissivity t, the internal reflectivity, r, the emissivity, e, and the interface reflectivity, s, are entered into a 6-flux radiative transfer model [230].

A soil layer is considered as the substratum in MEMLS. Reflection coefficients are modeled as functions of soil temperature and its dielectric properties [226]. Using reflection coefficients, the upwelling emission from a soil layer after interaction with the first layer of the snowpack equals $t_1(1 - r_1)T_0$, where t_1 is the transmissivity of the first layer of the snowpack; r_1 is the interface reflectivity between the first layer of the snowpack and the soil, and T_0 is the soil temperature. The sky contribution is also treated the same way; it is added to the last layer emission after multiplication by the last layer's reflection coefficients. Therefore, the sky contribution equals $r_n(1 - S_n)T_{sky} + S_nT_{sky}$, where r_n is the internal reflectivity in the nth layer of the snowpack, S_n is the interface reflectivity of layer n^{th}, and T_{sky} is the sky temperature.

MEMLS simplifies wave fluxes in the snowpack in six directions. In this six-flux method, scattering and absorption coefficients are computed in six directions, four in the XY plane and two in Z. Reflectivity between layers and to the sensor is described by the effective propagation path from a modified equation of Snell's law[9]. This modification accounts for diffuse scattering (volume) and polarization mixing [230]. A critical angle of $arcsin(1/n')$ is defined to discriminate trapped fluxes in a layer (incidence angles larger than the critical angle) and escaped fluxes (incidence angles smaller than the critical angle).

In MEMLS, the coherent superposition of wave interactions within interfaces of snow layers is ignored if the layer is thicker than a quarter of a wavelength; otherwise, coherent interactions are considered while defining the phase function of scattering for each layer. Wiesmann and Mätzler [230] explained that ignoring coherent interactions in the transition of waves between layers is attributed to cancelling interference effects by natural variability within a layer, the local incidence angle, and different frequencies applied in a radiometer bandwidth.

The phase function for each layer is computed as a function of layer thickness, the real part of the refractive index, propagation angle, and vacuum wavelength. Reflectivity is then modeled by an equation that includes phase function ($cos(2P)$, where P is the phase function). For the phases below $3\pi/4$, a coherent layer is assumed. For a phase function higher than $3\pi/4$, the layer is treated as an incoherent layer. A coherent layer is presented by its surface reflectively as its volume scattering and absorption contribution is negligible. Also, if a thin coherent layer (thinner than half of a wavelength) is located between two incoherent layers, due to the small volume scattering and absorption in the thin layer, the thin layer's emission contribution is ignored.

In this emission model, the dielectric properties of dry snow as a function of snow density are derived by empirical formulas according to [135] and [136] for permittivity and loss factor, respectively. An absorption coefficient of $4\pi n''/\lambda$ (n'':imaginary part of refractive index, λ: vacuum wavelength) and a scattering coefficient presented by [229] as a function of frequency and the exponential correlation length of snowpack grains are used.

MEMLS code is written in Matlab and is free and available for all users . The primary input variables to simulate emission for a layered snowpack include density, temperature, LWC, correlation length, and the thickness of each layer, as well as the ground temperature (soil) and snow-ground reflectivity coefficients.

---

[9] $\sin(\theta 1)/n'_2 = \sin(\theta 2)/n'_1$, refractive index is related to dielectric properties of a slab by: $\varepsilon_r = \varepsilon'_r + j\varepsilon''_r = (n' + in'')^2$

3.3.3 DMRT-ML

Tsang et al. [214] developed an emission model, dense media radiative transfer (DMRT), for a layered snowpack based on Quasi Crystalline Approximation (QCA) and previous studies on scattering behavior of particles in a dense medium[10]. Several implementations of DMRT based on different theories for deriving the equations have been developed [205]. Here, the DMRT developed by Picard et al. [155] is explained. Picard et al. [155] employed Quasi Crystalline Approximation-Coherent Potential (QCA- CP) to model emission for a multi-layered snowpack in the range of 1-200 GHz. QCA and QCA-CP approximations allow modelling particle positions' pair distribution functions while coherent wave interactions are assumed. In so doing, these approximations allow wave interactions to be modeled in a dense media [214]. In the DMRT-ML, snow scattering and extinction coefficients and the form of the phase function are computed based on DMRT theory whereby the radiative transfer equation is solved using the Discrete Ordinate Radiative Transfer method (DISORT).

The DMRT-ML employed by Picard et al. [155] discusses two approaches based on underlying assumptions in different versions of DMRT theory. The first approach is a mono-disperse assumption in the grain size distribution within a layer. This approach employs a "short range" stickiness and Grody's empirical method for large particles. The second approach is a poly-disperse assumption in a Rayleigh distributed grain sizes. A Rayleigh phase function is implied in the second approach, and no stickiness and no large particles can be assumed due to involved complexities[155].

In the DMRT-ML, to obtain brightness (the temperature emitted from a snowpack), a modified vector radiative transfer equation for each layer is defined based on Jin [94]'s formulas. In this radiative transfer equation, the emission transfer is modelled by including Rayleigh phase function and extinction and absorption coefficients. The effective dielectric properties of a medium with mono disperse small snow grains are estimated as a function of the fractional volume of scatterers, dielectric properties of ice and air, and the snow-grain spheres' radii (and stickiness in the case of assuming clusters of grains) [191]. Extinction and absorption coefficients are estimated as a function of the effective dielectric constant. For bigger snow grains Mie scattering takes place and the extinction and absorption coefficients in this medium can be calculated either assuming a Percus-Yevick pair distribution of grains and under QCA assumptions, or by Grody [82]'s empirical approach that defines these coefficients as a function of grain size and effective dielectric constant.

The substratum's contribution as a soil or ice layer with or without roughness is added

---

[10] When the particles occupy more than 20% of the fractional volume [155]

to the multi-layered snowpack. Reflection coefficients[11] in vertical and horizontal polarizations are calculated based on the assumption of a flat or rough surface, using Fresnel coefficients. For a rough surface, a standard deviation of the surface height is considered in the reflection coefficients calculation. Depending on the soil model employed (an ice layer or a semi-infinife configuration are other possible options for the sub-stratum), different physical and geometric properties such as dielectric properties, moisture, roughness and texture are required [155]. The assumption of no interface at the sub stratum is also modeled for a semi-infinite snowpack when wave penetration is less than snow depth [155].

The DMRT-ML code is written in Fortran90 and Python, both available for all users. Recently, a new version of DMRT-ML, has been adapted for active microwave as well is distributed in a Python package by Picard et al. [156]. The DMRT-ML requirements for the emission simulation from a layered snowpack at the surface includes the snowpack physical temperature, density, grain size, stickiness, and liquid water content; the properties of the substratum; and the downwelling atmospheric brightness temperature. These inputs can be provided by snowpack physical models that predict snowpack microstructure and would result in more realistic emission modeling [180].

3.3.4 Snowpack emission modeling: comparison and discussion

Semi-empirical and physical models for snow properties retrieval help to improve our understanding of microwave, snow grains and interfaces interactions. Theoretical modeling lets us analyze the sensitivity of emissions to the microstructure parameters such as a snow grain size, depth, and density. This sensitivity analysis become possible through theoretical relations that explain electromagnetic propagation in a snowpack, for instance, modeling the effective propagation constant for a dense dielectric medium in a radiative transfer equation [155, 214, 94]. The sensitivity is also traceable using field measurements. Roy et al. [174] rank the sensitivity of parameters modeled in HUT to the observed emission signature of the snowpack, using the correlation between measured and modeled T_b at 18 GHz and 37 GHz in horizontal polarization. Snow grain size, ground temperature, snow temperature, vegetation temperature, depth and density of snow are found to have the highest to lowest effects in a HUT simulation of 37 GHz [174]. Durand et al. [49] compared the measured and simulated T_b using MEMLS at 18.7, 36.5 and 89 GHz, and ranked the sensitivity by the density of the ice layer (if an ice layer is present), uncertainties resulting from relations between grain size and correlation length, snow density, Dmax (observed

---

[11] Diffuse reflection from substratum is not included in DMRT-ML, and the reflections are based on coherent wave interactions [155].

grain size in the field), snow temperature and snow depth. In their study, soil and sky were found to have a negligible effect on the simulations. Picard et al. [155] considered the ice dielectric constant, grain size, density and stickiness as the most important inputs of DMRT-ML and explained the sensitivity of the model to these parameters, using simulated results.

The differences in the snowpack emission models can be explained by differences in their underlying assumptions and theories. Key differences between HUT, MEMLS and DMRT-ML can be explained as follows:

1. In DMRT and DMRT-ML, required parameters for radiative transfer equations, such as extinction and scattering coefficients, are estimated based on theoretical equations. In HUT and MEMLS, these parameters are defined by experimental data and empirical solutions [162, 205, 230].

2. Wave propagation within the snowpack layer is modeled as a 2-flux model upward and downward in HUT, a 6-flux in perpendicular planes in MEMLS, and many fluxes (up to 64 [155]) in DMRT-ML [16].

3. HUT uses scalar radiative transfer assuming single polarization. In contrast, MEMLS and DMRT use vector radiative transfer equation (VRT) . The scalar radiative transfer in HUT simplifies the equations; however, it is not a valid assumption for a dense medium such as a snowpack. Jin [94] explains that in a medium with dense volume scatterers, an independent scattering assumption in vector radiative transfer is not valid, and coherent scattering should be modeled. In DMRT-ML and MEMLS, phase dependent coherent scattering of particles is modeled.

4. Modelling substratum in HUT and MEMLS are the same [226]; a substratum of a rough soil whose dielectric properties are used to define the reflectivity. Using this soil model, coherent ground scatterer is not considered. In contrast, DMRT-ML considers only coherent scatter from ground, and neglects diffuse scatter [155]. Different substratum models (including ice surface) can be employed as a sub-model coupled with emission from a snowpack (e.g., in DMRT-ML by Picard et al. [155]).

5. Disparate representations of grains in snowpack emission models make it difficult to compare results from different emission models. Snowpack grains are presented by the maximum diameter of dominant particles, the correlation length and optical diameter in HUT, MEMLS and DMRT-ML, respectively.

6. In DMRT-ML, a stickiness factor explains the natural tendency among snow grains to make clusters, which are modeled while deriving an effective propagation constant [155]. The stickiness factor is not modeled in HUT or MEMLS.

Emission models are highly sensitive to grain size parameterization. This impact empowers implementation of an effective grain size for calibration of emission models. The following subsection discusses different representations of snowpack grains and how an equivalent effective grain size can represent the snowpack. Due to the significant impact of grain size, and the other parameters being estimable and conservative in nature, just grain size effect is explained in detail.

3.3.5 Grain size definition

The best representative of the snowpack grains geometric structure is considered the most challenging issue for modeling microwave properties of snow. There are different types of representatives presented in related studies, although the general idea is using spherical particles with the same scattering and absorbing behavior compared to the assumed natural snowpack. The maximum length (Diameter) of dominant particles that has been defined from a snow hydrologist perspective, introduced by Colbeck [33] and known as D_{max}. It has been argued that this assumption causes large amounts of overestimations in average grain size [137]. Roy et al. [171] explain that wide range of snow grain shapes and complex structures cause low accuracy in D_{max} measurement.

Grenfell and Warren [81] suggested representing the granular snowpack medium with spheres having equal volume to the surface area ratio ($q = V/A$). This representation is explained by assuming the equal volume spheres and equal area spheres in snowpack grains. The scattering is less in the former case, and the absorption is higher in the latter condition compared to the original medium scattering and absorption. Therefore, spherical particles with the same volume and also the same area as chosen snowpack particles would simulate same scattering and absorption properties. The radius and diameter of these spheres r_q and D_q, respectively, were obtained by Grenfell and Warren [81], thus:

$$q = \frac{V}{A} = \frac{4/3^{\pi r_q^3}}{4\pi r_q^2} = \frac{r_q}{3} = \frac{D_q}{6} \tag{3.17}$$

where V is the volume and A is the surface area of representative spheres. It should be noted that the idea of considering an equal V/A ratio radius stems from the equivalent optical grain-size D_o, assigned to particles with optical properties similar to those of natural snowpack [137, 78]. Moreover, it has been noted by Mätzler [137] that D_q is equal to D_o. Mätzler [137] described D_q as:

$$D_q = \frac{6M}{\rho A} \tag{3.18}$$

where M is the mass of representative spheres and ρ is the density of those spheres. We can also estimate D_q from equation 3.17; $D_q = 6q$. As mentioned, q equals the volume divided by the surface area. It is also related to the Specific Surface ($s = V/A$) and the volume fraction of ice ($\upsilon = \rho/\rho_{ice}$) by $q = s/\upsilon$., where s, q and υ are measured by laboratory experiments [137].

The Specific Surface Area (SSA) is another parameter defined by surface area per unit mass ($SSA = A/M = A/(_{ice}V)$), which describes the geometric and physical properties of the snowpack [115]. SSA can be measured using methods such as IR techniques, X-ray imaging or methane absorption measurements [115, 8]. Experiments conducted by Legagneux et al. [115] have shown that SSA values decrease during constructive metamorphism, and highest measured values were related to settled fresh dendritic snow. Using equation 3.18, D_q, a function of SSA, is defined by

$$D_q = \frac{6}{\rho_{ice} SSA} \tag{3.19}$$

Mätzler [137] proposed correlation length as a complementary factor for D_{max}. This parameter is defined as a characteristic grain size, based on the Grenfell and Warren [81] definition (spheres that have an equal volume to surface area ratio). Mätzler [137] explained methods for estimating the correlation length using theoretical procedures such as the spatial auto correlation slope (p_c is calculated), and the exponential correlation function (p_{ex} is calculated[12][229]), and intercept length experiments (p_c is computed). In the latter, the correlation length is measured by stereology of the snow medium referred to as spatial interpretation of snow planar sections, and is computed from the intercept length of air and ice. Noteworthy that all the aforementioned methods are similar in their computation of correlation length components in granular materials that contain two components [137].

The relationships obtained between p_{ex}, p_c, D and D_o are summarized based on both

---

[12] $p_{ex} = 0.75p_c$

theory and experiment:

$$\begin{aligned}
&p_{ex} = 0.16D_o \\
&p_{ex} = 0.25D_o \\
&p_{ex} = 0.75p_c \\
&p_{ex} = 0.5D \\
&(D < D_o)
\end{aligned} \tag{3.20}$$

To date, only a few studies have compared known snowpack emission models, to explain the adaptability of inputs and analyze the differences. Significant examples were studies by Foster et al. [71], Royer et al. [176], Pan et al. [150] , and Sandells et al. [180]. On the other hand, grain size parameters, the key component of emission models are discussed in multiple studies, most agreeing on prioritizing the measurement of the SSA in the field to represent sphere grains, using the optical equivalent diameter [75, 115, 139, 149]. In addition, a micro-computed tomography technique for measuring the correlation length of snow grains, which is a parameter used in MEMLS, has been presented by Proksch et al. [158], and Krol and Löwe [107]. However, it has been augured that SSA and correlation length alone cannot characterize snowpack medium properly, and a better representation of the natural microstructure of snowpack is achieved by assuming clusters of grains randomly positioned in large vacant spaces, which can be represented by assuming and applying a stickiness factor. Tsang et al. [215] introduced a stickiness factor for enhancing the scattering properties of grains by calculating scattering and extinction coefficients. Löwe and Picard [128] stressed that applying a stickiness factor is essential, as it can represent the relative positioning of spherical particles with a fixed diameter; however, it is an unmeasurable factor. Detailed discussion on this subject as well as descriptions of an effective grain size can be found in chapter 4.

Next, is a brief description of technical aspects of spaceborne PM radiometers and three well-known examples of PM sensors.

3.4 Spaceborne radiometry

Spaceborne radiometry originated from radio astronomy ground-based techniques, which then underwent dramatic changes in being adapted for surface-observations requirements [190]. In spaceborne and ground-based PM radiometers, incident radiance is observed by an antenna and converted to a voltage, which is then amplified and registered as the brightness temperature observation. Due to the low energy of microwave channels operating in radiometers (5 GHz-100 GHz), spaceborne sensors should be designed either to observe for longer or gather enough energy detectable by larger footprints. As the former solution is not applicable, the latter is applied in radiometers' design [218]. It should be noted that spatial resolution is relevant to the diffraction limit, and its angular Full Width to Half Height(FWHH) is in the order of l/D (wavelength / diameter of dish) [166]. In other words, a higher wavelength causes lower spatial resolution, and the bigger the dish antenna, the better the spatial resolution. In order to minimize surface reflection, the sensor incident angle is designed to be close to Brewster's angle (however, this angle differs for different mediums and polarizations).

Current passive microwave sensor platforms are located in near-polar sun-synchronous orbits[13], with approximate altitudes of 800 km. The advantage of these orbits for earth observation is that they cover most areas of the planet twice daily. In addition, most coverage is gained in near polar areas. Most passive sensors have a conical observing geometry with a fix incidence angle scanning in a forward direction. These systems have less swath width compared to cross track scanning observation geometry. However, one of the weaknesses in the cross-track scanning systems is the footprint size variation from nadir to the extent of swath (highest to lowest resolution, respectively), resulting different viewing angles in the observation geometry [54].

3.4.1 Special Sensor Microwave Imager (SSM/I) and the Special Sensor Microwave Imager Sounder (SSMIS)

Defense Meteorological Satellite Program (DMSP) satellites carried multiple radiometers of SSM/I and successive SSMIS since 1987 with three active radiometers of F16 SSMIS, F17 SSMIS, and F18 SSMIS. These near polar orbiting satellites are sun-synchronous with an inclination of 98.8° at an average altitude of 833 km with a swath width of 1400 km and an orbit period of 102 min [89]. SSM/I and SSMIS have seven-port horn antenna at 19.35, 23.2, 37, and 85.5 GHz, where all frequency channels are dual-polarization except 23.2 GHz that is measured at Vertical polarization only.

NASA's MEaSUREs Program produces SSM/I and SSMIS data products to support monitoring cryospheric and hydrologic time series, in two processing levels of "rt" and "v7" as well as daily, 3-day, weekly, and monthly average. Further processes lead to high level products such as surface wind speed, atmospheric water vapor, cloud liquid water, and rain rate.

---

[13] Platforms in sun-synchronous orbits meet an observing point in the same local time, which is during night and day time with twelve hours difference.

3.4.2 Advanced Microwave Scanning Radiometer for the Earth Observing System (AMSR-E)

The Aqua satellite containing the AMSR-E launched May 2002. The system operated until October 2012. Aging lubricants led to its discontinuation; however, that lifetime was longer than planned. AMSR-E was a modified version of AMSR carried by the Advanced Earth Observing Satellite-II (ADEOS-II) launched December 2002 and was a joint project of the National Space Development Agency of Japan (NASDA) and the National Aeronautics and Space Administration (NASA) for the EOS Aqua satellite mission [97]. As a six-frequency dual polarized radiometer, AMSR-E's main mission was to estimate geophysical parameters in water cycle such as of water vapor, precipitation, sea surface temperature (SST), and soil moisture [97]. Two key elements of AMSR-E were the 1.6 m main reflector diameter (AMSR and AMSR2,the successor to AMSR-E, have the largest dish antennas among current instruments, both at 2m diameter) and the added 6.925 GHz channel, which can be used for SST and soil moisture retrieval [148, 228].

Aqua operates in a sun-synchronous, near-polar, low-earth orbit (705 km) that observes the earth at approximate local times of 1:30 am and 1:30 pm, with a 55° incidence angle. The coverage swath width of AMSR-E was 1450 km. The sensor spin rate is 40 r/min, so each scan took 1.5 s. Measurements at different frequencies were made by feed horn antennas, and for the data calibration in each scan, high temperature noise source (HTS)—blackbody reference load—and Cold Sky Mirror (CSM) data were used in two point linear extrapolation to obtain the effective observed temperature [97].

3.4.3 Advanced Microwave Scanning Radiometer 2 (AMSR2)

The AMSR2 onboard Global Change Observation Mission 1st-Water Satellite (GCOM-W1) launched in 2012 and was placed in low earth orbit A-train satellite constellation orbit (the same as the AMSR-E orbit onboard Aqua). GCOMW-1 is in collaboration with Suomi NPP to provide Environmental Data Records (EDRs). As a result of being a successor, AMSR2 inherited most of AMSR-E's sensor characteristics; however, some improvements in AMSR2 sensor and viewing geometry have been made. The modifications include added 7.3 GHz channels for radio frequency interference (RFI) detection, better spatial resolution and extended effective swath width (1450 Km to 1600 Km) due to increased antenna size (1.6m to 2m), a redundant momentum wheel and an improved calibration system [91]. In AMSR-E sensor, fluctuation of temperature in the HTS microwave absorber caused difficulties in calibration. Improvement for less variation in the AMSR2 HST unit is performed by a different thermal design and modified sun intrusion shielding [92].

3.5 Summary

This chapter has reviewed equations explaining the brightness temperature, emissivity and relation between an observed T_b and the emission properties of a medium, and radiative transfer. In terms of spaceborne PM remote sensing, the relation between observed T_b and terrain self-emission was explained, following a review on the observing geometry and main characteristics of AMSR-E (as we have used AMSR-E observations in chapter 5).

Semi-empirical and physical models for snow properties retrieval help to improve our understanding of microwave, snow grains and interfaces interactions. Theoretical modeling lets us analyze the sensitivity of emissions to microstructure parameters such as a snow grain size, depth, and density. Emission modeling of a snowpack using HUT, MEMLS and DMRT-ML has been explained, following a review of specific differences between these emission models caused by employed different theories and assumptions. Lastly, different representations of snow grains were discussed.

The next chapter reviews snow depth and SWE retrieval methods using passive microwave remote sensing observations. While the spatial resolution problem is largely in the realm of engineering design and constrained by physical restrictions, a better understanding of the whole range of retrieval methodologies can provide the clarity needed to move the thinking forward in this important field. Moving forward to a real case study, Chapter 5 elaborates on parameterization of the DMRT-ML with the *in situ* snow measurements of tundra snow in the Eureka region using a two-layer snowpack in two configurations: a depth hoar and a wind slab dominated pack. Conclusively, emission modeling predictions were compared to airborne observations. Using these parameterizations, Chapter 6 explains employing the Bayesian Algorithm for Snow Water Equivalent Estimation (BASE) to retrieve snow depth for the same case study.

Chapter 4

Review of SWE retrieval methods using spaceborne passive microwave radiometry

4.1 Introduction

Over the history of passive microwave (PM) remote sensing (RS) of the Earth from space, numerous studies have focused on Earth's surface monitoring using observations from the microwave part of the spectrum at 6-90 GHz. PM observations of surface and subsurface targets provide all-weather and day and night observations that remote sensing using other parts of the spectrum does not provide. Atmospheric windows in the PM spectrum are sufficiently wide that all but the thickest of clouds do not interfere with observations of surface and subsurface emissions. This robust remote sensing technique is particularly useful for monitoring snow water equivalent (SWE) and snow depth (SD) which influence climate at local and global scales [41] and represent a valuable water resource in many regions of the world. There are many studies that reinforce the importance of PM in snow properties retrievals and its significant contribution in accurate retrievals specifically in cases where *in situ* measurements have limited spatial and temporal coverage or these datasets are not available at all. Two significant instances are studies by Goodison and Walker [79] and Vuyovich and Jacobs [223].

Fundamental studies of microwave properties and emission modeling of snowpacks (e.g., [140, 214, 215, 180]) and significant works on hydrology of snowpacks (e.g., [192, 41, 193, 132]) have been published that support substantial efforts in the field of snow detection and SD retrieval using remote sensing techniques (e.g.,[83, 201, 204]). Rees [166] gives a good overview of cryospheric monitoring by means of remote sensing observations and explained available methods while presenting related applications for each component of the cryosphere. In a more-recent review, Tedesco [203] comprehensively discussed different remote sensing and field measurement tools and techniques for observing the cryosphere in bringing examples of employed methodologies. Significant review papers on remote sensing for SD estimation have been published in the last ten years. Frei et al. [74] examined global products of snow extent and SWE created using optical and passive microwave data, using both satellite and additional data sources. Dietz et al. [43]'s review paper elucidated the physical processes of a snowpack that controlled the observed response from snow in the visible, infra-red and microwave part of the spectrum, followed by SCE and SD retrieval methodologies, and an overview of available products. In the forward emission modelling field, a few inter-comparison studies exist, such as those by Tedesco and Kim [205], Royer et al. [176], and Sandells et al. [180].

Despite the extensive efforts of researchers to provide accurate SWE retrieval using PM, current SWE products still do not meet the minimum operational accuracy requirement for hydrological applications (±15%) [14]. One reason is the inherited low spatial resolution of PM observations. Another reason is knowledge gaps in coupling precise physical emission models of snowpack to airborne/spaceborne remote sensing observations. Emission models of snowpacks have been employed in various ground-based experiments; however, only a limited number of studies focus on retrievals using remote sensing observations through physical emission models. The scaling process is another challenge that impacts the accuracy of retrievals; generalizing *in situ* measurements for snowpack emission modeling and for the evaluation of retrievals is a very important analysis has largely been ignored. Another source of uncertainty is associated with snow properties retrieval of footprints with subpixel coverage of other landcovers such as bare soil, vegetation and waterbodies. Findings have shown that PM SWE retrievals tends to underestimate SWE in forested areas, areas in close proximity to open bodies of water or when temperatures are above -2 °C [71, 45, 36]. SWE retrieval in complex relief terrain is another challenging process that has been investigated in a few studies (e.g., [121, 211]). Although extensive research has been carried out on aforementioned areas, to our knowledge, no single study exists which provides a methodology for global snow properties retrieval in stated cases. In contrast, vegetation as one of the prevailing landscapes in snow-affected regions impact on snow retrieval in mixed pixels can be calibrated [162, 170], however the focus of this paper is critically evaluating snow properties retrieval approaches and therefore studies on suppixel mapping are not addressed here.

Given the lack of uptake of passive microwave remote sensing estimates of SWE in hydrometeorology and hydroclimatology applications, and the probable causes being coarse spatial resolution and retrieval methodology uncertainty, there is a need to assess the future potential of passive microwave remote sensing of snow. While instrument spatial resolution is bound to the physical restrictions on engineering, improvements in retrieval approaches can be addressed and it is with this scope that this paper focuses its attention. A retrieval methodology in remote sensing problems provides a framework for estimating variables that cannot be directly observed [183]. PM SWE retrievals are traditionally performed by empirical modeling using regressions and are calibrated by *in situ* measurements (e.g., [36, 70, 98, 204]. Substantial progress made in the emission modeling of multi-layered snowpacks, based on semi-empirical and physical emission models conducted by ground-based and/or laboratory experiments, created the foundations of SWE retrievals by PM remote sensing through emission modeling. Using simulated brightness temperatures (T_bs) from the radiative transfer (RT) solution of a snowpack, and PM remote sensing observations in an inverse modeling scenario, snowpack properties can be retrieved. *In situ* measurements can be employed to increase the accuracy of snowpack property estimation by: 1) characterizing and confining the snowpack variables via physical snowpack models (e.g., [114]); 2) calibrating empirical modeling and/or providing input variables for emission modeling if they cannot be measured or where measuring is not feasible, such as grain sizes (e.g., [201, 204]); and 3) being integrated into the inversion process by radiance assimilation techniques [122].

This review, unlike previous review papers, focuses on the methodologies for snow property *retrievals* using radiometric observations of snowpacks at 10-37 GHz. First, it briefly reviews retrievable key parameters that have significant impacts on hydrological and climate models, then explores how these key parameters change throughout the snow season. Various methods of retrievals along with notable products are presented afterwards. Stand-alone snow products that are retrieved globally using passive microwave observations are the main focus, but other products that include additional data sources are also briefly touched on. Finally, the issue of accuracy assessment is discussed since it determines the uptake potential of the SWE estimates.

4.2 Snowpack properties and the characterization of a snowpack for emission modelling

4.2.1 Emission properties of a snowpack

Microwave emission through a granular medium such as snow is subjected to absorption, scattering by snow grains (ice crystals) or transmission through the pack, depending on snowpack state and wavelength. For dry snow, scattering dominates the signal when the wavelength of the electromagnetic radiation is smaller than or comparable in size to the snow grains (wavelength of 0.8 cm-1.6 cm equivalent to 37-19 GHz). At longer wavelengths (3 cm and above, equivalent to 10 GHz or less) complete transmission leads to a zero sensitivity of the emission to the snow, regardless of snow depth [230]. Therefore, wave penetration through a dry snowpack increases with a wavelength increase. However, once snow starts to melt, or contains liquid water, the wave penetration decreases and the pack absorbs radiation. Penetration depth, which ranges from 1-10 m in a dry snowpack, is less than 10 cm in a wet snowpack for frequencies within the 10-37 GHz range, the most sensitive range for surface properties retrieval using PM. The spatially variable occurrence of wetness events on T_bs at different frequencies therefore adds ambiguity to SWE retrievals and so this paper takes only dry snow retrieval processes into consideration, ignoring studies that focus on wet snow retrievals (e.g., [209, 224]).

To model the surface emission form a snowpack as observed by a PM radiometer, a lossless sensor, an emitting surface, and the atmosphere between them are assumed. The three microwave sources observed by the radiometer are: atmospheric self-emission (T_{UP}), terrain self-emission (T_{surf}), and scattered downward atmospheric contribution (T_{SC}). The terrain self-emission and downwelling atmospheric contribution are attenuated by atmospheric loss, explained either by a loss factor (L_a) or atmospheric transmissivity ($e^{(-\tau)}$). Other contributors such as cosmic emission and emission from the background (to the target and then incident to the sensor) can be disregarded according to the relatively small magnitude of these components [186]. Thus, the apparent temperature (T_{AP}) observed at the spaceborne PM radiometer is modeled as

$$T_{AP} = \left(R \times T_{SC} + (1 - R)T_{surf}\right) e^{-\tau} + T_{up} \tag{4.1}$$

where R is the surface reflectivity, assuming that there is no transmissivity into the surface. For completeness, the emissivity (ε) equals $1 - R$. The atmospheric transmission at the commonly used frequency channels of interest (10, 19 and 37 GHz) is greater than 95% [218] and so if the simulation seeks to estimate observed emission at the spacecraft, the atmospheric contribution needs to be included. If the emission is to be predicted close to the snowpack, this term can likely be deemed negligible.

Close to the snowpack, the landcover emissivity given a downwelling sky radiation measured by ground based measurements is [139]:

$$e = \frac{T_{\text{surf}} - T_{sc}}{T_{phys} - T_{sc}} \tag{4.2}$$

where T_{phys} is the surface physical temperature. The dielectric properties of a medium as well as its composition define its emissivity and so the microwave interactions in a medium (including snow) are controlled by its geometrical structure and electromagnetic properties. Therefore, before discussing the forward emission modeling of snowpack, it is necessary to review snowpack hydrological properties and its evolution throughout the season with respect to its geometrical structure.

4.2.2 Hydrological properties of snowpack and its seasonal evolution

A comprehensive explanation of the seasonal metamorphism of snow was published by Colbeck [31]. The main physical hydrological properties used to characterize snow include SD, bulk density and SWE. SWE is the height (cm) of liquid water contained in a vertical column of snow with a cross section area of 1 cm^2. Information about density complemented by grain size control the snowpacks scattering response to electromagnetic field emission and radiation. These two variables also characterize a snowpack's stratigraphy which evolves during the winter season in response to variations in mass and energy fluxes that act on the snowpack [7]. Therefore, seasonal snowpack evolution should also be considered in a robust retrieval approaches, with metamorphic processes accounted for in regional-scale applications [112].

Snowpack stratigraphic evolution and transition to melt form are mostly controlled by the thermal gradient induced by the low thermal conductivity of the snow [132]. The positive values of net radiation and heat flux coming from the substratum (toward the snowpack surface) are the most important contributors to the temperature gradient between snow and the underlying ground. During seasonal snow evolution, constructive and destructive metamorphic processes modify grain size and density in a snowpack. The characterization of snow grain size, density and temperature for emission models requires grain-growth, densification and thermal models that should be calibrated using observations and *in situ* measurements [180]. It should be noted that there has been a significant debate regarding the determination of how snow grains are represented in emission models. While it is beyond the scope of this paper, it should be recognized that the term "grain size" is imprecise, therefore hereafter we use the general term of "snow grain metrics" to avoid this misrepresentation.

Snowpack evolution has been formulated either by empirical relations based on climatology or by physical or semi-physical models. Sturm and Benson [196] proposed a grain trajectory model that uses photogrammetric measurements of grains. In their research, an exponential decrease in the number of grains per unit mass through a season was fitted to grain measurements by sieving different layers of a snowpack. Kelly et al. [99] used this grain growth to provide grain metrics input values in a physical emission model coupled with passive microwave observations. In this growth model, a temperature gradient large enough for kinetic growth (0.1-0.2 °/cm) is assumed. At lower temperature gradients, Kelly et al. [99] proposed 0.008 mm/d based on Colbeck [31]'s study.

Regarding snow climate classes densities and densification throughout the season, Sturm et al. [200] developed a statistics-based approach for the density estimation of a seasonal snowpack using snow depth data. In this method, the snow climate classes from Sturm et al. [199] are used to derive separate coefficients for each class. Additionally, they employed a deviance information criterion (DIC) method to find the best predictor variables (such as snow depth, day of year and snow class) that impact the bulk density by means of the highest coefficient of determination, R^2, and least DIC scores (model fit factor). In a similar approach, Tedesco and Jeyaratnam [204] derived a densification formula using Bayesian statistics for SWE estimations of PM observations based on *in situ* snow depth, density, and SWE for each snow climate class.

With the major advances in scientific understanding of snow metamorphism, snowpack evolution can be relatively accurately predicted using physical land surface models that leverage meteorological mass and energy measurements as inputs for an accurate emission modeling Mätzler [139]. SNOWPACK by Lehning et al. [116] and Crocus by Vionnet et al. [222] are two well-known one-dimensional energy and mass evolution models for snowpack state prediction.

4.2.3 Forward emission modeling of a snowpack

In a simplified emission model where snow is considered as a single homogenous medium, the snowpack's dielectric constant is estimated by a weighted average of the dielectric properties of air, ice particles, and water. In a heterogeneous layer, internal scattering is also considered. In the case of dry snow (liquid water content is zero), a mix of air and ice-particles is assumed, and results in a simpler solution than if water is present. To simulate the emission of a snowpack, a robust solution to the RT equation is needed that accounts for emission from the substratum through the pack to the air-snow interface. Different RT model representations are available and are based on different assumptions and theories for computation of the equation unknowns such as the extinction, the scattering, phase functions, and transmission in each layer of the snowpack.

The emission model of Helsinki University of Technology (HUT) [162], the microwave emission model of layered snowpacks (MEMLS) [140, 230, 229], and the dense media radiative transfer theory for a multi-layered snowpack (DMRT) [214, 155, 27], are three distinct emission models for a multi-layered snowpack. The HUT model is an empirical representation of physics-based model while the MEMLS and DMRT models are more physically based. Emission models' accuracies and sensitives have been extensively evaluated using ground-based experiment PM observations [230, 49, 117, 171, 176]. However, fewer studies have evaluated the use of physically-based emission models at airborne/spaceborne scales [66, 169, 16, 143, 112, 177, 178]. Interestingly, while HUT is considered an empirical model, it is an exception compared with the other two modes since it is in operational use with the GlobSnow product [201] providing near global land surface estimates of SWE. The HUT model achieves this by empirically representing the extinction and scattering coefficients and by simplifying the wave propagation as a 2-flux, which is rather less complex than the MEMLS and DMRT approaches. Moreover, the RT solution is considered a scalar thereby assuming a single polarization.

Intercomparison studies of snowpack emission models are relatively few but those that have been conducted have provided insights into the performance of different snowpack microwave representations and how they differ in requirements and functioning. Tedesco and Kim [205] highlighted the discrepancies found from using different emission models, whereas none of applied emission models could reproduce the observed emission within a reasonable accuracy and therefore authors recommended more experimental analysis to improve the performance of available emission models. A decade later, Royer et al. [176] and Sandells et al. [180] presented the use of different emission models and inferred a need for a better microstructure representation of snowpack in emission models as well as a need for the interchangeability of snowpack microstructure metrics into different emission models to avoid errors incorporated to different grain metrics in comparison studies.

A key recent advancement from modeling experiments is how snow grain metrics is treated by the models. Grain metrics are key input variables for the emission models and only recently has there been convergence in how grain metrics should be quantitatively prescribed for use in the models. Most models agree on prioritizing the measurement of

Specific surface area (SSA) or correlation length in the field to represent spherical snow grains using the optical equivalent diameter [115, 139, 149, 75]. SSA and correlation length measurements, however, are challenging without sophisticated equipment. SSA measurements can be achieved using an integrating sphere approach [75] while a micro-computed tomography technique for measuring the correlation length of snow grains, which is a parameter used in MEMLS, has been presented by Proksch et al. [158] and Krol and Löwe [107]. While SSA and correlation length characterize a snowpack's discrete grain geometry, they are unable to represent grain assemblages (aggregates of snow grains) well. A different representation of the natural microstructure of snowpack assemblages has been demonstrated by assuming clusters of grains randomly positioned in large vacant spaces, which can be represented by assuming and applying a stickiness factor. A so-called "stickiness factor" was introduced by Tsang et al. [215] to represent the enhanced scattering properties of grains that are aggregated to varying degrees thereby affecting the scattering and extinction coefficients. Löwe and Picard [128] stress that applying a stickiness factor is essential since represents the relative positioning of spherical particles with fixed diameter, it is an unmeasurable parameter. Therefore, another way of representing a snowpack microstructure for microwave modelling is to assume a size distribution of grains within a discrete snow layer. This makes the application of a stickiness factor unnecessary [155]. Furthermore, building on this concept, Roy et al. [171] proposed applying a scaling factor on SSA grain sizes by minimizing the RMSEs of simulated and observed T_bs. They explained that this scaling is required in emission modeling because a grain metrics distribution and stickiness between grains cannot fully represent the emission signature.

4.3 Snow detection and SD or SWE retrieval techniques

Current retrieval methods are discussed by elaborating on how emission modeling knowledge is integrated in numerical inversions. First, snow detection is explained as a preprocess that is applied in global retrieval methods to minimize retrieval uncertainties.

4.3.1 Snow detection

To decrease the uncertainties involved in snow cover detection using passive microwave remote sensing observations at global scales, land ice, water bodies, and grid cells where snow presence is climatologically impossible are masked out using Dewey and Heim [42] snow climatology dataset [98, 204]. For places where snow accumulation is possible, snow cover can be detected if $_b$ values (T_b19- T_b37) are greater than a pre-determined threshold [186]. Kelly [98] defines this differential value as 0 K but notes that it is applicable for shallow to moderate snow depths. For deeper snow, scattering at 19 GHz can occur causing a depression in the T_b 19 GHz channel and a lower "background frequency" T_b is preferable such as at 10 GHz. If snow cover is deemed to be present then snow depth retrievals can be applied.

4.3.2 Retrievals using traditional regression-based methods

The discussion in the section 2 indicates that the microwave emission from snow is controlled by both the quantity of snow (SWE) and the quality of snow accumulation (snow microstructure). Retrieval approaches, therefore, should be sensitive to both elements in order to minimize estimation uncertainties. A simple linear empirical approach typically creates a functional relationship between observed T_bs and the snowpack physical property of interest (i.e. SWE). Early studies based this relationship on observational data [109] or from theoretical model data developed by Chang et al. [26]. In either case, a derived regression model connects the observed T_bs with the combined emission from snow and substrate reflected as the snowpack SWE. The relation is usually based on the difference or ratio between a short wavelength observation at 37 GHz, and a longer wavelength one at 10 or 19 GHz. Typically, at 37 GHz, the T_b observation decreases with increasing dry snow accumulation (depth) whilst the T_bs at 10 or 19 GHz are unaffected by the snow and respond more to the substratum emission. Using a $_b$, such as T_b 19 GHz - T_b37 GHz, mitigates the effect of the snowpack physical temperature and variations in soil dielectric permittivity that impact the emitted radiation from the SWE. In doing so, the $_b$ value is related to the bulk snow mass via the degree of scattering in the snowpack; the thicker the dry snow, the more the microwave scattering occurs (expressed as a depression in the T_b at 37 GHz) and the greater the $_b$ response since the T_b at 19 GHz is generally unaffected. Recent studies, however, have demonstrated that while these empirical approaches are attractive on account of their simplicity, they do not adequately mitigate the effects of physical temperature, snowpack microstructural controls, especially grain metrics, or soil dielectric permittivity [100, 65, 237]. Despite effectiveness and applicability of applied methods in global retrievals [100, 201, 204], more sophisticated representation of the microwave interactions with the snow are necessary to achieve robust estimates of snow accumulation and account for these confounding variables.

Figure 4.1 illustrates the decrease and reflection in the T_b signature at 36 GHz (vertical and horizontal polarization) and $_b$ as a function of measured SWE from an investigation conducted by Matzler et al. [141]. Considering a dry snowpack with less than a meter depth, when SWE increases, T_b37 decreases exponentially [217]. After a point of 150 mm or 200 mm of SWE (the thresholds suggested by Takala et al. [201] and Schanda et al. [184], respectively), T_b increases, and an ambiguity in T_b and SWE relationship-interpretation emerges. In our recent study, it has been shown that this threshold is as low as 21 cm depth in tundra snowpacks, where dense wind slab is developed on top of a thin depth hoar layer in late winter [178]. A simple physical explanation is that in a deep snowpack (deeper than a meter), 37 GHz frequency is not a volume scattering frequency; therefore, it does not decrease as SWE increases. Furthermore, 19 GHz microwave, which has been considered a sensitive frequency to the substratum, will play a volume scatterer role in this medium. The penetration depth limit of a microwave at 37 GHz in a dry snowpack and the ambiguity in the T_b and SWE relationship limit the application of an empirical equation for a snowpack with more than a meter depth. An empirical solution for SWE retrieval in snowpacks with higher than 120 mm SWE would be using T_b differences at longer wavelengths (T_b19V - T_b10V) [35, 98, 206].

4.3.3 Retrievals by the inversion of physically based models

Empirical retrievals aim to estimate variables of interest without providing understandings of the physical processes involved, whereas snow properties retrieval relies on our available knowledge of source of emission and the RT within the dense medium and how it quantitatively interprets snowpack properties. Therefore, better understanding of physical processes that control the emission facilitate making assumptions and simplifications in emission models, as well as constraining and parametrizing the model inputs for operational applications [221].

Due to the complex nature of emissions in a snowpack, no analytical solution has yet be found to invert physical emission models and derive the variables of interest, such as $SD = f^{-1}(T_b)$. The reason is the nature of this inversion problem, whereas many unknown parameters (compared to a few observations) are controlling the emissions signature and therefore we encounter a rank-deficient problem. To have an overdetermined system of equations or in other words to make the system of equations reliably invertible, we can either obtain multiple set of observations over a snowpack or constrain model parameters [202]. In PM remote sensing of snowpacks, assuming the steady state of snowpacks considering available temporal resolutions of observations is not applicable and therefore, we cannot increase the number of T_b observations in the system of equations. Instead, to make inversions reliable we have to either constrain the physical model parameters by parameterizations or simplify the physical process which both decrease the free parameters

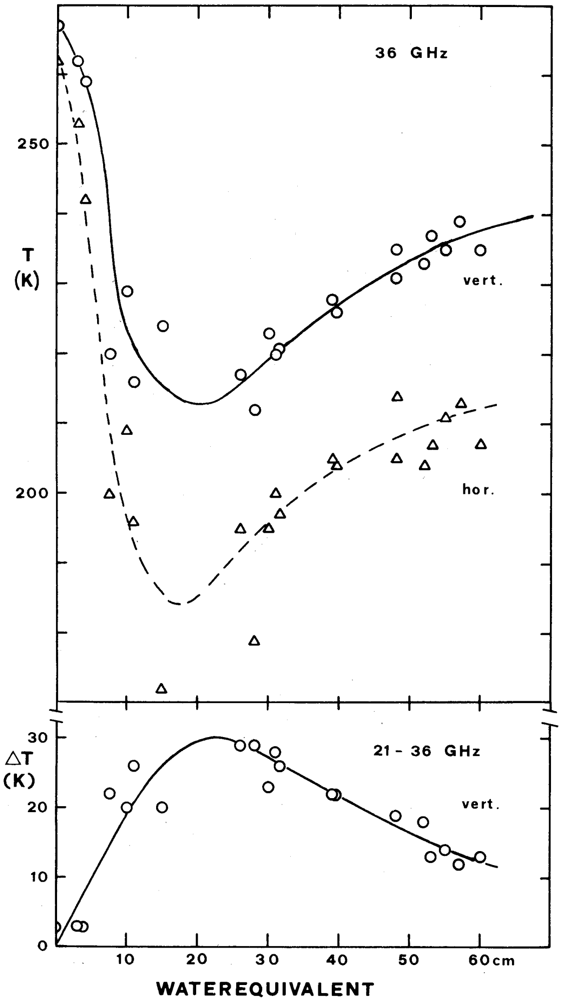

Figure 4.1: T_b measured at 50° incidence angle, at 36 GHz in both horizontal and vertical polarization (upper) and $T_b21 - T_b36$ in vertical polarization as a function of SWE (lower) during beginning of snow season to late winter in March 1977-December 1980 [141].

of physical-based models. Having an overdetermined system of equations, one numerical solution is the estimation of cost functions. Using cost functions, we seek for an optimum solution rather than a unique solution. We can either search for a global minimum of the cost function or evaluate the posterior probability of the state variables. The former refers to a deterministic answer to an iterative search (e.g. [100, 204], whereas the latter refers to a probabilistic response of the inversion system (e.g. [46, 151].

Machine learning (ML) techniques can be used to retrieve snowpack properties by performing an explicit inversion and finding non-linear relationships between observations and measurements iteratively or non-iteratively (e.g., [21, 208, 211, 65, 204, 194, 236]. Although non-linear relationships can be made using ML, the concept of inversion is similar to application of a cost function minimization. On the other hand, the tractability of ML methods such as Neural Networks and Support Vector Machines as the most popular ones in this field is still questionable. Inversion methods should be reproduceable, simple, and yet within an effective framework that include uncertainty analysis. A good example for a simple yet effective inversion is the use of a Bayesian retrieval probabilistically that allows the integration of *a priori* knowledge of snowpacks into a retrieval framework while making uncertainty analysis of retrievals feasible (e.g. [46, 151]). Unlike ML algorithms, understanding and building on employed Bayesian-based inversions is tractable, however until recently, there has been little interest in this field.

Employing data assimilation in SD retrieval

Having discussed uncertainties caused by the availability of a few independent PM observations through inversion algorithms, in this section, data assimilation as a technique that addresses this problem by integrating different data sources for accurate SD retrievals is explained. Data assimilation that was first used in atmospheric modeling—specifically weather prediction—has been employed to improve the estimation accuracy using other information sources as well as models and then gradually attracted interest for other applications. To estimate state variables the term used in data assimilation context in lieu of snowpack properties of a snowpack from PM observations, an RT model should be used either as an observation operator (in forward modeling of variables) or in a retrieval algorithm (as an inverse observation operator). If radiance assimilation is used, there is the advantage of having consistency among datasets from RT and geophysical models, as they are both used in the same data assimilation system [167]. However, assimilated retrievals are based on external estimates of desired variables that are inconsistent with geophysical models within an assimilation system. Relevant studies based on assimilated retrivals suggest using Land Surface Models (LSM) to provide information on snowpack, as they found that with minimal information on snow grain metrics and layering, retrievals from deep snow will be errorneous [49, 50, 213, 46].

In a radiance assimilation scheme, a snow model such as LSM, SNOWPACK [116] or CROCUS [18, 19] is used to predict the state variable of a snowpack, including its multi-layer thickness, density, temperature, and liquid water content, plus the ground temperature. Grain metrics can be estimated using grain growth parameterizations and then integrated it into the snowpack model. Grain growth formulas such as one suggested by Flanner and Zender [63] as a function of snow temperature and temperature gradient and density employed by Durand et al. [50] and Durand and Margulis [48], or the grain growth model of Jordan [95] employed by Durand and Margulis [47]. Grain growth models are disregarded in a few data assimilation frameworks such as works by Toure et al. [213] and Durand and Liu [46]. In the former research, grain metrics parameters and growth were randomly selected, whereas in the latter, a snowpack's probability distributtion function (PDF), including its grain metrics PDF is utilized to explore the feasibility of using minimal prior information in a Bayesian inversion framework.

One limitation of a radiance and more generally data assimilation is that snow state variables used in an assimilation are needed to be accurate enough to improve the analysis. For instance, in order to improve the analysis by assimilation, Durand et al. [49] specified a criterion for the snow model of ±0.045 mm for simulated optical grain size accuracy and $\pm kgm^{-3}$ for the density of melt-refreeze layers. Another challenge in data assimilation methods is the inclusion of detailed snowpack properties such as stratigraphy, grain metrics, and density in each layer, and the variance associated with these variables in the state variables. In a case in which cost function does not include the aforementioned variables, then an updating step would result in error accumulation. For example, the impact of modeling stratigraphy has been explored in a few studies, such those of Durand and Liu [46] and Richardson et al. [168] , who stressed that ignoring layering details causes a bias in T_b simulation due to not considering the emission reflection at boundaries and subsequently disregarding the impacts of diverse snow grain metrics and densities.

4.4 Global operational SD and SWE products

To date, various SWE and SD products have been created, employing different datasets and methodologies at different scales and extents, at diverse spatial and temporal resolutions. Among all available SD/SWE maps from PM remote sensing observations, we reviewed specific characteristics of three global operational SD/SWE products in Table 4.1. These products are created using spaceborne PM observations, where auxiliary data sources are minimal and the main purpose of limiting integration of other data sources is minimizing the error propagation in the SD estimations as well as considering that *in situ* observations are not globally available. In terms of data processing steps, global SD and SWE estimations generally include two major steps of snow detection and SD retrieval. Forest cover correction, masking water bodies, urban areas and complex terrains are other common processes [98, 204]. Another important step is a post-process for testing the accuracy with quality controlled *in situ* measurements, which provide an error analysis of final SD/SWE products.

In addition to the listed global SD and SWE products of PM observations in Table 4.1, there are other significant non-global significant SD products such as passive microwave SWE data for the Canadian Prairies by Canadian Cryospheric Information Network (CCIN)[2] and the SD product of Pulliainen and Hallikainen [160]. The latter was a baseline for Globsnow version2; employing SSM/I[1] T_bs, SD is derived from kriged synoptic weather station and grain sizes are estimated by minimizing observed and simulated T_bs from HUT model. SDs are then estimated using T_b observation and HUT simulations. A recent algorithm for SD and SWE retrieval using AMSR-E (NASA) observations is developed by [204] who employed a non-linear relationship between SD and T_bs using coefficients from trained Neural-Networks of simulated emissions using HUT and T_b observations. Sturm's snowpack densities are then used for SWE estimations. SD products of this algorithm are not available online yet. Another global SD product—which is not available to public yet—is SMSA[2][101], which uses T_bs of AMSR2 onboard GCOM-W1. The methodology is built on Kelly et al. [100]'s prototype product, whereas snow depth is retrieved using DMRT-ML simulations using a cost-function minimization inversion approach while considering densification and grain growth trajectory which is adapted based on persistent presence of snow.

There are other noteworthy SD and SWE products that are based on synergistic approaches such as blending active and passive observations (e.g., [88]). Active microwave is an efficient tool for wet snow detection [175]; however, to employ active microwave observations in synergistic approaches, temporal resolution discrepancy between active and passive observations is a challenge that seems to be the primary reason why to date, no long-term global SD or SWE product has been retrieved via a synergistic active/passive microwave approach.

---

[1] Special Sensor Microwave/Imager

[2] Satellite-based Microwave Snow Algorithm

Table 4.1: An overview of global operational SD and SWE products by PM remote sensing

Snow product name	Temporal coverage	Retrieval Approach	Data Source
GlobSnow SWE	1979-present	Snow depth from synoptic weather stations are kriged and then used to optimize snow depths in a Bayesian framework using SMMR, SSM/I, SSMIS, and AMSRE observations and HUT simulations [159, 201].	[4]
AMSR-E/Aqua Global SWE (NASA)	2002-2011	Multiple ancillary data is collected to create a base map for screening snow pixels and and then series of tests are conducted to detect snow pixels and retrieve snow depth based on empirical relations built on Chang et al. [25] algorithm	[207]
Standard SD and SWE AMSR-E and AMSR2 (JAXA)	2002-2011	Snow depths are retrieved via an empirical modeling. To estimate SWE, daily SD is multiplied by an average density map that is created using WMO SD measurements and Sturm's snow classes [98].	[1]

---

[1] Special Sensor Microwave Imager

[2] Satellite-based Microwave Snow Algorithm

4.5 Error and Uncertainty Estimation of Retrieval Products

Passive microwave sensors are advantageous in retrieving SWE estimates, however, sources of error must be examined, and uncertainties need to be quantified to fully understand the applicability of PM snow depth and SWE estimates. It is understood that variables such as forest cover, grain metrics parameterization, snowpack stratigraphy and metamorphism, vegetation cover and proximity to large bodies of water directly influence the uncertainty of PM snow depth retrievals and numerous studies have focused on quantifying these sources of error and developing methods to assess the accuracy of PM snow property retrievals [36, 45, 71, 113, 14]. Common accuracy assessment methods include comparing PM spaceborne snow depth or SWE retrievals to true values obtained from *in situ* measurements from extensive snow surveys or permanent snow stations, airborne PM observations and statistical algorithms. Given that permanent weather stations are usually situated in open clearings, snow depth and density are not directly measured at most stations, and at coarse spatial resolution of PM, *in situ* SWE observations can be misrepresentative of the PM footprint. It is suggested that only PM footprints with multiple *in situ* observations be used for validation purposes, since the accuracy of *in situ* observations within a footprint increases as the number of *in situ* sites increases [45, 23].

Extensive season-long *in situ* field and airborne campaigns can be more robust for accuracy assessments to minimize the misrepresentation errors as well as uncertainties related to microstructural changes. The best efforts to evaluate passive microwave-derived snow accumulation products are field catchment sites typically managed by government research laboratories and are high expense facilities which minimizes the spatial coverage. However, sites in Finland (Sodankyl), Canada (e.g. Trail Valley Creek NWT, Churchill MB), USA (e.g. Fraser CO, Kaparuk Basin AK, Reynolds Creek ID), Russia (Yakusk Siberia) serve this purpose well and have been used to evaluate satellite-based observations of snow accumulation [197, 24, 131, 55, 104, 118].

Collaborative projects and field campaigns such as the Boreal Ecosystem-Atmosphere Study (BOREAS) [188] in 1994 winter field campaign and the Satellite Snow Product Intercomparison and Evaluation Exercise (SnowPEX) [39] have been initiated to gain further insight into the uncertainty involved with snow retrievals using spaceborne PM observations. BOREAS involved the acquisition of both *in situ* and airborne snow depth measurements that were compared to spaceborne PM snow depth retrievals and was one of the first accuracy assessment studies to be performed [22]. SnowPEX is an ongoing project, funded by the European Space Agency (ESA), which is focused on quantifying the uncertainty of satellite derived PM SWE products in the Northern Hemisphere by combining *in situ* datasets from around the world [144, 146, 39]. Other field campaigns such as the Cold Land Processes Field Experiment (CLPX) and the SnowEx Campaign, although not specifically designed for quantifying uncertainty of spaceborne PM snow depth retrievals, have been used to validate some snow depth and SWE products, and have continuing potential in future uncertainty studies [220, 17].

Given the lack of large scale *in situ* or airborne snow depth and density measurements, validation studies have typically been carried out on a local scale. Additional datasets available for quantifying retrievals uncertainties include the Snow Survey Network Program for the BC River Forecast Centre, Environment Canada snow stations, the Finnish Environment Institute snow surveys, the Federal Service for Hydrometeorology and Environmental Monitoring of Russia (RosHydroMet), snow surveys and Snow Telemetry (SNOTEL) [189], and Snow Course Data in the United States [146]. Assimilated global SD of the Canadian Meteorological Center (CMC) by Brasnett [12] and Brown et al. [15] is another data source that is often used for accuracy assessments. Not a global project, but nevertheless noteworthy, is the SNOw Data Assimilation System (SNODAS) for the United States [10] that can be used for evaluation of SD products with coarser resolutions. Snow maps created by synergistic approaches, with integrated observations from PM and visible/infrared sensors, such as SD have been created by the US Air Force Weather Agency (AFWA)/NASA Snow Algorithm (ANSA) and can be used as a reference for uncertainty assessments [206, 73]. These datasets provide extended temporal *in situ* snow depth measurements that can be compared to PM snow depth retrievals to assess uncertainties in varying regions to assist in gaining a full understanding of the spatial and quantitative distribution of uncertainties.

4.6 Discussion and conclusions

PM remote sensing observations along with additional information such as snow grain metrics and density are significant data sources for snowpack physical properties retrieval. These additional datasets can be provided by ground-based measurements, other local-scale remotely sensed data, or model data [208, 145]. Grain growth and densification approximations, based on statistical analysis of the extensive field measurements provided by historical climatologic variables are examples of such prior information [199]. In addition, coupling snowpack emission models and physical models of snowpacks has been performed in different studies, such as those by Andreadis et al. [5], Langlois et al. [112], and Kontu et al. [106]. An experimental demonstration of snowpack models is presented by Essery et al. [58], providing a framework for using 1701 snowpack evolution models coupled to three different emission models. The accuracy of these coupled emission models was tested in Sandells et al. [180]'s work, which suggested that particular combinations of snowpack models and emission models should be considered in the design of retrieval processes. RA is another approach to address this problem by coupling snowpack physical models and emission models, however, until recently, there has been little interest in this technique. Broadly speaking, studies that use *a priori* information or assimilated *in situ* observations claim greater estimation accuracy than that is possible with stand-alone retrievals and find this approach crucial as it addresses the ill-posed nature of inversion problem [46, 204].

As previously mentioned, any accurate retrieval of land covers properties using PM observations requires employing an emission model or an empirical relationship based on physical explanations as well as data sources such as other remotely sensed observations, ground-based measurements, and climatology datasets. Point-based measurement networks can constrain coupled snowpack to emission models, leading to potentially increased accuracy of estimates by PM observations [11]. Relying on climatology information while using a physical emission model transforms the retrieval into an empirical treatment and snowpack physical properties are highly variable even at large scales, so specific care should be taken when different data sources are integrated as prior information in the retrieval process. Inclusion of a error covariance matrix in the inversion process or simply defining cost functions that include variances of key components in the retrieval let us control the reliance on the prior information.

Integrated frameworks that employ emission modeling and ground-based network data using assimilation techniques or the frameworks that couple emission and land surface models can be the solution to compensate for the low spatial resolutions of PM remote sensing. In terms of a retrieval problem, a systematic approach that can be applied on a global scale and allows quantifying the associated errors is the implementation of a probabilistic Bayesian framework. Such an approach brings the benefit of simplicity and tractability that is essential for global snow products and leads to the realization of the physically-based inversion in a probabilistic process.

To conclude, existing physical emission models have been increasingly developed and investigated for modeling microwave interactions with ice particles in a snowpack. However, this is a complex effort relying on spaceborne observations coupled with a sophisticated emission model and does not always result in an accurate retrieval. ML techniques are powerful tools in creating non-linear relations between sensitive T_bs and snowpack properties to leverage retrieval methods. However, lack of computational tractability of ML methods and a lack of simple deployment in their applicability to operational retrievals are barriers to their use. Emission modeling requires many input parameters to be measured, which is not feasible globally at appropriate spatial scales. Therefore, an open question persists regarding the way that detailed stratigraphic variables of a snowpack impact the T_bs at airborne/spaceborne scales. The ongoing long-term field experiments alluded to in this paper provide opportunities to evaluate this question. The real issue, then, becomes how these details should be generalized from small-scales and what is the characteristic nature of uncertainties that are tolerable for accurate (or acceptable) retrievals using PM Observations. This is now the fundamental issue that has to be resolved for effective progress to be made in passive microwave SWE retrievals.

Chapter 5

Modeling the Observed Microwave Emission from Shallow Multi-Layer Tundra Snow Using DMRT-ML

5.1 Introduction

Tundra snow cover is a key variable in the cryosphere that can significantly control local to regional scale surface water balances, energy fluxes, as well as ecosystem functioning and permafrost dynamics [165]. At regional and global scales, snow cover affects atmospheric circulation through variations in radiative forcing and the snow-albedo feedback effect [28, 64]. While satellite-based mapping of snow cover extent is routine, satellite based mapping of snow water equivalent (SWE) is less mature and it is still challenging to estimate snow accumulation regionally and globally to the desired accuracy that can inform climate change or catchment-based hydrology applications. Significant progress has been made in this area [201, 98, 208, 159], yet there is still uncertainty in the retrievals, primarily because the spatial resolution of the observation, most notably from passive microwave (SWE) instruments (regional-scale), does not match the spatial resolution of SWE variability (local-scale). Furthermore, there are uncertainties in the retrieval process likely linked to the unique snow properties found in certain environments, such as the tundra snow, which accounts for 16% of the total northern hemisphere land surface [199, 200].

Snow micro-physical structure (depth, grain size, density and temperature profile) evolves during the winter season. *In situ* measurements of tundra snow properties reported in previous studies[165, 37, 40] provide a reference for tundra specific emission modeling with studies showing that one layer of early season snowpack develops to two predominant layer types of slab and hoar, as a result of kinetic grain metamorphism due strong vertical temperature gradients [199]. A fresh or recent snow at the surface of the pack is subject to wind redistribution [38]. The slab fraction increases even with increased overall pack depth, and as a multi-layer medium, the discrete layers in the snow add complexity to the bulk microwave emission from the pack since each snow layer evolves differently as the season progresses and from year to year.

In terms of the general microwave emission from a typical low to moderate density dry snowpack, an increased snowpack thickness from progressive snow accumulation manifests itself as a decrease in microwave emission at shorter wavelengths (>25 GHz), as measured by the brightness temperature (T_b). This is because the microwave scattering coefficient dominates the emission process. However, beyond a threshold of SWE, the T_b increase as emission from the snowpack increases the T_b and overrides the scattering signature. In shallow tundra snow, unique layering characteristics coupled with high density, slab-dominated snowpacks produce an increase in the T_b response, as the winter season progresses, at shallower snow depths relative to other environments such as the boreal forest or alpine regions.

The slope reversal from decreasing to increasing T_b at 37 GHz with increasing snow accumulation has been observed in a limited number of studies. Rosenfeld and Grody [169] discussed the inflection behavior observed by the Special Sensor Microwave/Image (SSMI) as an anomaly in microwave spectra and simulated the inverted T_b applying Dense Media Theory (DMT) radiative transfer approach successfully for a two-layer snowpack of crust and aged snow. This work provided limited details on the *in situ* measurements. Derksen et al. [40] explored the seasonal 37 GHz T_b slope reversal in an empirical fashion for spaceborne SWE retrievals based on cumulative absolute difference of T_bs. Using a physically-based approach, Liang et al. [124] applied the Dense Media Radiative Transfer approach based on the quasi-crystalline approximation (QCA) with stickiness to simulate T_bs from multilayered stratified medium depth to deep snow (∼4080 cm). They demonstrated the T_b inflection behavior, which was driven by ground based snow microstructure measurements of a multi-layer pack with larger grains at depth and smaller ones above with lower densities. However, Liang et al. [124] used a multilayer simulation (>6 layers) with exact input variables for each layer from *In situ* measurements. While the approach yielded good results, physical stratification of the snow adds significant complexity to the model implementation and may lead to overfitting in the process of finding the best correlation between simulations and observations. Therefore, model applicability to airborne or spaceborne observations for snow depth retrieval is not straightforward. Moreover, the representation of slab on depth-hoar that is frequently seen in tundra environments, is less well tested by these models.

Determining the stratigraphic and microstructure layering of snow, at least in general form, is an operational prerequisite if physical modeling approaches are to be used in SWE retrievals. While the study by Derksen et al. [40] explores the empirical evidence of the T_b reversal at 37 GHz, it does not attempt to explain the T_b response from a physical perspective while the Rosenfeld and Grody [169] study does not provide any direct experimental evidence of the existence of a dense layer, except through inference from T_b variations observed from satellite T_b measurements. Therefore, this study develops the ideas of Rosenfeld and Grody [169], Derksen et al. [40] by parameterizing and testing a physically-based model that predicts the T_b response, including the T_b slope reversal from an Arctic tundra snowpack using DMRT-ML and *In situ* snow pit observations. The model results are compared and validated against coincident multi-resolution airborne microwave T_b observations. The goal of this research is to be able to apply this model in a manner requiring only a minimal parameterization scheme that is independent of ground-based data for satellite SWE retrievals.

5.2 Methodology

5.2.1 Description of the DMRT-ML snow emission model

Electromagnetic radiation passing through a multi-layered dry snowpack medium can be modeled by scattering, absorption, reflection, refraction and transmission considering dielectric properties of the medium. Three different groups of empirical, semi-empirical and physical emission models have been developed to derive estimates of a snowpack's physical parameters using radiometry. Empirical models typically do not account for snowpack microstructure metamorphism, which significantly impacts the microwave signature of a snowpack. Semi-empirical and physical models of the microwave emission from snow have evolved as our understanding from experiments of snow microwave emission has improved and has been fed back to model design. The Dense Media Radiative Transfer Model-Multi-Layer (DMRT-ML) is a physically-based model that couples the microstructural properties of a snowpack to its emission signature. DMRT-ML has been employed in several studies using ground-based radiometers and *in situ* snow measurements [155, 171]. The Dense Media Radiative Transfer (DMRT) model [214] and DMRT-ML have also been employed and evaluated for SWE retrievals using spaceborne radiometry (e.g.,[100, 16]). However, using DMRT-ML to retrieve snow depth globally needs parameterization of the dynamic state of the snowpack. Observations from airborne radiometry together with *in situ* measurements on the ground makes it possible to constrain the DMRT-ML for inversion and snow depth retrieval.

DMRT theory was developed by Tsang et al. [214] for a layered snowpack, and was originally based on the Quasi Crystalline Approximation (QCA) of scattering behavior of particles in a dense medium, where the particles occupy more than 20% of the fractional volume [227, 94]. Picard et al. [155] employed Quasi Crystalline Approximation-Coherent Potential (QCA-CP) to model emission for a multi-layered snowpack in a range of 1200 GHz. QCA and QCA-CP approximations let us model particle positions pair distribution functions while coherent wave interactions are assumed. In so doing, these approximations allow wave interactions to be modeled in a dense medium [214]. For DMRT-ML, snow scattering and extinction coefficients and the form of the phase function are computed based on DMRT theory, whereby the radiative transfer equation, based on the work of Jin [94], is solved using the Discrete Ordinate method (DISORT) [20]. Our implementation follows the approach of a mono-disperse assumption in a grain size distribution within a layer with the empirical method for large particles [82].

The DMRT-ML model is implemented by providing snowpack inputs including grain size, density, physical temperature, and thickness of each layer. For ground-based radiometer studies this is straightforward because the radiometer typically senses an instantaneous field of view (IFOV) of the order of a few meters at most, depending on the target-sensor separation. However, at the spatial scale of airborne observations (with typical IFOVs at the 100 s of meters) the spatial and temporal variability of snowpack physical properties can make it challenging to constrain the DMRT-ML model parameter set. This might also be exacerbated by spatial miss-match between flight lines and ground measurements. By characterizing the spatial variability of snowpack properties from field data using information given by a semivariogram, the spatial mismatch between observations on the ground and from air can be rendered acceptable by establishing geographical limits in the analysis beyond which ground and air observations should no longer be compared directly because they are too far apart and no longer spatially autocorrelated.

Accurate DMRT-ML model parameterization is of the utmost importance. Ground-based measurements of snowpack properties do not always match model input requirements. For example, one of the most commonly measured snow grain metrics observed by snow surveyors in the field is the maximum physical dimension(s) of the snow grain. Unfortunately, this metric cannot be directly input into the DMRT-ML model which represents the snow grains as spheres. Current research in this area is attempting to resolve differences between different snow grain size representations and how these differences influence model results [176]. Standard snow grain size measurements protocols need to be established because: (a) the models require a more sophisticated representation of snow grains (optical grain size, correlation length, specific surface area (SSA); and (b) the traditional observed measurement of the maximum dimension of the snow grain is inherently subjective depending on the surveyor and can vary between different surveyors using the same sampling equipment [71, 49]. A simple scaling factor has been developed by Roy et al. [171] to convert measured SSA [75] to effective grain size into DMRT-ML. While it is recognized that this scaling factor is optimized to produce the best results with the given snow survey data and may not be applicable to other snow survey data collected in different regions, it provides a starting point for defining snow microstructure inputs to DMRT-ML.

5.2.2 Data Analysis Workflow

This study investigates the DMRT-ML model performance over a high Arctic tundra snowpack by comparing simulated T_bV37 GHz results with airborne T_bs measured at moderate resolutions and spaceborne T_b observations at coarse resolutions. The objective is to characterize and predict the observed T_b slope reversal in emission behavior at 37 GHz for tundra snow using the DMRT-ML model. The methodology workflow includes: (1) the pre-processing of airborne observations to match with snow surveys; (2) the generalizing of snowpack characteristics for emission modeling; (3) DMRT-ML parametrization; (4) analyzing the emission behavior of tundra snow in the study area using airborne observations; (5) implementing the DMRT-ML model in selected sites and then in all footprints with significant number of snow depth measurements; and (6) analysis of the AMSR-E T_b V 37 GHz signature of the study area through the same snow accumulation season.

5.3 Data and Data Processing

5.3.1 Study Area

Snow survey and passive microwave airborne brightness temperature measurements were made across the Fosheim Peninsula, near the Eureka weather station on Ellesmere Island (∼ 80○ N; 84○ W) between 13 and 22 April 2011 (Figure 5.1). The region is cold and dry with an average annual air temperature at the Eureka weather station of 18.8°C and total yearly precipitation of 79 mm (19812010), with almost 60% falling as snow. The snow survey study area centered on a previously studied inland drainage basin, Hot Weather Creek (HWC), approximately 30 km inland from the weather station [40, 234, 233, 52]. The HWC study area has been described as a polar oasis within the High Arctic polar desert because of its unique geography of being protected by surrounding mountain ranges resulting in less cloud cover and warmer temperatures and subsequent abundance of vegetation compared to the surrounding High Arctic environments [52, 233]. However, despite the greater presence and variety of tundra vegetation in this region relative to other regions of the High Arctic, the main controlling influence on the depth and distribution of snow across this region is local scale topography, as existing vegetation is extremely sparse (bare ground), or is very low-lying [234]. The terrain of the study area is generally flat land consisting of upper plateaus, gently rolling hills and long slopes of varying aspects, accounting for approximately 90% of the study area, with the remain 10% made up narrow incised river/stream drainage channels draining into flat wetlands, lakes and valley bottoms [233]. The Fosheim Peninsula is only approximately 75 km wide, but the extent of the generally flat terrain is large and far enough away from the coast to minimize the influence of the sea ice and surrounding mountain ranges on satellite-scale passive microwave swath data [232], and includes the coverage of multiple re-sampled 25 km Equal-Area Scalable Earth Grids (EASE-Grids) [13].

5.3.2 Airborne Data

Airborne T_b data were acquired from dual-polarized 19, 37 and 89 GHz microwave radiometers mounted on the Alfred Wegener Institute Polar-5 research aircraft. The radiometers were aft-viewing at a 53° degrees incidence angle to simulate the earth-viewing characteristics of the satellite-based SSM/I and AMSR-E passive microwave sensors. The 19, 37 and 89 GHz radiometers all have the same 6° degrees half-power beamwidth. After instrument calibration using warm and cold targets, the calibrated brightness accuracy was reported as <1 K for the 37 GHz and 89 GHz and <2 K for 19 GHz radiometers. The aircraft was based out of the Eureka weather station from 19 to 23 April 2011. Aircraft positional information was recorded using an AIMMS-20 system recording GPS data and platform attitude information which were used to precisely calculate the passive microwave radiometer footprint locations on the ground. All positional information was collected using the WGS 84 datum.

Three flight plans were devised to record multi-scale measurements of high Arctic tundra snow using passive microwave airborne radiometers. These multi-scale measurements include the following flights:

1. Local-scale grid (33 km $\times 6km)lowaltitudeflight(\sim$350 m above ground level [a.g.l]),

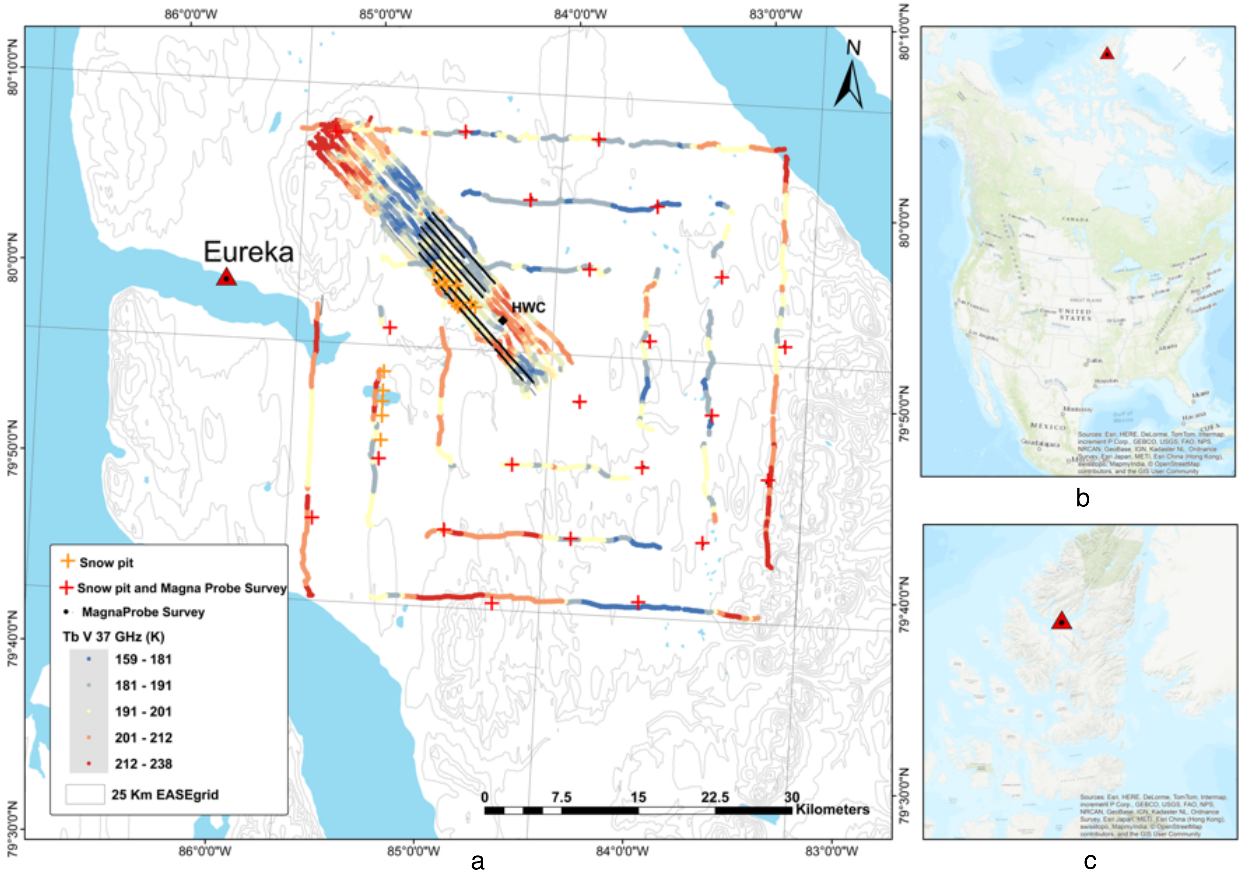

Figure 5.1: (a) Snow survey locations, snow pits and MagnaProbe transects, and EASE-Grid pixel boundaries; and (b,c) The location of the study area in North America and Nunavut, respectively

flown on 20 April

2. Local-scale grid (33 km $\times 6km)highaltitudeflight($∼2900 m a.g.l.), flown on 21 April.
3. Regional-scale grid 48 km $\times 48kmhighaltitudeflight($∼2700 m a.g.l), flown on 21 April.

Flights 1 and 2 constitute the local scale analysis data set while Flight 3 constitutes the regional scale analysis. Observations taken from a KT-19 infrared surface temperature sensor mounted on the aircraft with the same incidence angle and orientation as the high frequency radiometer were used in the regional scale modeling analysis to estimate the snow surface temperature. Figure 5.1 shows airborne flight lines, snow survey locations, HWC location as well as EASE grid pixel boundaries.

The approach used in this analysis to spatially link ground snow depth measurements to airborne passive microwave footprints is similar to that used by [37], where the IFOV of the airborne radiometer is calculated, and measured snow that falls within and around the bounds of this IFOV are linked to particular airborne measurement. The airborne radiometer's IFOV dimension is dependent on the aircraft's ground speed, altitude, roll, pitch and yaw, as well as the radiometer beamwidth, view angle, and integration time. The radiometer variables remain constant during data acquisition: beamwidth = 6°; view angle = 53°; and integration time = 1 s. The aircraft's altitude above sea level remained stable along each flight line, however due to changes in terrain height, the height above ground varied, but on average was approximately 350 m above ground for the low altitude flights, and 2700 m (regional grid) to 2900 m (local grid) above ground for the high altitude flights. Variables such as aircraft heading and speed varied slightly during each flight, but overall was quite consistent at approximately 155 nautical miles per hour (∼80 m/s). The aircraft's roll, pitch and yaw varied substantially during turns, with the radiometer's IFOV often pointed towards the horizon, rather than at the surface, and therefore these airborne measurements were removed from the analysis. If the airborne radiometer system was mounted on a stationary platform, the typical ground-projected IFOV for the low altitude flights would be approximately 100 m deep by 60 m wide. However, because the aircraft is moving, and the radiometer's have a 1-s integration time, the IFOV between two observations is elongated in the along-track axis, producing a "smeared footprint" [38]. The (smeared) footprint dimensions at low altitude were calculated as 120 m $\times 102m(along-track \times across-track)$.

The size of the footprints produced during the high altitude flights at $\sim$ 2900 m above ground was approximately 850 m $\times 510m.Figure$5.2$showsfootprintsintheEurekalowaltitudeflightgrid.$

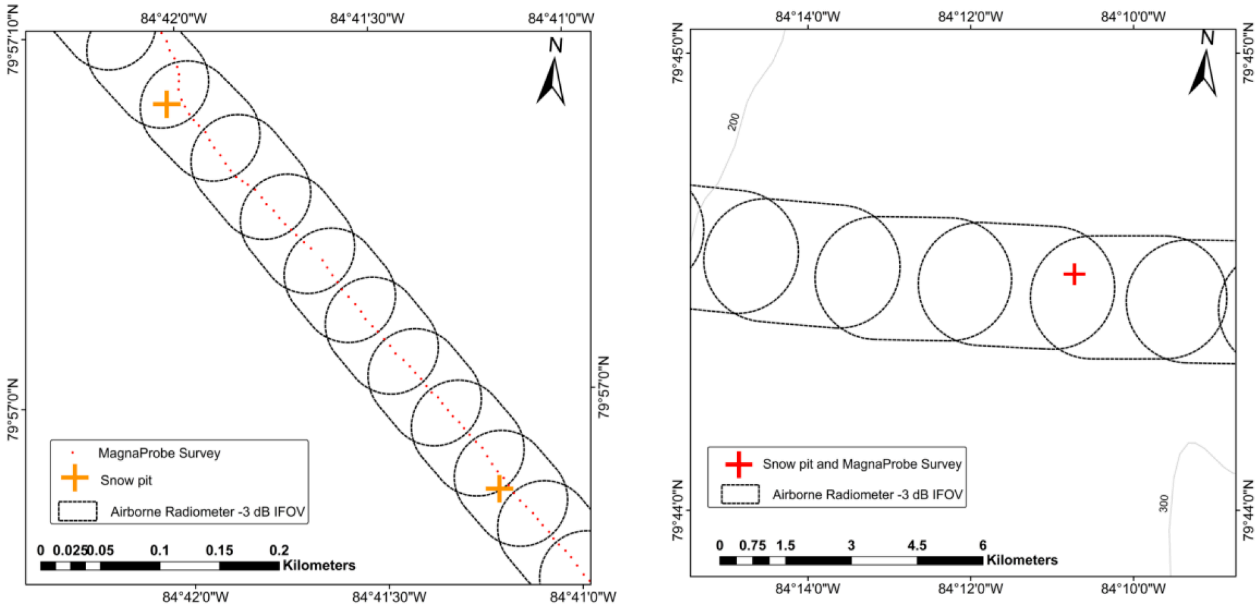

(a) **(b)**

Figure 5.2: (a) Example of projected IFOV of the airborne radiometer at low altitude ∼350 m; an average flight altitude for each flight line is used to calculate footprint dimensions. (b) Footprints of the radiometer at high altitude ∼2900 m after an average filter preprocess; an average flight altitude for the whole flight region is used to calculate footprints dimension.

from the airborne to the satellite scale and ensure complete coverage at different spatial resolutions of T_b products.

The lengthening of the radiometer footprint in the along-track axis is an important consideration when analyzing the high resolution, local-scale airborne data because the total number of snow measurements that fall within the radiometer's IFOV varies depending on the size of the IFOV. This effect becomes less important when working with coarser resolution airborne data because the extent of the IFOV becomes larger than the distance traveled during the one second integration time and therefore adjacent T_bs are heavily overlapped, leading to an over-sampled dataset. To reduce computational time when working with the oversampled high altitude airborne data, the data were thinned by taking the average of every 10 airborne observations. Consequently, the dimensions of footprints for these filtered observations were based on the average flight height for all 10 measurements (Figure 5.2b).

5.3.3 Satellite Data

AMSR-E/Aqua Daily EASE-Grid T_bs from 1 December to 30 April were downloaded from the National Snow and Ice Data Center (NSIDC; [105]) to produce seasonal time series of brightness temperatures. The AMSR-E/Aqua Daily EASE-Grid T_bs were produced from the interpolation method of Inverse Distance Square, using AMSR-E/Aqua L2A Global Swath Spatially-Resampled Brightness Temperatures (AE-L2A), projected into EASE-Grid (north and south Lambert azimuthal and global cylindrical) at 25 km resolution [105].

5.3.4 Ground-based *in situ* Data

Between 12 and 22 April, two types of snow surveys were conducted along the airborne radiometer flight lines. A regional-scale snow survey covering much of the Fosheim Peninsula was conducted via helicopter, with the purpose of evaluating the variability in snow properties at the 25 km EASE-Grid scale. The regional snow surveys involved snow depth transects and snow pits measuring snow properties including layering, density, temperature and mean geometrical maximum (D_{max}) grain size using a field microscope and a 2 mm comparator card, for 22 regional sites (these sites are presented by red crosses in the Figure 5.1). The regional snow conditions were relatively homogeneous; there was minimal terrain influence (generally flat), and no emergent vegetation above the snowpack was visible [40]. Snow depth was measured using a GPS enabled, self-recording snow depth probe [197],

Table 5.1: Summary statistics of the combined local and regional scale snow depth, density, and SWE measurements.

Statistics	**Depth (cm)**	**Density (kgm^{-3})**	**SWE (mm)**
Number of samples	15,251	576	576
Mean	26.9	246	67.0
Standard deviation	23.9	82	63.1
Coefficient of variation	89%	33%	94%

called a MagnaProbe. Depth measurements were made at 5 to 10 m intervals along a 100m sided-square centered on a snow pit. Total number of snow depth measurements made at each site ranged from 133 to 176 (average of 150) for a total of 2656 snow depths at all 22 sites. These measurements were used to determine the statistical distribution of snow depth at each site. An ESC-30 snow corer with a cross-sectional area of 30 cm^2 [59] was also used to record bulk SWE and density measurements at each site three times, for a total of 66 times.

The second type of *in situ* snow survey was conducted to characterize local-scale snow properties. The local-scale survey involved using a snowmobile to mark and set multi-kilometer snow depth/bulk SWE transects across the HWC study area, along the local grid airborne radiometer flight lines. A total of ten snow depth transects were surveyed, ranging in length from 2 to 15 km, with snow surveyors walking these lines and recording snow depths every 58 m and bulk ESC-30 SWE every 150180 m. Eight of these lines were parallel, spaced approximately 900 m apart, creating a multi-kilometer snow survey grid. A total of 12,595 snow depths and 510 bulk SWE measurements were recorded within and around this grid. A total of 27 snow pits were measured along the local scale survey transects, following the same survey protocol used during the regional helicopter surveys [40]. A summary of snowpack physical properties from the snow surveys is provided in Table 5.1. The high coefficient of variation (CoV) of snow depth measurements confirms high spatial variability in the region that will contribute to higher uncertainties in evaluating the microwave emission modeling results in this region.

The data summarized in the Table 5.1 differ from the data presented by [40] which reported exclusively on the regional-scale transects and snow pits. Table 5.1. gives the total summary statistics for all snow depth, snow density and SWE measurements from the Eureka field campaign used in this analysis. The measurements from the local scale transects were recorded mostly within a 33 km $\times 6kmgridwhiletheregional - scalemeasurementswererecordedacrossalarger48km \times 48kmgrid.Anadditionalfivesnowpitswereusedin$

The average number of layers identified in all 49 snow pits was five but there was a variety of different snow types that were observed; including: recent, fine-grained (F.G.), medium-grained (M.G.), crust, soft slab (S.S.), medium slab (M.S.), hard slab (H.S.), slab-to-hoar (Slab-Hoar), chains of hoar (indurated) (CoHI), chains of hoar, depth hoar and icy hoar. Typically, the upper snow layers (recent, fine and medium grained and crusts) are the thinnest while the mid-pack slab layers have largest densities and the middle and lower layers have the largest grain sizes.

To undertake the DMRT-ML modeling, the snowpack characterization had to be generalized. An unsupervised K-means clustering [129] of average grain size and snow density was conducted for 10 of the snow layer type classes (fine grained and icy hoar were excluded from the clustering because of the small sample size). The cluster analysis calculated five cluster means; this number of classes was set based on the average number of layers found in all pits. The hoar classes have cluster means that are low in density but have the largest grain sizes (and grain size range) while the recent and crust layers have the smallest grains and moderate density. The slab layers have the largest densities and the largest range of density values. Cluster 1 has very small layers with small grain sizes (top layer), while Clusters 2 and 3 have the largest densities (wind slabs) and Clusters 4 and 5 have the largest grain sizes (depth hoar).

For the DMRT-ML modeling, the upper cluster contained radiometrically insignificant layers since the layer thicknesses were small (7% of total thickness) and the grains were also very small. Therefore, this class was removed from the analysis for further generalization. The effect of a layer with small scatterers on top of thick layers with medium-sized grains is simulated by [124] where the 37 GHz T_b slope reversal was seen. They show that, when a snowpack is thick ($\sim$ 70 cm), a thin layer of new snow decreases attenuation of the ground emission, thus 37 GHz T_b increases, and, when a snowpack is shallow and composed of new snow, the emission (and T_b) decreases. It is noteworthy that, in all investigated cases discussed by Liang et al. [124], a topmost layer of new snow, at least 10 cm in thickness, was present showing consistency with our study.

The remaining four classes are further combined into two layers: slab (Clusters 2 and 3) and hoar layers (Clusters 4 and 5). The combined statistics for the slab and hoar layers are shown in the layer temperatures and densities for both structures, were relatively consistent with low coefficient of variations while layer thickness and the grain sizes had high standard deviations. The summary of generalized statistics is presented in table 5.2.

For the model inputs, it is necessary to use *in situ* forcing data (snow depth and snow pit) that are spatially coincident with the T_b observations. T_b observations represent snow emission from distributed areas across the radiometer's IFOV whilst *in situ* ground mea-

Table 5.2: Summary statistics of pits classified to two major layers merged from K-Means clustering results.

Layer Number	2 3			4 5 (base)			
Layer type	Soft Slab, Slab to Hoar, Medium Grained, Hard Slab, Moderate Slab			Chains of Hoar Indurated, Depth Hoar, Chains of Hoar			Bulk Total
Statistic (M,S,C)	M	S	C%	M	S	C%	
layer thickness (cm)	4.2	3.5	84	6.2	2.7	43	2.4
layer temperature (C)	-27.2	1.7	0.69	-26.7	1.6	0.6	-27.0
grain size long (mm)	0.9	0.6	62	5.6	2.4	43	2.4
grain size short (mm)	0.4	0.3	72	2	1.1	56	0.9
Density (kgm^{-3})	324	88	27	215.6	41	19	300.1

surements are made at the point scale. To evaluate the spatial variability of the *in situ* data (and determine the spatial representativeness of each *in situ* measurement) semivariograms of the MagnaProbe snow depths were calculated. Semivariograms provide an unbiased description of the scale and pattern of spatial variation of snow depth, determining what the threshold distance (range) is beyond which snow depths are no longer spatially autocorrelated. Figure 5.3 shows the semivariogram fitted with a spherical model highlighting the range to be at ∼58 m (range is identified where the variogram model line levels out). Snow depth (and snow structure from snow pits) separated by distances greater than the range value (58 m) are no longer spatially autocorrelated. To ensure a strong assumption of correlation between the *in situ* snow survey data and the airborne radiometer measurements the 58 m range value was used as an inclusion/exclusion threshold, where snow survey data within 58 m of the calculated radiometer IFOV were likely to be spatially autocorrelated to the snow found within the IFOV and therefore were used in this analysis. For snow depth data from MagnaProbe measurements, the CoV (%) of snow depth measured within each individual footprint varied from 22% to 100%, suggesting the presence of high spatial variability within a single footprint. Therefore, only snow depth within IFOVs were used. After screening, 38 out of the total 49 snow pits and 12,671 MagnaProbe measurements were used in the DMRT-ML model analysis.

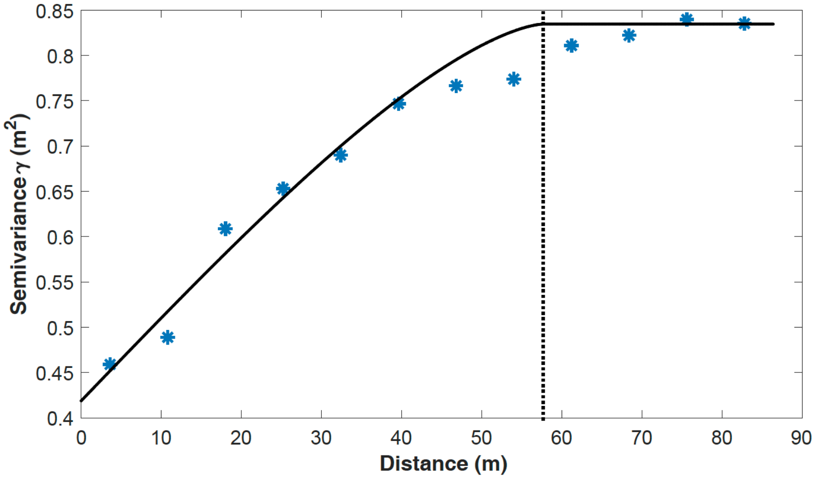

Figure 5.3: Averaged semivariogram of snow depth values for pairs with a seven-meter lag size and a fitted spherical model (black line). The range (58 m) is indicated by the vertical dotted line.

5.4 Results

5.4.1 Airborne Microwave T_b Observations of Snow Airborne

Airborne observations were used first to analyze the emission behavior of tundra snow in the study area. Figure 5.4 presents T_bs matched with coincident snow depth measurements sampled along the intensive flight paths for low and high altitude flights. In this study, only the vertical polarization at T_b 37 GHz response were studied due to less sensitivity to layering and ice lens structures in the snowpack than horizontal polarization [40,41]. In Figure 5.4a, each data point shows an average value of minimum 10 MagnaProbe snow depth measurements inside the footprint for a total of 601 T_bs with 6628 coincident depth measurements. When snow depth increases to about 20 cm, the T_b V 37 GHz signal decreases rapidly as scattering dominates the emission signal. Above this depth T_bs increase. To define this inflection point, a simple iterative regression equation search was applied to locate the depth at which the T_b was minimal based on the highest correlation coefficient (R). The best R correlation was -0.4 with a snow depth of 21 cm observed which equals SWE of 65 mm with an average density of 310 kgm^{-3}. At depths exceeding this threshold, T_bs increased, albeit with a relatively weak R coefficient (+0.1), in response to contributions of microwave emission from the snow itself. Both correlation coefficients are significant at the 95% confidence level.

This weak positive relationship between T_b and snow depth greater than 21 cm in this study area can be explained by wind slab formation, where emission is the main contributor rather than scattering. The high average value of measured slab fraction from the snow pit observations (50% from 26 sites) confirms this explanation. In a layer of wind-slab, mechanical processes of compaction dominate the upper layer metamorphism and snow is no longer an efficient insulating medium. The temperature gradient is very small and, therefore, thermal processes promoting snow crystal growth is minimized. While depth hoar is expected to continue to contribute to the signal, its effect is moderated by the overlying slab layer emission.

In Figure 5.4b, each point shows an average value containing MagnaProbe snow depth measurements inside the footprint in a total of 160 high altitude sample T_b's with 7,829 coincident SWE measurements. Footprints are much larger for high altitude IFOVs than the low altitude observations (by 700 times). *In situ* snow depth measurements are less representative of the IFOV's snow depth variability and, therefore, a higher level of uncertainty in characterizing the IFOV snow depth is likely. The R correlation between spatially correlated high and low altitude T_b V 37 GHz was 0.66. A 20 K standard deviation was calculated for low altitude T_bs found within the IFOV of high altitude footprints. The linear correlation coefficient of high altitude T_bs and snow depth is -0.25 over snow depth range of 0-20 cm and 0.12 for the depth of 20-90 cm (both significant at 95%).

5.4.2 Parameterization of the DMRT-ML

In the implementation of DMRT-ML, theoretical simulations of extinction and scattering coefficients are calculated based on the QCA-CP theory that can only solve small particle interactions with electromagnetic radiation with respect to Rayleigh scattering [155]. For larger grains (>1.6 mm) where QCA-CP is not applicable for Mie scattering, an empirical approach [82] is implemented in DMRT-ML imposing a limit for scattering efficiency. However, using simulated characteristics in this study, QCA-CP is valid for non-sticky grains assumption (Fig.6 Range of grain sizes for which the DMRT QCA-CP non-sticky is reasonably valid in [155]. In our simulations, it is assumed that soil layer's contribution in 37 GHz emission is minimal and snow extinction is dominant which occurs when there are numerous snow grains through emission (thick or very dense snowpack) and/or snow grains are quite large. In the tundra snowpack of the late snow season with depth hoar and slab layers, the aforementioned assumption is valid. Also, this assumption was evaluated using sensitivity analysis of the model to soil configurations (interface model, prescribed or modeled dielectric constant, and soil material), and the minimal effect of soil layer was verified. Here, in the DMRT-ML implementation, the snowpack is represented as a semi-infinite layer of high density snow slab over a layer of depth hoar. The combined pack is equivalent to the weighted average of the measured variables from the field site with different proportions based on different *in situ* measurements.

Having explored the airborne T_b observations, the DMRT-ML was used to simulate the T_b V 37 GHz response to replicate airborne and AMSR-E tendencies. The model was set up to be run for three broad scenarios, hereafter termed cases. Setup parameters for each case are summarized in Table 5.3. Density values were acquired from snow pit measurements based on Table 5.2. A range of grain size was used in all cases based on previous modeling studies to represent grain size parameterization [171, 177]. DMRT-ML requires the optical diameter (D_{opt}) of grain size as an input. However, human-observed *in situ* grain size measurements are typically recorded as a geometrical maximum (D_{max}) and minimum (D_{min}) dimension. There is currently no established methodology widely accepted to adjust D_{max} or D_{min} to values of D_{opt} [176]; and *in situ* data from this experiment were not extensive enough to optimize grain size using observations and simulations. Uncertainties in the representation of grain size, particularly when converting D_{max} to D_{opt}, are likely to be compounded when upscaling to the airborne footprint observations. Therefore, in this research, effective grain size (D_{eff}) that is a scaled value of D_{opt} justified for snowpack's

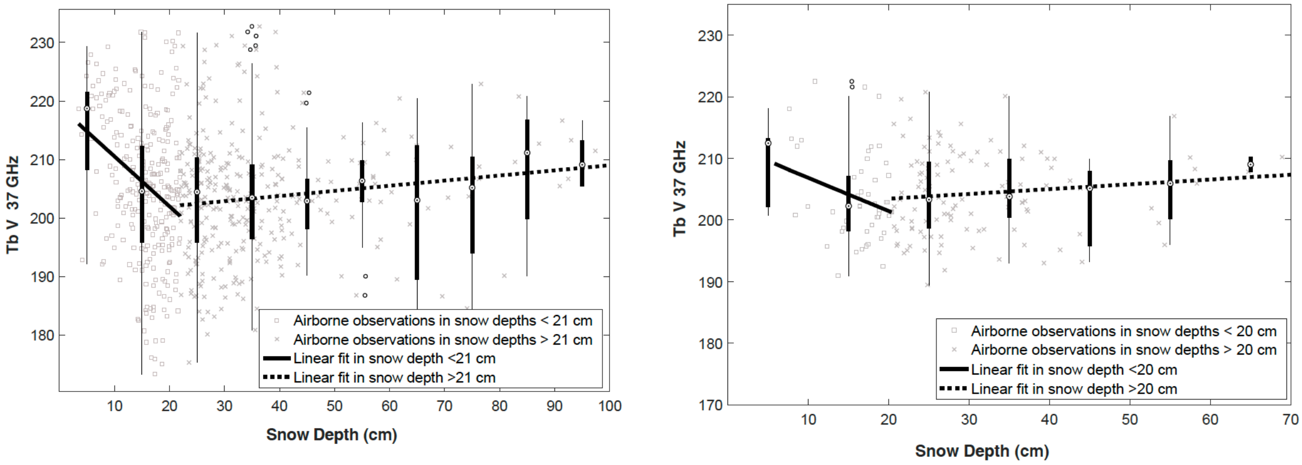

(a) **(b)**

Figure 5.4: Measured snow depth coordinated with footprint in T_b V 37 GHz from (a) low altitude T_b data, and (b) high altitude T_b data and boxplots of snow depths grouped by 10 cm.

microwave emission models is used. The physical temperature range measured in all snow pits was a maximum of 2 K. Therefore, for the DMRT-ML model simulations the average temperature for all 49 snow pits over the nine days was calculated (247.0 K) and used for the parameterization experiments.

In case 1, depth hoar development and subsequent 37 GHz volume scatter was simulated in a single homogenous layer model by running the model with increasing grain sizes, using a constant density of 300 kgm^{-3}. Snow depth was increased from 10 to 50 cm and the grain size was increased from 400 to 1000, resulting in a decrease in T_b V 37 GHz (Figure 5.6a). In case 2, the same grain size and snow depth inputs as case 1 were used, but this time a two-layer model that maintained a 2:1 ratio of wind-slab to depth hoar as depth increased was run to simulate early season snowpack evolution as a more realistic simulation (Figure 5.6b). For case 2, the slope of T_b-snow depth relation using relatively large grain sizes of 800-1000 [171], which should be employed for DMRT-ML modeling of a snowpack that contains depth hoar, is less than for case 1 which better matches the observations in Figure 5.5. In case 3, a simulation representing the mid-to-late season snowpack evolution where the wind slab layer grows, while the depth hoar layer thickness remains stable was modeled by running a two-layer snowpack with a fixed depth of the underlying depth hoar layer (7 cm) and a progressively increasing wind slab layer thickness (Figure 5.6c). To simulate the rise of T_b with depth increase in a two-layer snowpack, based on our simulation runs, the minimum depth for the depth hoar layer is calculated as 7 cm which is measured as 6.2 cm for the average depth of base layer (Table 2). The progressively growing wind slab increased the absorption coefficient and decreased the scattering coefficient with a net effect of decreasing the extinction coefficient. It should be noted that while formal DMRT theory related to highly compacted snow with densities in the range of 300-500 kgm^{-3} is imprecise, however, the model formulation uses a technique to approximate the coefficients at this range following the methods of Picard et al. [155].

The simulation approach for cases 2 and 3, when taken together illustrate a tendency that agrees with field observations showing the drop and rise in T_b with increased snow accumulation, as demonstrated documented in previous studies such as [165, 28, 64, 201, 98, 208, 159, 199, 200, 37, 40], and as illustrated by the field measurements presented in Figure 5.6. Simulation case 2 and 3 form the basis for the comparison between simulated and observed T_bs at the regional and local scales in section 5.4.3.

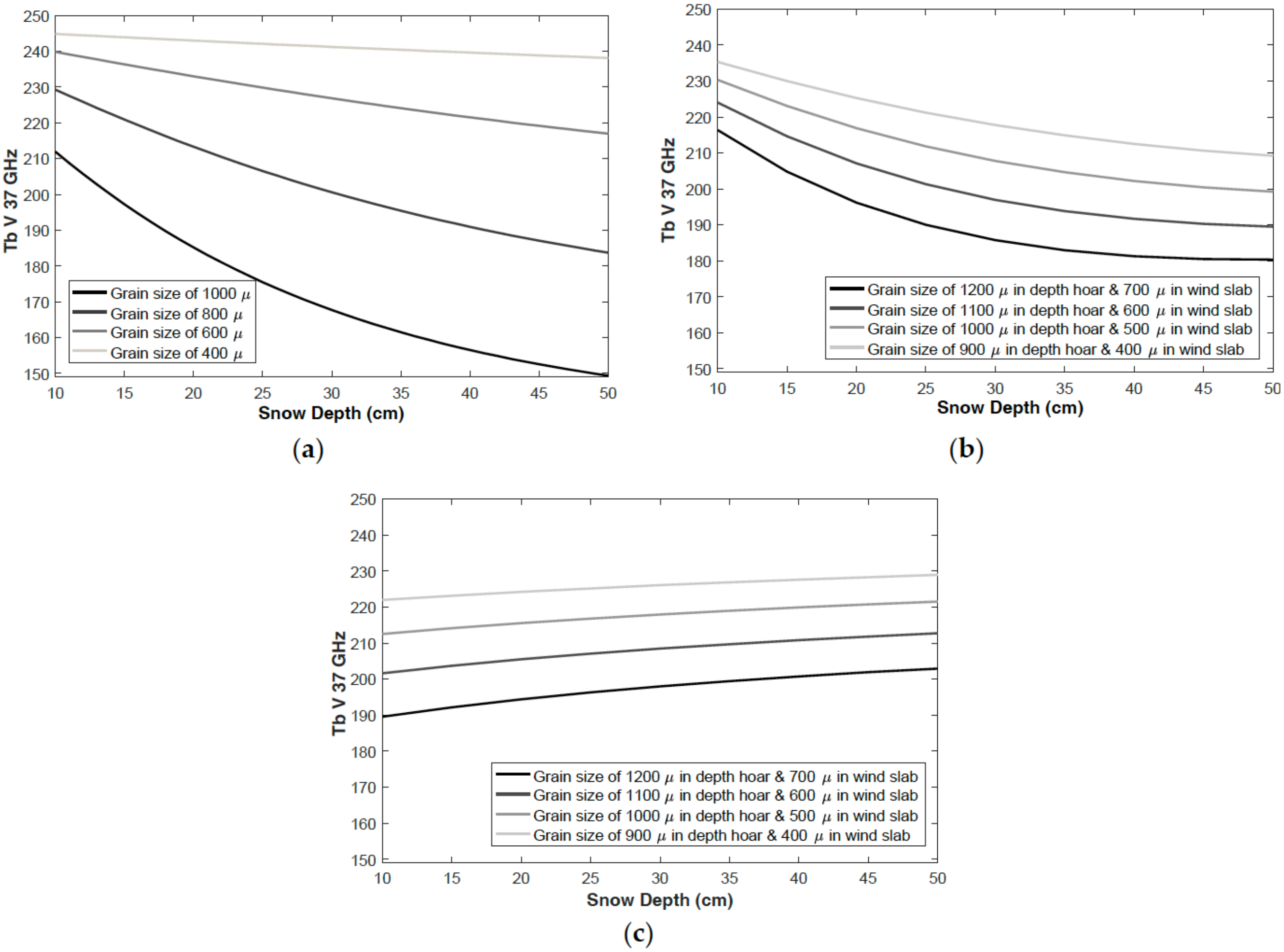

(a) (b) (c)

Figure 5.5: DMRT-ML simulations of the three experiment cases: (a) depth hoar formation simulation using a single snow layer; (b) two-layer snowpack of wind slab and depth hoar with a wind slab to depth hoar ratio of 2:1; (c) two-layer snowpack of wind slab and depth hoar with static depth hoar of 7cm.

Table 5.3: Three cases input parameters for DMRT-ML.

	Case 1: One layer: Depth hoar development	Case 2: Two layers: Static wind slab to depth hoar ratio 2:1	Case 3: Two layers: Static 7 cm depth hoar with a thickening wind slab
Effective Grain size	400 m- 1000 m	Wind slab: 400 m- 700 m; Depth hoar: 900 m- 1200 m	Wind slab: 400 m- 700 m; Depth hoar: 900 m- 1200 m
Density	300 kgm^{-3}	Wind slab: 324 kgm^{-3}; Depth hoar: 215 kgm^{-3}	Wind slab: 324 kgm^{-3}; Depth hoar: 215 kgm^{-3}
Snow depth	10cm - 50 cm	Wind slab: 3.3-16.6 cm; Depth hoar: 6.6 -33.3 cm	Wind slab: 3-43 cm; Depth hoar: 7cm
Temperature	Constant at 247.0 K		
Substratum	Soil model= None; Semi-infinite snowpack		

5.4.3 Comparison of DMRT-ML Modeled T_b with Observations Snowpack

Snowpack data from 38 pits coincident with airborne T_bs (see Section 3.4) were used to simulate the T_b V 37 responses that coincided with the high and low altitude airborne radiometer observations. To reflect small variations in snowpack physical temperatures over the study domain, the average physical temperatures of 246.6 K and 247.4 K were used for the local and regional scale model simulations respectively. Depth hoar and wind slab layer influences on emission were simulated using two-layer snow packs as demonstrated in section 4.2 via case 2 (depth hoar formation) and case 3 (wind slab development). Based on *in situ* measurements and a cluster analysis (Table 4), the average snow density of 215 kgm^{-3} and 324 kg^{-3} were used for depth hoar and wind slab layers respectively. Effective grain size (D_{eff}) values are used based on previous studies with similar snowpack characteristics. Representative grain size values were used for a wind slab layer and depth hoar layer characteristics defined by [171]; the optical grain size (D_{opt}) was set to 330 m for a depth hoar and 170 m for a wind slab layer. These values were scaled by a factor of 3.3 [171] to achieve the effective grain size (D_{eff}) of 561 and 1089 respectively.

Figure 5.6 presents a scatterplot of simulated vs. observed T_b of depth hoar formation and wind slab development for both case 2 and 3. The correlation of 0.83 at a significance level of p-value=4×10^{-11} was found; with a 0.88 correlation value for case 2 and 0.61 for case 3 simulations. Footprints with data from snow pits at local scale observations (high and low altitudes) were simulated in case 3 since the snowpack was determined to be deeper and denser locally, while footprints with data from snow pits from the regional scale observations (high altitude) were simulated in case 2, due to the presence of snow depths less than 21 cm (the previously calculated inflection depth). Data points in the scatter-plot are shown in two groups of depth hoar (case 2) and wind slab (case 3) simulations. Lower correlation of case 3 simulations is mainly due to the coarser spatial resolution of observations.

Figure 5.7 is a repeat of Figure 5.4a with the T_b V 37 GHz simulations from Figure 5.6 overlain to show how the depth hoar and wind slab dominated snowpacks control the T_b V 37 GHz emission behavior measured by the airborne radiometer. The plot also includes, the model simulations for each airborne radiometer T_b IFOV with a minimum of 10 MagnaProbe snow depth measurements inside. Depth hoar development and wind slab formation were simulated using a two-layer snowpack as presented earlier. KT-19 infrared surface temperature measurements recorded coincidently with each airborne T_b were used as model inputs for snowpack temperatures. The simulation results using the airborne KT-19 snow temperatures inputs produced parallel patterns of simulated T_bs that can be seen in (specifically in the case 3 wind slab growth simulations). These parallel patterns of T_bs are a result of small variations in KT-19 snow surface temperatures between areas along the flight lines, highlighting the model sensitivity to this input variable. Overall, the model simulations of T_b have a smaller variance compared to observed airborne T_bs due to a smaller range of snow density, and grain size used as model inputs which arises from the generalization process of the *in situ* snow survey data.

The non-parametric test of Kolmogrov-Smirnov (KS test) was run to compare simulated and observed T_b V 37 GHz with the null hypothesis, H0, that observations and simulations come from populations with the same distribution, and an alternative hypothesis that the cumulative distribution function (CDF) of observations is larger than the CDF of the simulations. The test returned value of H0 = 1 which indicates KS test rejects the null hypothesis, in favor of the alternative hypothesis that the CDF of the observation is larger than the CDF of the simulations, at the default 5% significance level. The rejection of the null hypothesis can likely be explained by the presence of random errors as well as simplified snow properties/variability that are not represented by the generalized DMRT-ML model forcing data.

5.4.4 Application to AMSR-E Time Series Data Satellite

Satellite AMSR-E T_b V 37 GHz observations (AMSR-E 36.5 GHz frequency is rounded up and reported as 37 GHz for convenience) covering the study area were obtained to

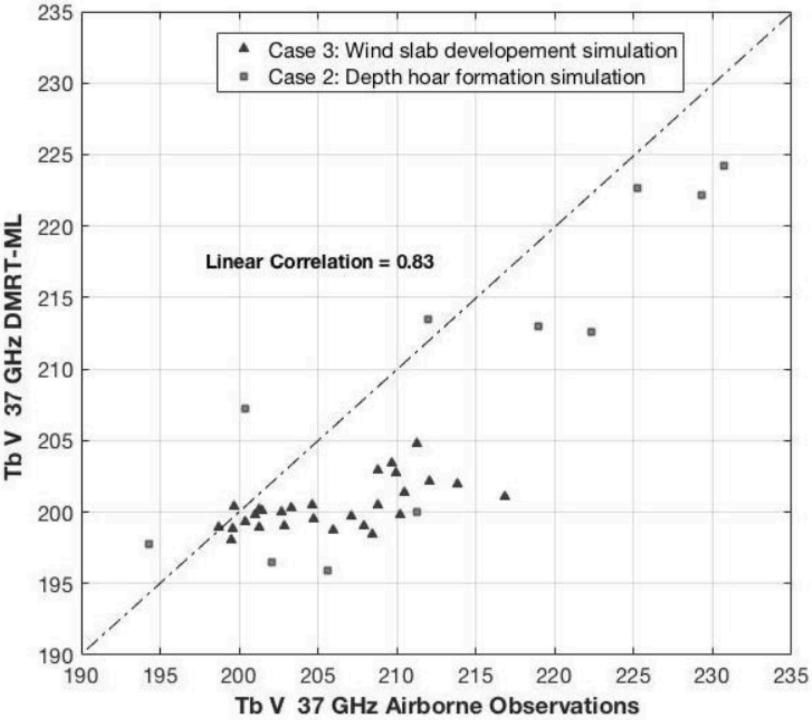

Figure 5.6: Simulated vs. observed 37 GHz T_bs (vertical polarization) for individual airborne footprints with data from 38 snow pits and associated MagaProbe measurements. Squares show case 2 simulations with a two-layer model with fractions of 2:1 ratio of wind slab layer to depth hoar. Triangles show case 3 simulations from a two-layer wind slab and depth hoar pack with fixed depth hoar thickness. The 1:1 line of agreement is shown as the dashed line.

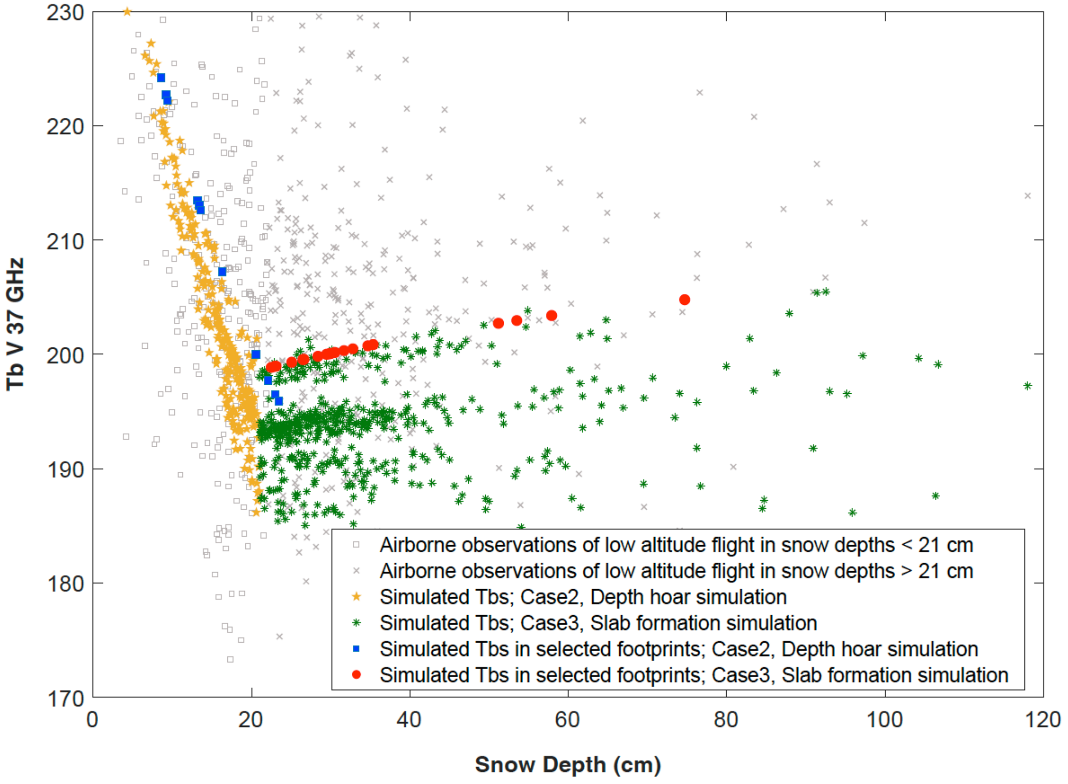

Figure 5.7: T_bs from airborne observations and simulations of all footprints using generalized density, physical temperature and grain sizes along with MagnaProbe data. All simulated T_bs are superimposed over the observed T_b V 37 GHz data from low altitude flight passes, also, T_b simulations from Fig. 6 superimposed over the observed T_b V 37 GHz data from low altitude flight passes.

illustrate the T_b trend throughout the whole snow season (December-May) (5.9). Error bars represent the standard deviation of the four AMSR-E footprints covering the study area. Air temperatures measured by Eureka weather station are also added to the right hand axis. Figure 5.8 shows a gradual decrease in early to mid-season, and an increase afterwards. The high correlation of 0.84 between air temperature and T_b V 37 GHz indicates that T_bs are dominated by surface temperature and interpretations using these T_b values about snowpack's metamorphism are spurious. The error bars increase in size from March through to the end of the season likely as a result of high variation in two of the four pixels; one has a moderate topographic heterogeneity (900 m variability) and the other has the greatest adjacency to waterbodies. The regional airborne T_b observations covering these pixels also had the highest standard deviation compared with the other regions in the study areas.

To characterize the impact of background emission on Figure 5.8, differences between T_b V 37 GHz and T_b V 19 GHz (abbreviated to $\Delta\ T_b$) are used and shown in Figure 5.9. This difference is typically used to represent emissivity processes in the snow. In Figure 5.9, snow survey data recorded by the Eureka weather station on the 1st and 15th of every month are added to the right-hand axis for comparison. Error bars show the standard deviation of the 10 snow depth measurements made on each day and indicate that heteroscedacity is present. After an increase in snow accumulation during December, the record is characterized as a period of gradual snow depth increase until the end of the record on April 30. Through the same period, $\Delta\ T_b$ shows gradual decrease in $\Delta\ T_b$ until middle to end of February. This decrease is interpreted as being the result of the combined effect of snow accumulation and snow grain metamorphism of the depth hoar layer which enhances the scattering of subnivean soil emissions. From mid to later February, the $\Delta\ T_b$ signal increases likely, as the wind slab layer increases in depth, relative to the depth hoar layer. The increasing thickness of the wind slab reduces the penetration depth of the 37 GHz V signal, and the scattering effect of the depth hoar is suppressed by the emission component of the high density, small grained wind slab. The snow survey data at the Eureka weather station verifies that on February 1 the average snow depth exceeded 23 cm which is very close to the defined threshold of 21 cm found in the airborne data (see Section 5.4.1). Although the $\Delta\ T_b$ in Figure 5.9 has physical temperature effects reduced, residual variability can be explained by the variations in physical air/snow temperature, snowfall events, and local snow redistribution processes.

An interesting interpretation of Figure 5.9 is that the increased emission of wind slab can be explained by spatial processes observed through a field experiment and a temporal process from consistent satellite observations. The temporal process of increasing T_b V 37 GHz and $\Delta\ T_b$ during the late accumulation season was shown by [169] from SSM/I

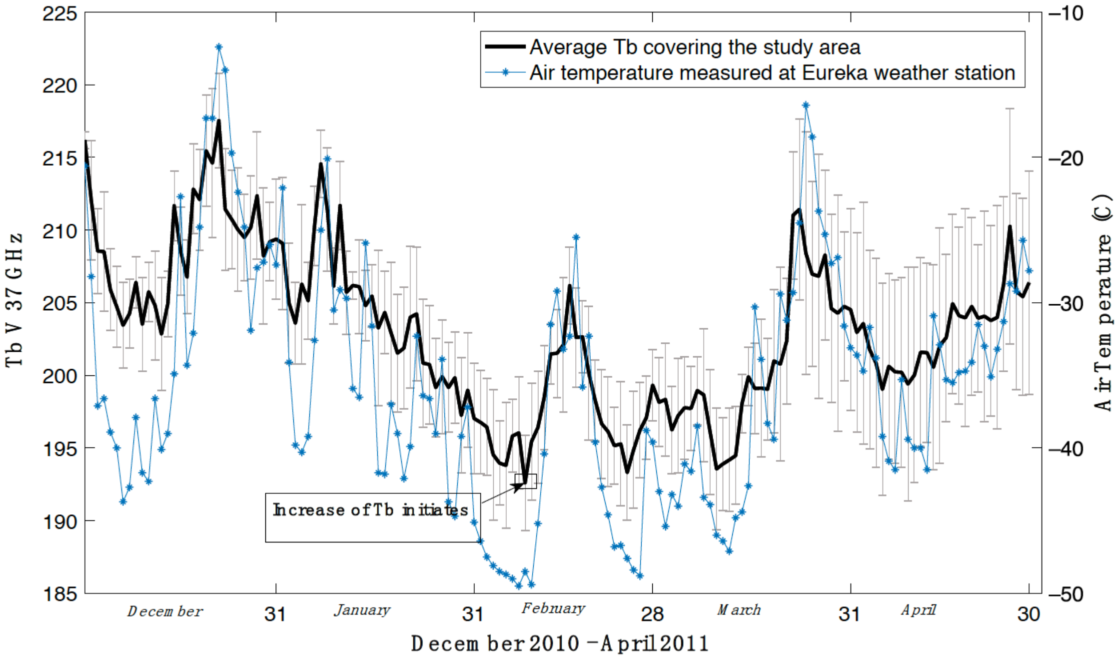

Figure 5.8: Average of 2 $\times 2 footprint AMSR - ET_b$s covering the study area with error bars showing the standard deviation.

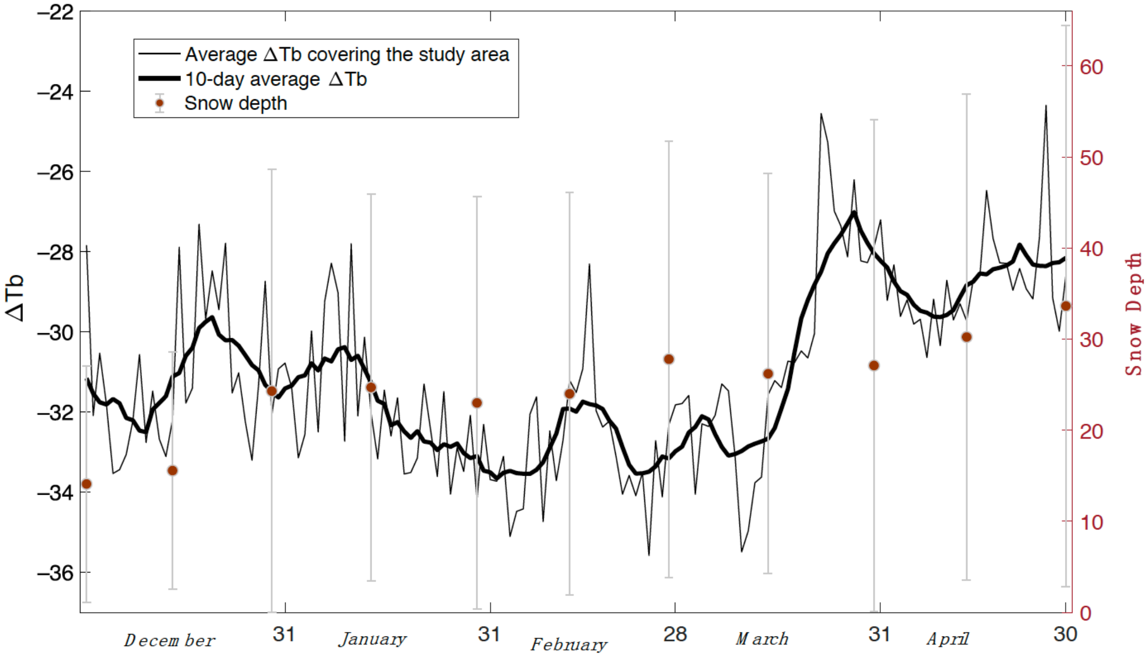

Figure 5.9: Average of 2 $\times 2 footprint AMSR-E \Delta\ T_b$ covering the study area, a 10-day average ΔT_b and an overlaid local snow depth measurements recorded by Eureka weather station.

observations. In their study, the accumulation of fresh snow was presumed to increase scattering, followed by metamorphic changes in crystalline structure that decrease the single-scattering albedo. They explained the T_b reversal, by presence of consolidated ice layers developed from subsurface melt-refreeze and overlaid on top of coarse-grained snow. While similar processes are present in Figures 5.7 and 5.9, the analysis of airborne measurements in the late season strongly indicates that a sharp decrease and a mild increase in emissivity can be explained first by the thickening of a depth hoar layer in the earlier (December mid-February) followed by the continued thickening of the wind slab layer after mid-February as the depth hoar layer remains relatively constant.

The Δ T_bs in Figure 5.9 are likely affected by the snowpack and or soil physical temperature. The use of emissivities (vertical and horizontal polarizations at 37 GHz) would help clarify this issue. To calculate the emissivities, the effective temperature of the snowpack and the brightness temperature of the sky are required but are not available for the complete AMSR-E record. The polarization ratio (PR) H-pol / V-pol at 37 GHz (the emissivity ratio of horizontal to vertical polarization at 37 GHz) could be calculated in lieu of emissivities to characterize snowpack microstructure properties and conclusively investigate the snowpack's self-emission. In a previous study [196], it was suggested that the PR can be used for density retrievals as its decrease and increase can verify the development of depth hoar and wind slab layers, respectively. However, due to the coarse resolution of AMSR-E observations and the high variability of snow properties in a footprint, PR values ranged from 0.90 to 0.95 with a low CoV(%) of 1 were not reliable enough for further analysis and interpretation.

5.5 Discussion

The DMRT-ML model was run using *in situ* measurements surveyed between April 13th and 22nd, 2011., and compared against airborne T_b observations measured on April 20th and 21st. Model and observation comparisons were made at 37 GHz frequency which is the most sensitive frequency channel to characterize moderate snow depth. Only the vertical polarization response were investigated since the microwave response from snow at T_b 37 GHz in vertical polarization is known to be less sensitive to ice lens structures in the pack than horizontal polarization T_bs [119, 177]. The DMRT-ML model successfully simulated the seasonal T_b V 37 GHz response from high Arctic tundra snow by separately modeling the depth hoar growth (case 2 simulations) and the wind slab development (case 3 simulations). The case 2 simulations modeled a two-layer slab and depth hoar snowpack with a fixed depth ratio of 2:1. Comparisons with observed airborne T_bs indicate that

DMRT-ML can be used to simulate the T_b V 37 GHz decrease with increasing snow depth up to 21 cm, whilst a two-layer slab and depth hoar with fixed depth hoar thickness (7 cm) and increasing wind slab thickness can successfully simulate T_b increases as the snowpack thickens beyond 21 cm which occurs more commonly later in the season. Finally, the AMSR-E time series response of Δ T_bs in the region, shows a declining in the early season followed by an inflection on mid-February after which the emission begins to increase in magnitude, which may presumably be in response to the continued wind slab growth as the season progresses.

The high spatial variability of snow properties observed in our study area is averaged across the footprint scale in the airborne T_bs observations. Inevitably, this causes the sensitivity of observed T_bs to be lower than the model estimates, when the model is driven by point-scale *in situ* snow pit measurements that have a high degree of spatial variability. Furthermore, even different footprint sizes acquired from the same location from different altitudes with the same sensor produce different T_bs because the underlying natural emission signal is variable. The calibration of a physical emission model using *in situ* snow pits will likely lead to uncertainties for larger scale applications. Therefore, it is necessary to develop robust schemes such as the unsupervised K-means cluster analysis to generalize snowpack structural elements that can be adopted for snowpack emission modelling and snow retrievals.

5.6 Conclusions

The obtained 21 cm threshold in the T_b-snow depth inflection is lower but comparable to other findings elsewhere. For example, Roy et al. [173] observed a 110 mm SWE (31 cm snow depth) threshold using ground-based observations. Rosenfeld and Grody [169] showed threshold minima of 20 cm and 45 cm using spaceborne observations in different case studies while explaining this phenomena as an anomalous signature and modeling it using a two-stream Dense Media Theory. However, no comprehensive *in situ* snow pit data with snow structural information were available to conclusively support these findings. In the study by Derksen et al. [40], a threshold of 130 mm of SWE was observed but neither averaged density nor equivalent snow depth were reported at the airborne observation scale (70 x 120 m). The range of differences is likely attributed to the differences between the sampling of high spatially variable snow properties at different scales: point ground measurements [200, 124] and area airborne measurements [37]. The presence of dominant wind slab layers with high snow densities in our study area likely resulted in a lower threshold for the observed 37 GHz T_b V inflection point, explaining why the inflection point of 68 mm of SWE (21 cm snow depth) was lower than those values reported in previous studies. The measured airborne T_bs and the DMRT-ML simulated slope reversal of T_b at 37 GHz, documented in this study suggests that this threshold, and the modeling approach taken, is generalizable to other Arctic tundra snow environments.

In this research, airborne observations and field data measurements were made over a ten-day period through almost consistent air temperature with likely negligible snow structural changes. Therefore, it is assumed that no metamorphism occurred during the field campaign period. However, in the presence of seasonal snow evolution, emission models of snow should account for snowpack seasonal metamorphosis. Various methods can provide estimates of snowpack structure (grain size, density) to couple with microwave emission models: the empirical densification approach of [200] and the grain growth model of Langlois et al. [112]; land surface models such as the Canadian land surface scheme [106] or snow microstructure models such as SNOWPACK snow microstructure model [96]; and seasonal / event densification and grain crystal development through using the snowpack's recent thermal history [100]. Each of these approaches can improve estimates of the state of the snow whereas there are limitations in large scale applications. Knowledge about this inflection point can inform these approaches and help constrain the retrieval process if a physically-based emission model is used. Future work should continue to develop strategies that improve the current explicit inverse solutions using generalizable models/methods for parameterizing snowpack structure.

Chapter 6

The use of a Monte Carlo Markov Chain method for snow water equivalent retrievals based on microwave emission modeling experiments of tundra snow

6.1 Introduction

Passive microwave remote sensing observations of winter landscapes have been used since 1979 to estimate snow accumulation. Regression-based techniques to estimate terrestrial snow water equivalent (SWE) have used empirical coefficients relating snow depth or SWE to brightness temperatures at 19 and 37 GHz frequencies [26, 99, 98].

These approaches have their limitations not least because they generally treat the snowpack as a single layer and do not account for complex metamorphic processes known to control the microwave emission from snow [124, 117]. Physically-based Radiative Transfer (RT) models are capable of modeling snowpack microwave emission accurately at point scales when provided with consistent state variables of a multi-layer snowpack. With increased fidelity in the application of these forward RT models, the successful estimation of passive microwave brightness temperature (T_b) responses from multi-layered snowpacks is deepening our understanding of the emission process. However, the application of forward RT models for explicit retrievals requires fully prescribed parameters of key emission parameters of snowpack such as grain size, density, physical temperature and thickness of each layer.

In the absence of complete spatial knowledge of these variables, while having T_b observations in only two or three frequencies sensitive to snowpack properties, retrievals must include estimates of all snowpack properties except one or two of those to be known to have a problem that is numerically solvable. One way to achieve this is to constrain RT inversion approaches for snow property retrievals from passive microwave observations by estimation of all snowpack properties except one or two unknowns such as snow depth and grain size (key emission parameters), then applying statistical methods and/or techniques that use iterative searches or machine learning optimization (e.g.[21, 208, 181]). In both methods, a cost function (a function of the difference between observed and modeled data) is minimized using linear or non-linear optimization approaches. Explicit inversions minimize the differences between observed and simulated emissions, by means of models such as a linear regression using least square methods. Key emission parameters are typically an unknown quantity and so can be estimated in the cost function minimizing process.

Additional information, empirical relationships or information from snowpack physical models can also be incorporated into the parameterization process of snow properties, which is imported into the inversion models as *a priori* knowledge. *A priori* knowledge can also be imported as a first guess to obtain the best fit in an iterative approach. This general retrieval approach is based on Bayesian probability theory which was first used for passive microwave estimation of snow by Pulliainen and Hallikainen [160] and then utilized in the Globsnow product [159, 201] that employs an emission model of Helsinki University of Technology (HUT). Radiance Assimilation (RA) is another technique that facilitates the integration of external data sources for SWE estimation by coupling snowpack physical models and emission models [47, 122].

Among the available inversion approaches for retrievals, methods that include prior information in a probabilistic framework rather than constraining variables using estimations are preferable as they can generate probability distributions of observable states. The result generates a probability distribution based on an iterative search of the full or subset of the full parameter range as well as retrieval uncertainty. Such approaches can employ multi-layer snowpack representations whilst more empirical retrieval methodologies such as one developed by Kelly et al. [100] or iterative inverse solutions such as one by Pulliainen and Hallikainen [160] simplify the snowpack to a one-layer model. Inaccuracies caused by this simplification can be minimized by a multi-layer emission model. Several studies have demonstrated the use of a multi-layer snowpack in SWE retrievals and have shown the significance of the multi-layer snowpack stratigraphy in comparison with one-layer snowpacks [49, 117, 168]. Durand et al. [51] have shown that the estimated root mean squared error (RMSE) of estimated SWE when neglecting layering is about 50% in different types of snow classes retrievals. To address this challenge, Durand and Liu [46] let the inversion algorithm choose the number of layers by iteration in a Bayesian Markov Chain Monte Carlo (MCMC) scheme. They proposed the inclusion of posterior probability iteratively using a Bayesian approach. The applicability of the method was then evaluated by Pan et al. [151] using *in situ* measurements and ground-based radiometry.

The main purpose of this research is to evaluate a Bayesian MCMC snow depth retrieval approach applied in a tundra snow context. The method employs snowpack properties and their probability distributions based on forward modeling simulations. What remains unknown is whether minimal snow and soil property priors taken from *in situ* measurements produce acceptable retrievals without any need for additional calibration of the physical emission model involved. This study, therefore, builds on the work by Durand and Liu [46] in the application of MCMC for snow depth retrieval from airborne T_b observations and ground-based snowpack measurements acquired in Eureka in 2011, an RT model, and site-specific parametrization of the RT model based on our previous work [178]. This research is unique as it incorporates previously applied methods using priors taken from a broad study with the application of same physical emission model and T_b observed by airborne radiometer [178].

In the following sections, an explanation of the methodology is provided including the MCMC theory followed by a detailed explanation of the experiments. Then, we discuss the results before making future suggestions for the application of this method.

6.2 Methodology

In this study, we use the forward emission model of Dense Media Radiative Transfer Multi Layer (DMRT-ML) by Picard et al. [155] to simulate the emission at an airborne footprint scale and then conduct retrievals using the MCMC approach to estimate snow depth. The MCMC method is chosen as it allows us to integrate probability distributions of snowpack properties based on the acquired knowledge of the study area. Snowpack profile characteristics and layering are determined using known distributions (or priors) of measured snowpack properties based on *in situ* measurements conducted at the study area. The acquisition of observations from airborne radiometry together with *in situ* measurements on the ground makes it possible to constrain the DMRT-ML for inversion and snow depth retrieval. The retrieval algorithm performance in this study is tested by two experiments explained in 6.3.3.

6.2.1 The inversion problem: the MCMC theory

The process of Bayesian data analysis begins with a probability model setup during which the conditional probability of the unknown parameters is constrained by the observations (brightness temperature in our study) [77]. Next is evaluating the posterior snow estimates to independent observations as a way to evaluate accuracy and precision. In this study, for probabilistic retrievals we use the MCMC method that is based on Bayesian statistical theory. Monte Carlo analysis allows adding randomness to a deterministic physical problem. Monte Carlo Markov chains of snowpack properties are created based on random draws of snowpack properties. Conditional probabilities of snowpack properties given specific T_b observations defines whether this random draw should be added to the Markov Chain. In this application it can be formulated as:

$$p(X|L_{obs}) \propto f\left(L_{obs}|X\right)\pi(X) \tag{6.1}$$

where $f(L_{obs}|X)$ is the likelihood of an observation, given a particular set of X state variables (unknowns) and $\pi(X)$ the corresponding prior distributions of the unknowns. MCMC searches for the snow and soil properties that result in the highest posterior probability of the observed $T_b, p(X|L_{obs})$. The posterior probability is calculated based on the difference between distributions of simulated and observed T_bs as well as the difference between distributions of retrieved snow properties and given priors. As mentioned previously, the current study is a continuation of the work by Durand and Liu [46], whose inversion approach used an MCMC algorithm and MEMLS with no surface model and minimal prior information to run an RT model. In our study, MCMC uses the Metropolis algorithm to generate random chains (state variables), and then attempts to maximize $f(L_{obs}|X)$ by considering prior distributions of state variables and likelihood functions in each run. The likelihood is calculated as in [46]:

$$\begin{aligned} & f\left(L_{obs}|X\right) = (2\pi)^{-\frac{n_c}{2}}\left|\Sigma_{L_{obs}}\right|^{-\frac{1}{2}} \\ & \exp\left[-\tfrac{1}{2}\left(L_{obs}-Y(X)\right)^T\Sigma_{L_{obs}}^T\left(L_{obs}-Y(X)\right)\right] \end{aligned} \tag{6.2}$$

where n_c is the dimensional identity matrix, ΣL_{obs} is the error covariance matrix for the observation and model, whose diagonal terms are $\sqrt{\sigma_o^2+\sigma_m^2}$ with σ_o being variance of the microwave measurements and σ_m being the model error and the remaining arguments representing the covariance between channels (assumed to be zero), Y(X) the T_b from the model, L_{obs} is the observed T_b. Diagonal elements of $\Sigma_(L_{obs})$ is set to 3 K and 2 K for 37 GHz and 19 GHz, respectively. Radiometer calibration accuracy (σ_o) that was reported as

~1 K for 37 GHz and ~2 K for 19 GHz, assessed by recording the brightness temperatures of targets with known temperatures (black body absorbers and sky observations) [212]. We assigned 1 K and 1.5 K for σ_o at 37 GHz and 19 GHz, respectively. A nominal value of 2.8 K and 1.3 K was assumed for σ_m; due to the inherent imprecision of measuring key model inputs, estimates of the true model uncertainty are not available. The prior distribution of variables, including layer thickness, grain size, density, and snow and ground temperature for a given number of layers, are generally calculated using gamma, or log-normal distribution. The prior distribution for all state variables, assuming conditional independency among them, is the product of all probabilities.

After changing the variables and computing the likelihood function in each run, the next step is to find the optimum values for state variables in the iterations. To move sequentially between iterations in a Markov Chain, the Metropolis algorithm is implemented as a random walk algorithm utilizing a so-called "jump distribution" [77]. Conceptually, we apply the Metropolis algorithm to estimate a vector of unknown snowpack and soil state variables. Transition between iterations in a Markov chain is governed by the likelihood function and the prior distribution of the snowpack state variables. A likelihood ratio, r, is defined by Gelman et al. [77]:

$$r = \frac{p\left(X_i|L_{obs}\right)}{p\left(X_{i-1}|L_{obs}\right)} = \frac{\pi\left(X_i\right) f\left(L_{obs}|X_i\right)}{\pi\left(X_{i-1}\right) f\left(L_{obs}|X_{i-1}\right)} \tag{6.3}$$

where $X_{(i-1)}$ is the vector of snowpack variables before the random walk/step, and X_i is the vector after the jump step. A flowchart of the process of optimal variable selection is presented in Figure 6.1. A jump step size is first set as a ratio of the variable's prior variance and then is adjusted based on a defined criterion. If the likelihood ratio is greater than a certain probabilistic value, r_c, then the probability that X_i would occur is higher, and X_i will be used in the i-th iteration. If not, $X_{(i-1)}$ does not change until the next iteration. Jump steps are adjusted in each 100 runs during the burn-in period and after this period, jump step size is adjusted every 1000 runs, this adjustment is made to maintain an acceptance rate (the rate of accepted variables in an iteration set), which is about 0.25-0.3 in this study. A burn-in period of 2000 iterations is where the chains start from the initial state variable values and gradually approach the posterior distribution. These burn-in iterations are still influenced by the initial values. Snowpack and soil variables are estimated from the Markov chain after the burn-in period, from the 2000th to the 8,000th iterations—where output variables are converged.

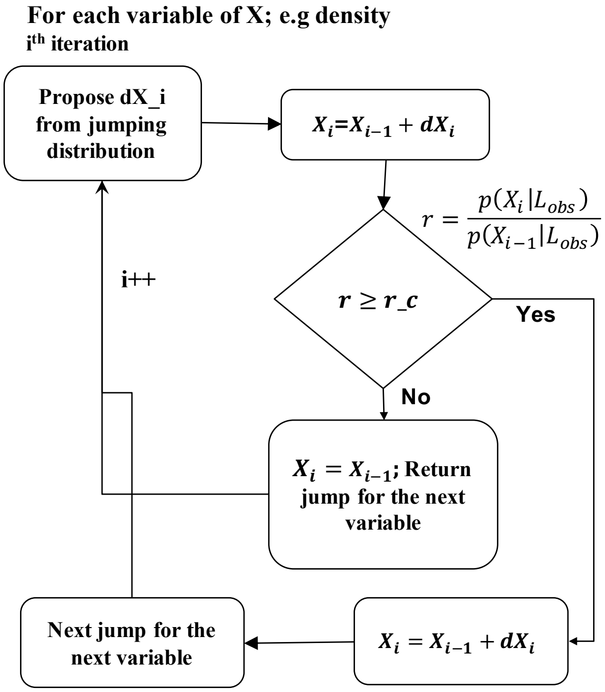

Figure 6.1: The flowchart of the variable (snowpack and soil) selection using MCMC sampler

6.2.2 Study area and datasets

Snow survey and airborne passive microwave brightness temperature measurements were made across the Fosheim Peninsula, near the Eureka weather station on Ellesmere Island (∼80°N; 84°W) between April 13th and 22nd, 2011. The region is cold and dry with an average annual air temperature at the Eureka weather station of -18.8 °C and total annual precipitation of 79 mm (1981-2010), with almost 60% falling as snow [56]. Airborne T_b observation data were acquired from dual-polarized 19, 37, and 89 GHz microwave radiometers mounted on the Alfred Wegener Institute Polar-5 research aircraft. The radiometers observed the ground aft-viewing at a 53° incidence angle, similar to the observing angles of the satellitebased Special Sensor Microwave Imager (SSM/I) and Advanced Microwave Scanning RadiometerEOS (AMSR-E) passive microwave sensors. The antennas at all bands have the same 6° half-power beamwidth.

The aircraft was based at the Eureka weather station and flew the study area where this study focuses from April 19th to the 23rd, 2011. Aircraft positional information was recorded using an Aircraft Integrated Meteorological Measuring System (20 Hz) system recording GPS data and platform attitude information which were used to precisely calculate the passive microwave radiometer footprint locations on the ground. All positional information was collected using the WGS 84 datum. In this research we use T_b observations from local-scale grid (33 km × 6 km coverage, collected during low altitude flight of ∼350 m above ground level [a.g.l]), flown on April 20th. Only T_b at 19 and 37 GHz were used for snow depth retrieval. In the previous study, model inputs could not be found that reproduce the observed T_bs at 89 GHz [178]. Thus, we omit them from this retrieval study. Figure 6.2 shows T_b observation footprint locations and corresponding *in situ* measurements in the study area. The airborne radiometer's IFOV dimension is dependent on the aircraft's ground speed, altitude, roll, pitch and yaw, as well as the radiometer beamwidth, view angle, and integration time. The radiometer variables remain constant during data acquisition: beamwidth = 6°; view angle = 53°; and integration time = 1s. A radiometer mounted on a stationary platform with the same low altitude flight height would create a ground-projected IFOV of 100 m by 60 m. However, because the aircraft is moving, a 1-s integration time would elongate the IFOV and produce a "smeared footprint" [38]. Dimensions of a (smeared) footprint at low altitude were calculated as 120 m × 102 m (along-track across-track). More technical information about the study area and preprocessing of the T_b footprints can be found in Saberi et al. [178].

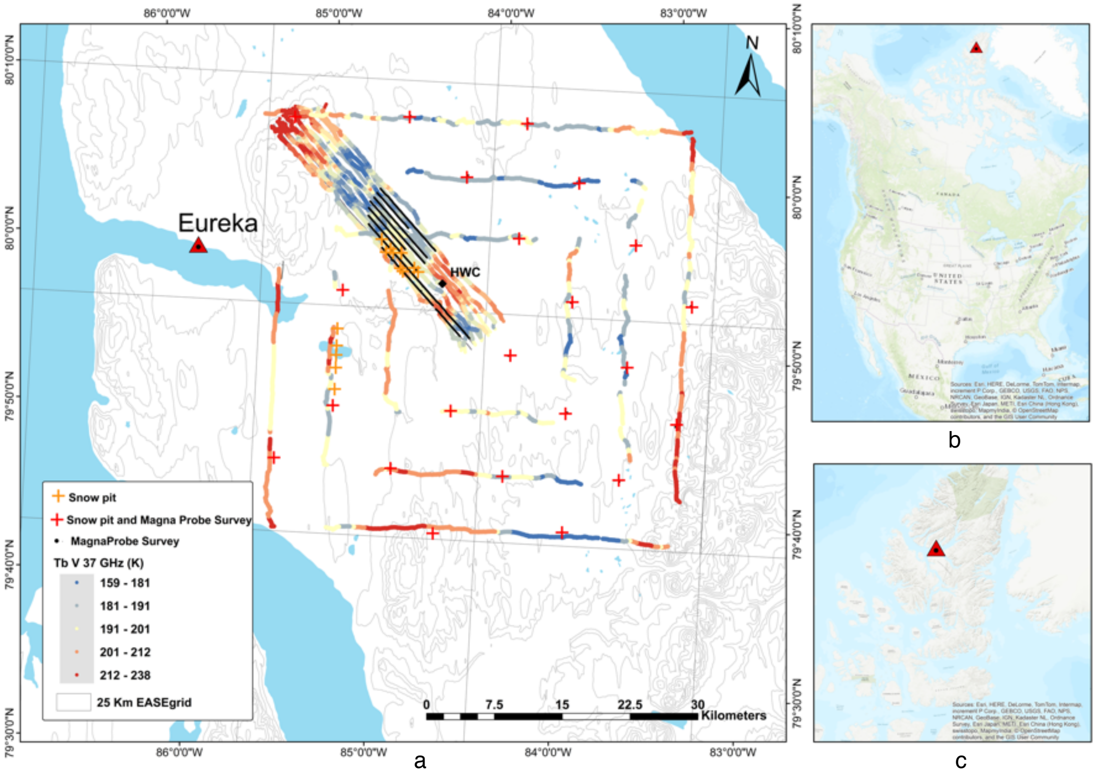

Figure 6.2: Snow survey locations, snowpits and MagnaProbe transects, and EASE-Grid pixel boundaries [178].

6.2.3 The approach to applying MCMC theory to the Eureka experiment data

Implementation of the MCMC theory within a Bayesian inversion framework is developed to retrieve snow depth using airborne passive microwave observations and the DMRT-ML model. The MCMC code, developed in MATLAB, calls the simulation runs of DMRT-ML using a wrapper that runs the code in its original written language, Fortran 90. Since the domain of MCMC application is tundra snow, which typically consists of a two- or three-layer snowpack, we use a two-layer snowpack DMRT-ML representation that consists of a depth hoar and wind slab layer as developed in Saberi et al. [178]. The model approach is parameterized with a two-layer snowpack with explicit definition of depth hoar and wind slab in each layer initialized based on field data collected during the 2011 Eureka field study. The probability density functions of snow depth, grain size, density, and physical temperature in a two-layer snowpack obtained from snow pits in the Eureka region are used to setup the MCMC priors. Brightness temperatures at 19 and 37 GHz, vertical polarization are used as the observations to conduct snow depth retrieval in the MCMC algorithm. Sensitivity of T_b at horizontal polarization is similar to the vertical polarization, and thus is also not included in the observations used for the snow depth retrieval. In the following sections, the preparation of MCMC priors and the retrieval experiment design is elaborated.

6.3 Experimental implementation of the MCMC

The MCMC algorithm for SWE inversion searches for the best match between simulated T_bs using DMRT-ML model estimates and airborne-observed T_bs. MCMC searches for snowpack variables with emissions close to observations based on the priors. In this section, for a complete understanding, the MCMC algorithm setup for priors is explained. Local priors of snowpack variables are presented first, and then the experiment design of the inversion is explained in two steps of applying MCMC on footprint data, and applying MCMC in a generalized approach.

6.3.1 Priors of snowpacks' variables

The data used to calculate the priors of the snow variables for the inversion is from 12,594 Magna Probe (GPS-tagged) snow depth measurements in the region with a range of 5-90 cm, an average of 26.9 cm and a standard deviation of 23.9 cm, along with physical temperature and density values measured in 49 snow pits. Priors are estimated using all *in situ* measurements in the study area, whereas averaged MagnaProbe data in each footprint is used for the evaluation of the snow depth retrieval accuracy in each footprint (explained in 4.1).

First, because we have only T_bs at 19 and 37 in vertical polarizations with high sensitivity to soil and snowpack properties, and also because we aim to do the inversion with minimal data inputs and prior information, it is very important to characterize the snowpack layering. Based on the snowpit measurements, snowpack characterization is generalized using an unsupervised K-means clustering of average grain size and snow density for variety of snow layer type classes including: recent, fine-grained, medium-grained, crust, soft slab, medium slab, hard slab, slab-to-hoar, chains of hoar (indurated), chains of hoar, depth hoar and icy hoar. Two major layers of wind slab and depth hoar were generalized from merging four K-Means' clusters. These two layers with small scatterers on top and medium-sized grains in the bottom can replicate the slope reversal of T_b observations with the snowpack increase [178]. Therefore, the retrieval was conducted with a two-layer snowpack configuration, which is composed of a wind slab layer over a depth hoar layer.

Average snow density and snow temperature were calculated from all the wind slab layers classified based on K-means clustering of nine snow layers from the snowpit measurements, and used as the corresponding priors for the wind slab layer; the same was done for the snow density and temperature priors for the depth hoar layer. The average and the standard deviation of the thickness of wind slab and depth hoar layers can also be calculated from the snowpit measurements. However, the absolute values of the thickness cannot be used directly, because they are too accurate. Therefore, using *in situ* measurements coupled to forward modelling tests, we derived another conditional constraint for the snow layer thickness, based on a relative thickness ratio of the wind slab and the depth hoar layers. This constraint is based on the observed inflection point for T_b as discussed earlier and demonstrated in Saberi et al. [178]. The forward modeling obtained a reasonable fit using a 1:2 depth hoar to wind slab ratio for shallow snow (hereafter we call it as a depth hoar formation phase) and a developing wind slab using a fixed 7 cm depth hoar for deep snow (hereafter we call it as the wind slab development phase).

For the grain size, DMRT-ML requires the optical diameter (D_{opt}) of grain size as an input. However, geometrical maximum (D_{max}) and minimum (D_{min}) dimensions of grains were measured in the field and there is currently no established methodology widely accepted to adjust D_{max} or D_{min} to values of D_{opt} [176]. On the other hand, uncertainties in the measurement and the representation of grain size and the conversion from D_{max} to D_{opt} are likely to mix when upscaling to the airborne footprint observations. Therefore, in this research, effective grain size (D_{eff}) that is a scaled value of D_{opt} adapted for snowpack microwave emission models, is used. The grain size priors for wind slab and depth hoar layers are adapted based on experiments reported by Roy et al. [171]. This information is used to provide first candidates for the grain size priors. Based on forward modeling and comparisons with observed airborne T_bs, we evaluated these grain size priors. We found that within the defined range of grain size prior and a stickiness factor of 0.2, proposed by Matzler [136], combined with the snow layering, T_b at 37 GHz vertical polarization can be simulated to replicate a decease with the increasing snow depth up to 21 cm and an increase as the snowpack thickens beyond 21 cm. The inclusion of a stickiness factor has been proposed in other studies to represent snowpack microstructure in microwave modelling [215, 128]. It is recognized that stickiness is an unmeasurable parameter and therefore, in order to avoid spurious explanation, we considered this parameter as a model constant.

6.3.2 Setting the priors for MCMC

Table 6.1 presents ranges of priors used in MCMC algorithm. We used gamma distributions as it fit the best for physical temperature, snow depth, and density. Grain size priors are adapted from previous studies based on observed stratigraphy and generalization technique that has been applied [171, 178]. We constrain the microstructure of the snowpack, and then MCMC computes probabilities of the posteriors. The optimum microstructure is defined based on forward modeling and comparisons with observed airborne T_bs, which indicate that DMRT-ML can be used to simulate the T_b V 37 GHz decrease with increasing snow depth up to 21 cm, whilst a two-layer slab and depth hoar with fixed depth hoar thickness (6.5-7.5 cm) and increasing wind slab thickness can successfully simulate T_b increases as the snowpack thickens beyond 21 cm which occurs more commonly later in the season.

We use the soil layer reflectivity model of Wegmuller and Matzler [226] for a rough surface, using a prescribed dielectric constant. Assuming a frozen substratum—according to the average soil temperature in the study area—with a permittivity between 4+0i and 6+0.5i, a root mean square (RMS) of roughness in a 0.001-0.1 m range was found to be acceptable. Soil temperature is the only soil variable that Durand and Liu [46] considered in the MCMC inversion algorithm. They set it to be the same as the prior used for the temperature of the bottom-most snow layer. Pan et al. [151] added soil moisture and roughness in the parameterization of emission modeling, using priors fixed at 8±8% and 1±1 cm for soil moisture and roughness, respectively.

Table 6.1: Snowpack and soil input priors parameters from snow pits measurements for emission

2-layered snowpack and soil model	**Snowpack variables**	**Ranges**
Wind slab layer	Thickness	2/3 of total snow depth for snow depth < 21 cm; and 15.5-82.5 cm for snow depth ≥ 21 cm
	Density	300-440 kg/m^3
	Grain size	300- 500 μm
	Temperature	242-248 K
Depth hoar layer	Thickness	1/3 of total snow depth for snow depth < 21 cm; and fixed to 5.5-7.5 cm for snow depth ≥ 21 cm
	Density	150-300 kg/m^3
	Grain size	900 - 1300 μm
	Temperature	242-248 K
Substratum: Soil model	Dielectric properties-Permittivity	4-6
	Dielectric properties-Loss	0-0.5
	Sigma	0.001-0.1 m
	Temperature	240-247 K

6.3.3 The application of MCMC

Because the T_b footprint is large, one T_b measurement can be related to a number of MagnaProbe snow depth measurements on the ground. To evaluate the way multiple magna probe snow depth measurements can represent T_b inside one footprint, an analysis was conducted: 1) simulating T_bs for each MagnaProbe snow depth within a footprint and then averaging the simulated T_bs, 2) averaging all snow depths within a footprint and then simulating the emission for an averaged snow depth. This comparison of multiple instances (footprints with snow depth standard deviations of 30-50 cm) shows a maximum T_b difference of 0.1% between these two cases, at T_b 19 and 37 GHz in both polarizations. Thus, T_b values are not significantly different whether we run the emission model on an averaged snow depth (as a representative of a footprint snow depth), or we run it for each snow depth and then average the simulated T_bs. So, we choose the second option of averaging snow depths within each footprint, as this process is less computationally intensive.

Although a 2-layered snowpack that develops depth hoar and eventually forms wind slab can depict the trend of observations, discrepancies between observations and simulations may still be found. Error can arise from emission model errors, and from uncertainty in T_b measurements (e.g., antenna gain consistency and geo-registration accuracy) and the representative of the MagnaProbe depths to the footprint T_b that is the mean value of measured depths. The sensor measurements are averaged over time, space, and spectral bandwidth. This averaging is done by convolving the inputs using a response function. The upwelling emission from a surface is the portion of the total emissions coming from a ground instantaneous field of view (footprint). While the measured natural emission is transformed radiometrically through the instrument system [187], we simulate the emission of a snowpack without considering any of these transformations, assuming that the frequency-dependent uncertainties are contained within the specified measurement error budgets. Unlike the analysis from the last paragraph, the uncertainty here is not from the averaging process, but is from the sampling protocol as well as available methods for generalizing collected data, i.e., the way to represent a large-area footprint by 1 or 2 transects of depth measurements.

To test how these uncertainties may influence the retrieval, we designed two sets of retrieval experiments. In the first, a footprint-based experiment, T_b values from footprints were used for retrieval and retrieved snow depths compared with the measured snow depth (average values from the MagnaProbe were used) inside a footprint. The other experiment is a synthetic approach that is based on the averaged T_bs for the same snow depth (± 2.5 cm range) from all footprints. This approach is acceptable because the retrieval was conducted using airborne experiments for a small area within four days of constant weather. In addition, the main controlling influence on the snow depth and distribution of snow in this region is local-scale topography, as existing vegetation is extremely sparse (bare ground), or very low-lying [178]. In our study area (one AMSR-E grid), we assume that the microstructure and the layering of snowpacks have properties in common. Therefore, the way that T_b is sensitive to the snow properties is similar, and the T_b for the same snow depth can be aggregated to reduce the uncertainty. The two experiments' details are as follows.

MCMC's application on filtered data

In the first experimental approach, the MCMC was run on filtered T_bs applying the realization of depth hoar development in snow depths up to 21 cm and then the slab formation for deeper snow greater than 21 cm as discussed in our previous study [178]. Figure 6.3 and Figure 6.4 show T_b V 37 GHz and T_b V 19 GHz footprints as a function of measured snow depth. In each T_b-snow depth group within the range of 9 cm, quantiles of T_bs with cumulative probabilities of 0.25 and 0.75 (QL and QU) are calculated and T_bs with values greater than QU+1.5×(QU-QL) or less than QL-1.5×(QU-QL) are assumed to be outliers. Filled triangles represent the interquartile range (IQR) of the T_bs and the crosses are the

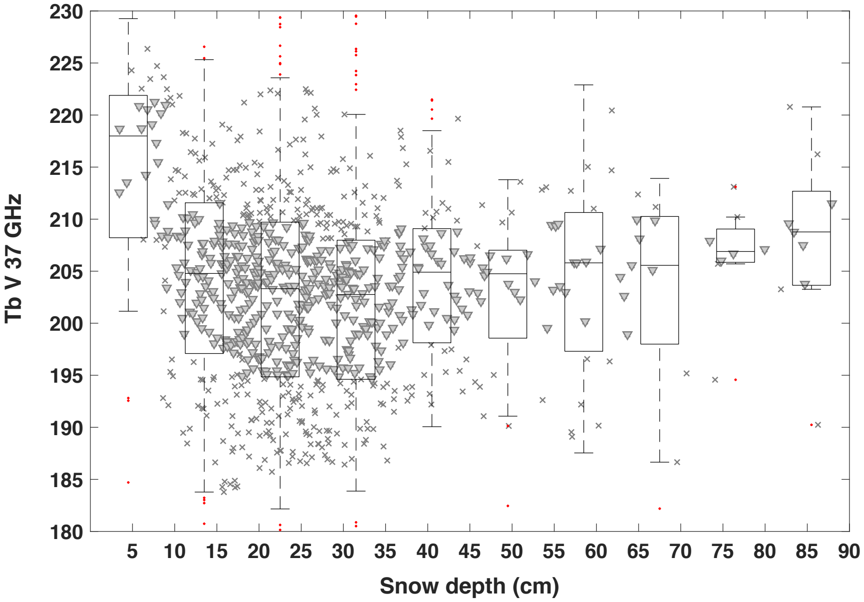

Figure 6.3: T_b V 37 GHz observations as a function of measured snow depth for the IQR (shown as triangles) and 95% coverage of T_b distribution (shown as crosses) within each 9 cm snow depth range bin. The boxplots shown are for the 9 cm snow depth ranges.

remaining 95 percent of T_bs outside the IQR, but within the $\pm 2\sigma$ of the data from the mean in each 9 cm snow depth class. We used IQR Tbs as filtered

MCMC's application in a synthetic approach

In the second experimental approach, median T_bs representing emissions for snow depths values from 5 to 90 cm with a 5 cm interval were used. The reason we called this analysis a synthetic approach is that we used T_b values that are not actually observed but they are representatives of the observations in each 5 cm interval. Decrease and rise trends of selected T_bs were predictable by the inversion of simulations and assumed to be minimally affected by random errors caused by measurements and uncertainties inherited by the high variability of snow depth in an airborne scale footprint.

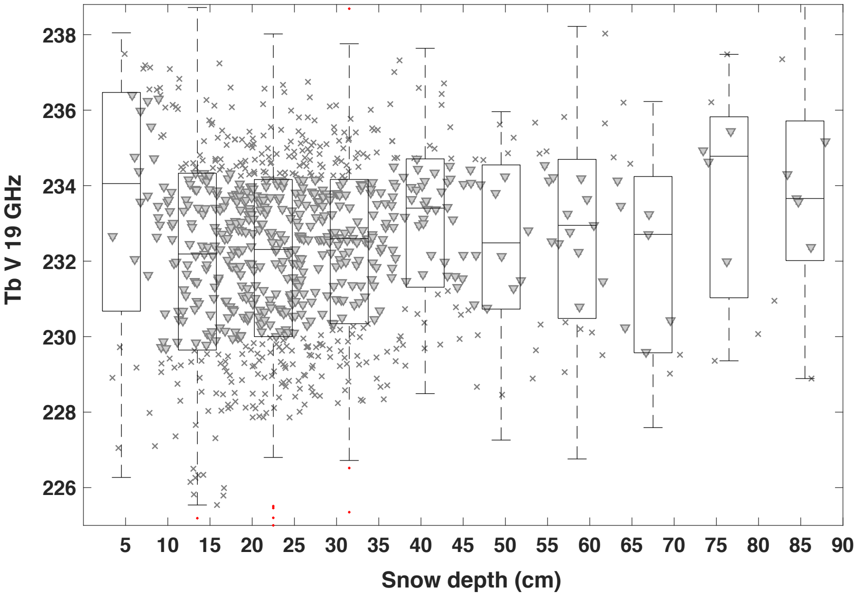

Figure 6.4: T_b V 19 GHz observations as a function of measured snow depth for the IQR (shown as triangles) and 95% coverage of T_b distribution (shown as crosses) within each 9 cm snow depth range bin. The boxplots shown are for the 9 cm snow depth ranges.

6.4 Results

MCMCs application on filtered data

The inversion algorithm is applied on 464 T_b footprints within the IQR of 5 cm snow depth intervals. T_b footprints outside of this interquartile range are not used in the inversion analysis, so as to increase consistency and focus more on less erroneous data. A significant although weak Pearson correlation of 0.27 was observed between the estimated and measured snow depths in the 6-21 cm depth range which represents the initial depth hoar dominating layer. A weak, but significant, Pearson correlation of 0.21 between estimated and measured snow depths of 22-90 cm characterized the wind slab layer development phase, where wind slab layer dominates the snowpack. The scatterplots for the depth hoar development and wind slab development phases are shown in Figure 6.5-a and Figure 6.5-b, respectively. The RMSEs for the whole 6-90 cm range of estimated snow depth is 21.8 cm (for 5-21 cm and for 22-90 cm), while the RMSEs of T_b V in 37 and 19 GHz are 3.5 K and 1.3 K, respectively. The RMSEs are 13.7 cm for the 6-21 cm snow depth range and 58 cm for the 22-90 cm snow depth range. Mean bias of snow depth (estimated-measured) is 13.5 cm for the 5-21 cm range and 55.6 cm for 22-90 cm range, respectively. Mean value of MCMC retrievals uncertainties for 75% of the retrievals in 6-21 cm range is 25.8 cm while this uncertainty is as large as 151 cm for 21-90 cm range of snow depths. Noteworthy, snow depth measurements STD is 1.5-57.7 cm in the whole region. Considering T_b observations plotted in Figure 6.3 and Figure 6.4, given the spread of data, there are many footprint instances where a range of T_bs is observed for a single snow depth or a single T_b value is observed for a range of depths. Therefore, we would expect less accurate estimates of snow depths. In both scatterplots of Figure 6.5, we can see that there is less agreement in the 15 to 30 cm range. Additionally, in the wind slab development case (Figure 6.5-b), lower correlation between estimated and measured snow depths is as a result of less sensitivity of T_b 37 V as a function of snow depth. In short, the sensitivity of T_bs at 37 V in snow depths over the 22 cm to 90 cm range (wind slab dominated) is only 5.8 K, compared with the 15 K decrease of T_bs in snow depths ranging 6 cm to 21 (depth hoar dominated). This means that with a higher sensitivity of T_bs to snow depth (depth hoar dominated snowpacks), the probability of inversion accuracy will likely increase. To better understand the inversion process and uncertainties, the estimated chains of two footprints, #1 and #2, with and average snow depth of 13 cm and 56 cm respectively are examined. Markov chains of T_bs and histograms of snowpack's properties in these footprints are plotted in Figure 6.6 and Figure 6.7. Snowpit EK16 and snowpit 021 are located within footprints #1 and #2, and represent the stratigraphy of shallow and deeper snow in the footprints, respectively. No numerical comparisons are made between snowpit measurements and estimated variables

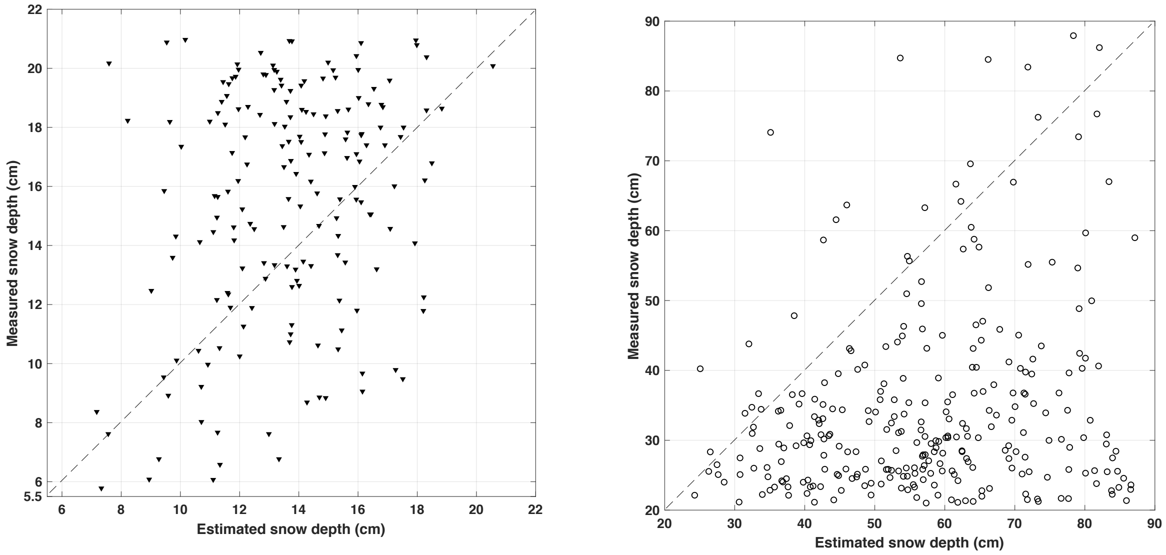

(a)

(b)

Figure 6.5: Scatterplots of measured vs. estimated snow depth in all IQR footprints for cases of (a) depth hoar formation and (b) wind slab development.

within a footprint using MCMC inversion, as evaluations based on point-scale measurements for footprint scales are not verifiable. Therefore, measured variables in each snow pit are not shown in the chains histograms of Figure 6 and Figure 7, as the snow pit measurements do not represent the estimates in a footprint scale.

Footprint #1 represents a shallow snowpack with microwave emission simulated via a 2:1 wind slab to depth hoar ratio. Markov chains of T_bs and observed T_bs are shown in the Figure 6.6-a. Estimated T_bs are quite close to the observations with a 0.9 K and 0.2 K absolute difference between observed and estimated T_bs at 37 V GHz and 19 V GHz, respectively. The snowpit EK16 within this footprint is a five-layer snowpack consisting of recent snow, hard slab, moderate slab, slab-to-hoar, and chains of hoar. Disregarding the recent layer as it constitutes only 2% of the whole snowpack, we have two merged layers of a 9 cm wind slab and a 4 cm depth hoar. The mean and STD of 12 snow depth MagnaProbe measurements in the inclusive footprint is 13.2 cm and 16 cm, respectively. Figure 6.6-b shows histograms of Markov chains for each layer thickness to simply display the posterior probability of this variable. The modal value after burn-in period is 8.7 cm with a STD of 2.5 cm for the wind slab layer and 2.5 cm with a STD of 0.6 cm for the depth hoar layer. The average densities at the field in snow pit EK16, are 370 kg/m^3 for the wind slab layers and 230 kg/m^3 for the depth hoar layers. Figure 6-c shows histograms of Markov chains for each layer's density. The modal values after burn-in period are 335 kg/m^3 and 259 kg/m^3, for the wind slab and depth hoar layers, respectively.

Snow grain metrics observed by snow surveyors in the field are geometrical maximum (D_{max}) and minimum (D_{min}) dimensions. Unfortunately, these metrics cannot be directly input into the DMRT-ML model, which represents the snow grains as spheres with an optical diameter, D_{opt}. Therefore, assumed priors of grain sizes in our analysis are based on previous modeling studies to represent grain size parameterizations [171]. Figure 6-d shows histograms of Markov chains for each layer grain size. The modal value after burn-in period are 650 μm and 1080 μm for the wind slab and the depth hoar layers, respectively. The snow layer temperature at the site were measured as 244.3 K in the depth hoar layer and 245.5 K in the wind slab layer. The substratum layer's temperature was measured as 244.8 K. Figure 6-e shows histograms of Markov chains for each layer's temperature. Estimated physical temperatures for wind slab, depth hoar, and sub-stratum layers are 246.2 K, 245.2 K, and 243.6 K, respectively. Higher variance in estimations is as a result of large variances applied to the temperature priors which itself inferred from the statistical analysis of the measurements in the study area. Footprint #2 represents a deeper snowpack situation with wind slab developed over a constant depth hoar layer that is simulated via a progressive wind slab thickening to a fixed depth hoar layer. Markov chains of T_bs and observed T_bs are shown in the Figure 6.7-a. Estimated T_bs are quite close to the observations with a 0.8 K and 0.1 K difference between observed and estimated T_bs at 37 V GHz and 19 V GHz, respectively. Site 021 is a snowpit with 56 cm containing four layers of snow each characterized as recent snow, hard slab, moderate slab, and depth hoar. The topmost layer is less than 0.5 cm, and slab layers constitute 85% of the total thickness equal to 48.5 cm. The depth hoar is 7.5 cm. A small variance for the thickness of the depth hoar layer is applied through *a priori* information which was confirmed in the forward modeling step as well. The average value of 13 MagnaProbe measurements in the inclusive footprint is 51.6 cm along with a large STD of 45.4 cm. Figure 6.7-b shows histograms of Markov chains for each layer thickness. The modal value after burn-in period is 43.5 cm with a STD of 9.1 cm for the wind slab layer and 7 cm with a STD of 0.2 cm for the depth hoar layer. Average densities of the wind slab and depth hoar layers measured at the snow pit are 410 kg/m^3 and 260 kg/m^3, respectively. In Figure 6.7-c, there is a skew to higher densities in both layers, which when it coincides with smaller grains in wind slab, simulates the snowpack's self-emission. The modal value of densities after burn-in period is 418 kg/m^3 and 285 kg/m^3 for wind slab and depth hoar, respectively.

Figure 6.7-d shows histograms of Markov chains for each layer grain size that estimated grain sizes of 570 μm and 1110 μm for wind slab and depth hoar, respectively. The snow

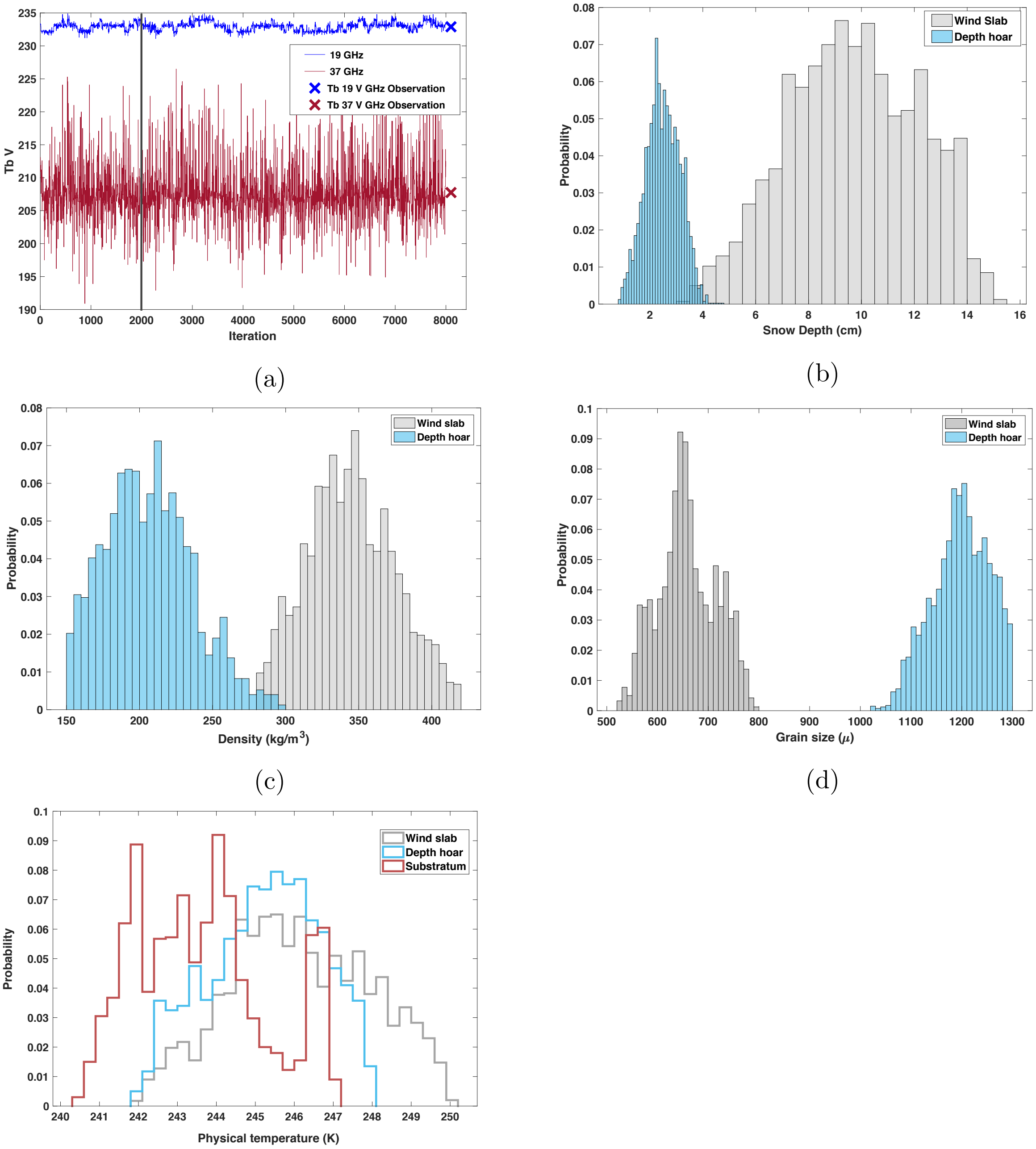

(a)

(b)

(c)

(d)

(e)

Figure 6.6: MCMC results for footprint #1. Observed T_bs and Markov chains of estimated T_bs at 19V and 37V GHz are shown in (a). Markov chains histograms of wind slab and depth hoar layers, density, grain size and physical temperature are shown in (b), (c), (d) and (e), respectively. Markov chains histograms are for the two snow layers (wind slab and depth hoar) for all four parameters except for the physical temperature which also includes the substratum histogram.

layers' temperatures at the site were measured as 244.3 K in the depth hoar layer and 245.4 K in the wind slab. The substratum layers temperature was measured as 245.7 K. Figure 6.7-e shows histograms of Markov chains for each layer temperature with estimations of 246.1 K, 245.2 K, and 244.9 K for wind slab, depth hoar, and sub-stratum layers, respectively. Observed difference among measured and estimated temperature gradients can be explained by local controllers of the temperature.

Calculated MCMC chains contain 8,000 array arguments, where the modal value of chains after the burn-in period is considered to be the converged value. The burn-in period is defined by a solid black line in Figure 6.7-a. The reason to choose a modal value rather than an averaged value is the exclusion of extreme values. The jump size for a snowpack variables selection significantly impacts the convergence rate in MCMC chains. The soil properties posteriors are not shown as they construct a uniform range with little variation, due to the small range of dielectric properties of frozen soil [86]. Moreover, our limited information about soil properties such as roughness in the region confine these properties by the pre-processing step explained previously.

We applied the MCMC algorithm on 464 footprints, whereas only two out of 38 footprints having inclusive snow pits were chosen to explain the results in detail. These two sites were chosen because the measured snow pit depths were very close to the average MagnaProbe measurements within the whole footprint (less than 10% difference).

One noteworthy element in employing MCMC in all 464 footprints and using averaged MagnaProbe data to compare estimated snow depths was that we found several instances with extreme underestimations and overestimation of snow depths (more than 100% of snow depth) mainly caused by uncertainties linked to airborne T_b observations (Figure 6.3 and Figure 6.4) and possible shortcomings of the model implementation. This is because the MCMC retrieval here assumes a fully snow-covered land with uniform depth inside the footprint. No effects of fine-scale topographical variation and the variations of distributed snow depth and snow microstructure within footprints were considered, which would also challenge the representation of the MagnaProbe measured snow depth. On the other hand, due to the low sensitivity of brightness temperature to snow depth, even at 37 GHz, the MCMC algorithm has to constrain the retrieval to meet the observed T_b tightly, in order to make use of this sensitivity. However, in this case, errors in the T_b measurements will transfer into errors in the estimated snow depth, and possibly result in extreme underestimations or overestimations. Because the T_b and the snow depth are noisier at footprint scales, the MCMC inversion with current available ground-based measurements at footprint scales is of limited accuracy, especially for deep snowpacks where the wind slab is dominating the snowpack. Therefore, we employed another approach to minimize uncertainties in a synthetic approach, explained in the following section.

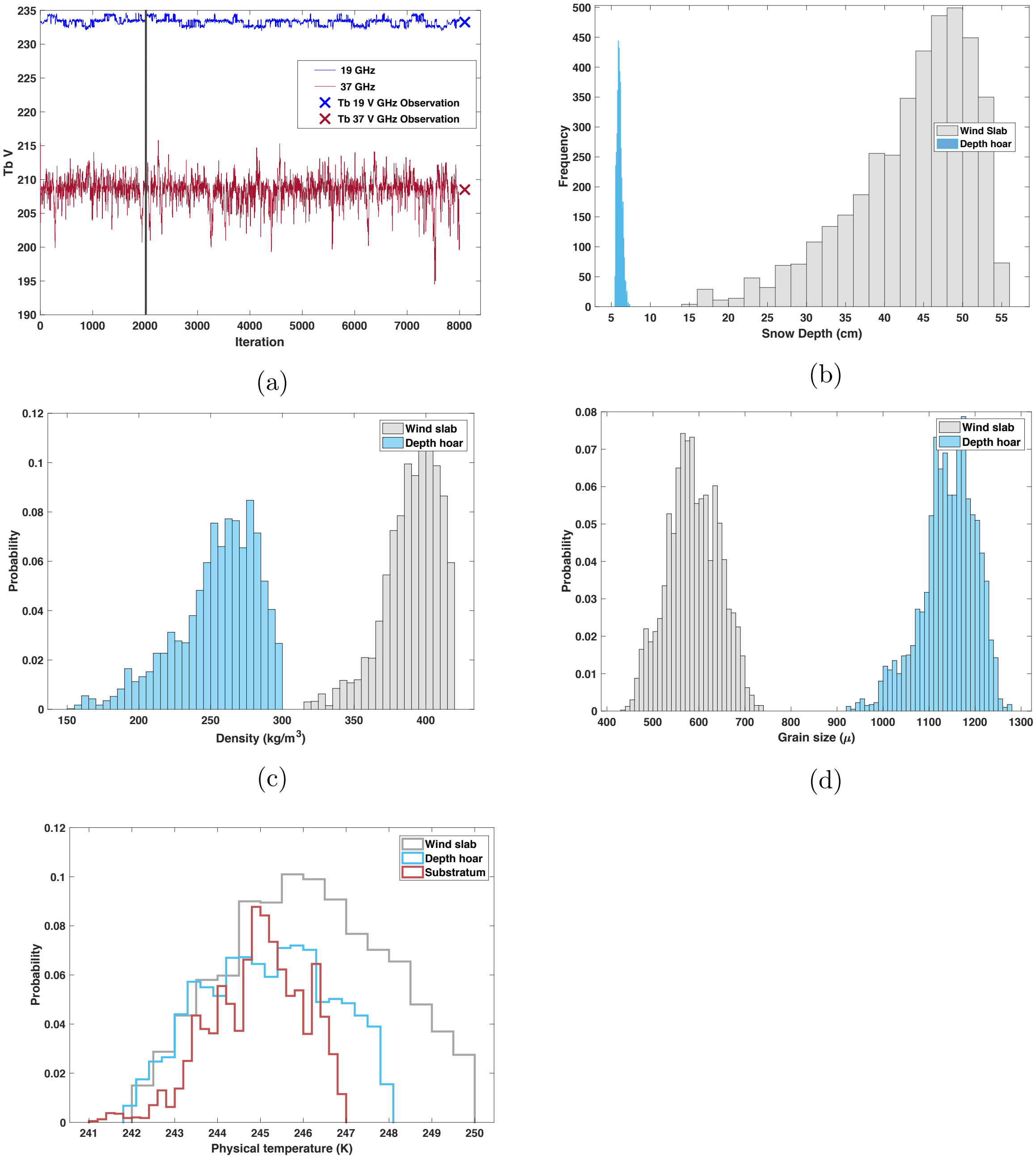

(a) (b) (c) (d) (e)

Figure 6.7: MCMC results for footprint #2. See Figure 6.6 caption for explanation.

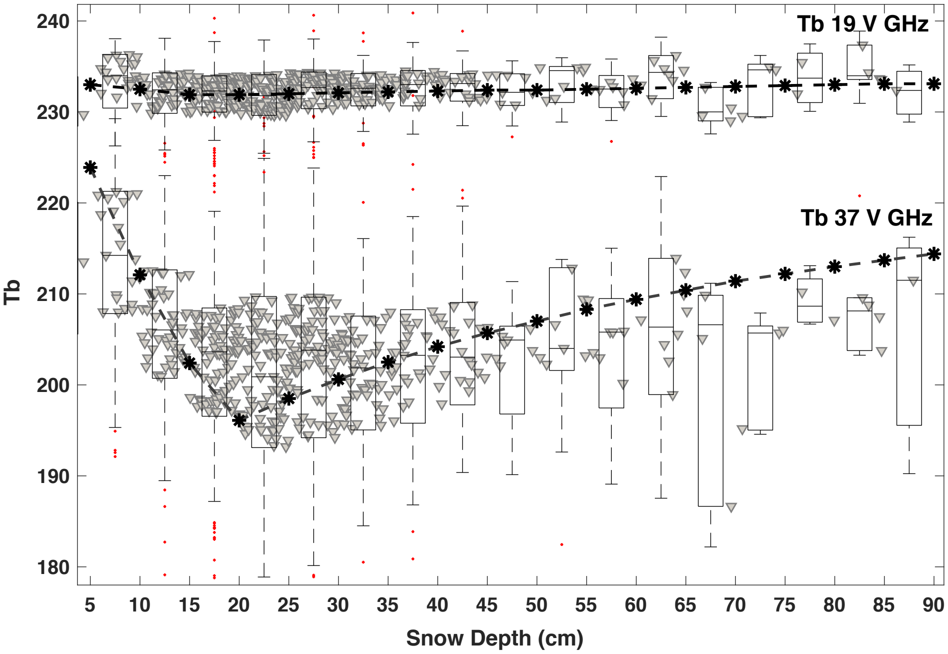

Figure 6.8: T_b V 37 GHz and 19 GHz observations as a function of measured snow depth for the IQR (shown as triangles) within each 5 cm snow depth range bin. Asterisks show simulated T_bs using the mean values of priors.

MCMC's application in a synthetic approach

Given the high degree of variability of snow depth within and at the individual footprint scale as well as the high degree of emission variability, the MCMC was applied in a synthetic approach. By replicating general emission behaviour of snowpacks, the forward emission model was run using mean values of priors for snow depth intervals of 5 cm ranging 5-90 cm. This simulated T_bs correlated to aggregated T_bs—with a linear correlation coefficient=0.9—shown as asterisks in Figure 6.8. This analysis shows how the retrieval works under perfect conditions (zero noise level in observations, perfect emission model and no spatial variability of SWE at footprint scales).

The estimated and measured snow depth scatterplot and the scatterplot of estimated and measured T_b V 37 GHz and T_b V 19 GHz are presented in Figure 6.9 and Figure 6.10, respectively. A significant and high Pearson correlation of 0.94 was observed among estimated and measured snow depth, which the scatterplot is presented in Figure 6.8. RMSE of snow estimated depth is 0.07 cm and RMSE of T_b V in 37 and 19 GHz are

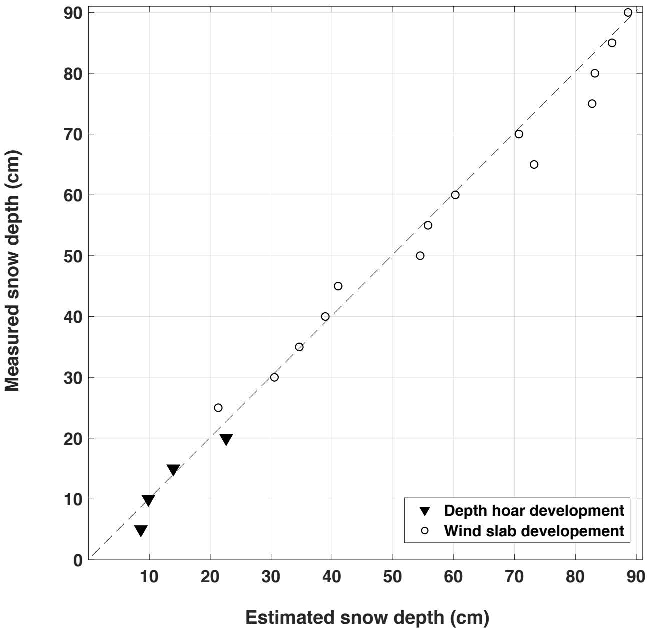

Figure 6.9: Estimated and measured snow depth scatterplot in sampled footprints based on synthetic approach

2.7 K and 0.14 K, respectively. Although higher accuracies were obtained, this experiment cannot be employed to retrieve snow depths in this study area as it took all observations and measurements in the region to represent a typical emission signature. This analysis helps to present a case where observations are ideally predictable using an emission model, whereas in an experiment with high spatial variability of SWE and high emission variabilities, we should expect high retrieval uncertainties.

6.5 Discussion

The results show how a Bayesian inversion, specifically in a retrieval problem with high uncertain variables, can be applied but with some care. The approaches taken for the application of MCMC that was conducted in the two steps of 4.1 and 4.2, underline the importance of methods that deal with uncertainties related to T_b observations. The T_b observations in our study area have a high standard deviation (STD) in shallow to medium depth snowpack, for instance in footprints with average snow depth values of 18-27 cm

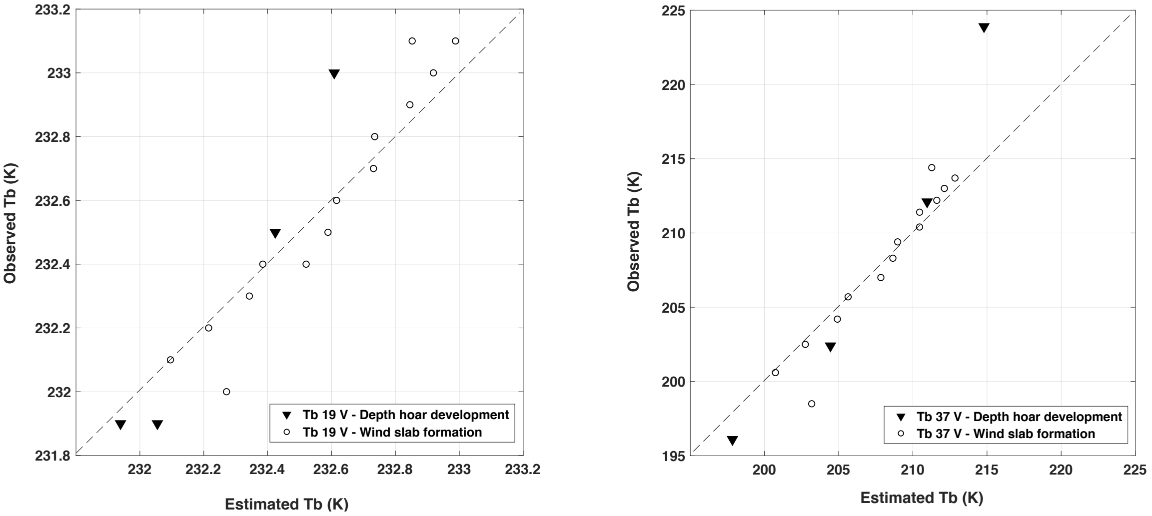

(a) (b)

Figure 6.10: Estimated and measured T_b V scatterplot at 19 GHz (a) and 37 GHz (b) in sampled footprints based on synthetic approach

range, the STD of T_b 37 GHz is 11.1 and the STD of T_b 19 V GHz is 2.8. This variability confirms the high level of uncertainties and expected snow properties retrieval error. On the other hand, based on KolmogrovSmirnov statistical testing in our previous work, T_b observations at 19 V GHz and 37 V GHz have different distribution functions compared to simulated T_bs at the same frequencies [178]. One solution to control these uncertainties is adding extra information to each T_b footprint, such as remotely sensed observations or intensive ground-based measurements. Intensive ground-based measurements at the airborne scales are not feasible in many small-scale projects. Moreover, quantifying propagation of associated errors with all data sources that are included the retrieval process, will not be a straightforward process if errors from different sources are correlated [71]. Another solution to deal with T_b uncertainties is to minimize the errors at the expense of losing footprint scale T_bs. Taking this approach, we evaluated MCMC retrievals through a synthetic approach using forward emission modeling that correlates well with averaged T_bs of binned snow depths, where T_b footprints are mapped as a function of snow depths. The success of synthetic approach is a hint for consideration of these limitations in the design of field observations framework as well as details of tools and variables to measure.

In the absence of intensive ground-based snow stratigraphy measurements and unaccounted for physical processes, priors play a significant role in calibration of the forward model. Furthermore, in the inversion process, priors confine the search space of unknowns effectively and therefore should reduce uncertainties in retrieval. In this research, priors are defined based on local measurements and they are adapted by forward emission modeling. This process minimizes the impact of unaccounted variables in the emission process. The novelty of this research is in the labeling the data using a simple snow depth criterion to determine whether the inversion is related to a snowpack that is scattering dominant (depth hoar) or it is the one that is a self-emitting medium (wind slab). Furthermore, using this method, statistical distributions of snow layer physical temperature, density, and depth were all unimodal. Unimodality is an advantage of forcing the prior information about a snowpacks stratigraphy based on forward modellings using *in situ* measurements. By using a Bayesian framework, the inversion process allows statistical distribution information in the form of priors to be included. Although a challenging approach, this method is preferable to the commonly-taken approach of point (*in situ* data) to area (footprint remote sensing observation) calibration and validation. Applying a deterministic inversion approach is generally achieved through a minimization of differences between simulated and observed T_bs through the varying of one or two key parameters such as snow depth or grain size to seek for an optimum snow depth value. The beauty of adopting an MCMC framework approach, is that the uncertainty in both T_b and *in situ* snow depth measurements can be represented through the priors and that the final converged solution typically represents the uncertainty in the data. In essence, this framework solution is one realization of a distribution of solutions but is perhaps more defensible given the statistical uncertainty in the *in situ* and T_b measurement data.

6.6 Future suggestions

The spatial variability of the *a priori* data make retrieval of SWE at spaceborne PM scales challenging. When the high variability of individual footprint T_b observations are coupled with a detailed physical model forced with *a priori* data that reflect the highly variable nature of snow properties, disagreements between modeled and observed T_bs are almost inevitable. This study illustrates such a situation. Model calibration in its traditional form, known as fitting the model outputs to observations by adjusting the model parameters, is not reliable as it forces the model to match observations by tuning model parameters. The Bayesian model calibration approach proposed by Kennedy and O'Hagan [102] represents a potential solution to the problem.

Sacks et al. [179] discuss the deterministic nature of most physical models that result in identical outputs for the same inputs after running the model. Being deterministic differentiates models from physical experiments, which tend to be plagued by random errors-both human and instrument. Sacks et al. [179] assume that a model is a realization of a stochastic process carried out through adding random functions. This assumption allows us to analyze the predictor in a statistical framework and quantify the associated uncertainty of the model. We can modify the model response using a Gaussian process with a covariance term involving snow depths. Snow depth should be chosen as it drives the emission response. The DMRT-ML is also very sensitive to the grain size and in the same time it contains highest uncertainty compared to other variables. Future studies should add a discrepancy term to capture the uncertainty in the hope to reduce the sensitivity that is not observable at airborne scale.

6.7 Conclusion

This current work is a retrieval approach through the incorporation of the emission modelling of the tundra snow in the region of interest that is known to the authors [178]. An iterative approach to retrieving snow depth has been applied on an airborne radiometry dataset. We consider the inversion process, only as a mathematical/statistical approach to deriving the controlling parameters, using the physical foundations of the forward model. Priors are based on *in situ* measurements, and are adapted by comparing forward model with the observed emissions. A two-layer snowpack with a developing depth hoar and a developing wind slab on top of a fixed depth hoar layer after a certain snow depth was imposed to the inversion model, whereas the validity of this assumption was determined in our previous research [178].

The inversion process is applied in two steps. First, T_b footprints within the interquartile range of snow depth intervals were used for our inversion algorithm with limited success. Then, we applied the inversion in a synthetic approach. Expectedly, the results significantly improved with a snow depth RMSE of 0.07 cm, compared to former analysis with an RMSE of 21.8 cm. This improvement is due to the averaging process that minimizes random errors related to T_b observations and snow depth variability in the footprint scale. The approaches used in the MCMC simulation approach underlines three major findings that satisfy the objectives: 1) informative priors leads to a successful retrieval, 2) we need to dictate a tractable and robust snow structure in the inversion process for an accurate inversion, and 3) the impact of observation scale (both remote sensing observation and *in situ* field measurement) is significant for the retrieval accuracy. In this study, the shallow snowpacks (depth hoar forming phase) and the deep snowpacks (wind slab development phase) were retrieved separately. Further improvement requires probabilistic classification prior. By applying a probability of snow structure or snow history, a snowpacks likelihood of a depth hoar forming phase or wind slab development phase can be determined before the retrieval. This application coupled with the Bayesian approach allows us to realize the physically-based inversion of a stochastic process.

Chapter 7

General Conclusions

7.1 Summary

This thesis has demonstrated a Bayesian approach for SWE retrieval in Tundra regions, using airborne PM observations, *in situ* measurements are generalized for a better parameterization of the emission model. The analysis is supported by an explanation of snowpack physical properties impacts on the upcoming emission based on physical descriptions in empirical approaches and forward emission models. Introductory chapters [1-3], presented the main research questions and objectives, followed by descriptions of snowpack microstructure and evolution, the physics of microwave emissions in a snowpack, and the interpretation of observed brightness temperatures to retrieve snowpack physical properties.

The background chapters explained the impacts of effective components in controlling microwave emission. Chapter 4 describes in greater detail current retrieval approaches in PM remote sensing of snow. Spaceborne SWE products are not commonly employed in operational hydrological and hydroclimate modeling applications even at regional scales. Various causes have been suggested for their insufficient accuracy, the coarse spatial resolution of PM observations that observe highly aggregated snowpack properties at the spaceborne scale, and inadequacies during the retrieval process that are caused by uncertainties with the forward emission modeling of snow and challenges to find robust parameterizations of the models. In this chapter, snow depth and SWE retrieval methods using PM remote sensing observations have been reviewed and concluded that snowpack parameterization is key to accurate retrieval.

Chapter 5 presented the application of Dense Media Radiative Transfer Theory for Multi Layered (DMRT-ML) snowpack to predict the passive microwave response from airborne observations over shallow, dense, slab-layered tundra snow. Airborne radiometer observations coordinated with ground-based *in situ* snow measurements were acquired in the Canadian high Arctic near Eureka, NT, in April 2011. The DMRT-ML was parameterized with the *in situ* snow measurements using a two-layer snowpack and executed in two configurations: a depth hoar and a wind slab dominated pack. With these two configurations, the calibrated DMRT-ML successfully predicted the T_b V 37 GHz response (R correlation of 0.83) when compared with the observed airborne T_b footprints containing snowpits measurements. Using this calibrated model, the DMRT-ML was applied to the whole study region. At the satellite observation scale, observations from the Advanced Microwave Scanning Radiometer-Earth Observing System (AMSR-E) over the study area reflected seasonal differences between T_b V 37 GHz and T_b V 19 GHz that supports the hypothesis of the development of an early season volume scattering depth hoar layer, followed by the growth of the late season emission-dominated wind slab layer. This research highlighted the necessity of considering the two-part emission characteristics of a slab-dominated tundra snowpack at T_b 37 GHz.

Chapter 6 explained the development of a Bayesian Algorithm for Snow Water Equivalent (SWE) Estimation (BASE), which uses the Monte Carlo Markov Chain (MCMC) method to estimate SWE for tundra snow from airborne radiometer T_b. In this experiment, datasets of 464 footprints in the Eureka region were coupled with airborne passive microwave observations from a wide area flight conducted in 2011. T_b at 18.7 and 36.5 GHz was available. The algorithm searches optimum posterior probability distribution of snow properties using a cost function between physically based emission simulations and brightness temperature (T_b) observations. A two-layer snowpack is assumed to simulate emission using the Dense Media Radiative Transfer-Multi Layered (DMRT-ML) model. The two-layer wind slab and depth hoar assumption is based on local snow cover knowledge from previous research in the study area. The inversion was also applied in a semi-synthetic approach, and results significantly improved with a snow depth RMSE of 0.07 cm, compared to the former analysis with a snow depth RMSE of 21.8 cm. Our work verifies the feasibility and applicability of the proposed methodology regionally for airborne retrieval. This framework reinforces the tractable applicability of a physics-based radiative transfer model in SWE retrievals. We suggest re-evaluation of the computation costs, examining the use of faster search methods, and inclusion of a Gaussian function in the emission model as potential future works.

Overall, this research contributes to retrieval frameworks and methodologies that will facilitate the development of a Bayesian PM based snow property retrieval using spaceborne observations. Contributions of this work and the significance of this research can be discussed in three aspects:

1. While the spatial resolution problem of spaceborne PM observations is largely in the realm of engineering design and constrained by physical restrictions, a better understanding of the range of retrieval methodologies developed and adopted can provide the clarity needed to move the thinking forward in this important field.
2. A framework for forward emission modelling using generalized stratigraphy of snowpacks is presented and the results are compared with coordinated PM airborne observations after employing required pre-processes. This analysis shows the significance of integrating modified climatology of snowpacks based on our field knowledge to improve parameterizing emisssion models.
3. A representative emission model can be employed in a retrieval system to estimate snowpack physical properties. A Bayesian Algorithm for Snow Water Equivalent Estimation (BASE) inversion is proposed for the retrieval that is based on parameterizing snowpack stratigraphy. This retrieval algorithm is developed by taking prior information into account, while minimizing dependence upon it, as accurate ancillary datasets are not globally available.

The challenge of using SWE products derived from spaceborne PM in operational hydrological and hydroclimate modeling applications is very demanding with limited uptake by these systems. The last two contributions of this thesis can be extended to employ retrievals at regional scales using spaceborne applications, which can provide valuable datasets for applications ranging from modeling snow variations in a small catchment to global climatologic studies.

7.2 Limitations

A comprehensive dataset of multi-scale observations is needed for full understanding of the spatial and quantitative distribution of uncertainties. Addressing uncertainties caused by generalization and aggregation of *in situ* measurements requires simultaneous T_b observations of ground-based and airborne scales. Unfortunately, our dataset did not include ground-based T_b observations, and no significant conclusions could be made by comparing airborne T_bs at different high and low altitudes with footprints of 850 m —510 m and 120 m —102 m, respectively. A high standard deviation of 20 K was calculated for low altitude

T_bs found within the IFOV of high altitude footprints, showing a high uncertainty level of observations. On the other hand, the flight lines were designed in a pattern to assist in the scaling up of T_bs from the airborne to the satellite scale and to ensure complete coverage at different spatial resolutions of T_b products. A time series spaceborne observation facilitated the interpretation of the observed signature, but no statistical comparison was possible with the limited airborne observations that covered the study area in four days.

In our study, grain sizes were measured by average maximum and minimum diameters, which could not be used directly as DMRT-ML's inputs. In addition, there was no empirical transformation function from D_{max} or D_{min} to optical diameter (D_{opt}) to be inputted in DMRT-ML. Grain size values, measured in the field, were used in the generalization of snowpack stratigraphy. We then employed effective grain sizes (D_{eff}), based on previous research in the emission model. This research could have benefited from the use of another metric for grain measurements such as SSA that could have been employed in an emission model after applying a scaling factor.

7.3 Future Work

Hydrologically-important snowpack properties such as snow depth, SWE and snow state can be retrieved as a result of the sensitivity of a microwave's signature to snowpack properties. A microwave emission signature is also affected by seasonal snowpack evolution, through changes in key parameters of the snowpack that control the emission. Consistent time series of passive microwave observations in a heritage record of almost 40 years provide a good source for times series analysis and inter-seasonal variability detection. A daily near-real time snow depth/SWE product with improved spatial resolution can provide required information for operational hydrological, climatological and agricultural applications in local to global scales. It can also be used to develop operational forecast models such as weather forecasts, water supply prediction, and flood and avalanche forecasts that require near-real time observations to update the state variables in the model.

By improving retrieval algorithm architectures that better capture dynamic snowpack evolution processes, SWE estimates are likely to improve. Physical modeling facilitates controlling the emission signature with key components of the model such as grain size in a realistic approach. This physical control opens up the possibility to parameterize some of snowpack properties such as number of layers or grain size in an inverse iterative approach, which helps to improve our understanding of seasonal snow cover and leads to the creation of climatology stratigraphy maps including the microstructural properties of snowpack that are required for emission modeling. Available knowledge of snowpack properties in regional scales can help to build such maps. For instance, Sturm's snow classes can be used as a baseline (climatology density maps are available), and more details on snowpack stratigraphy can modify these snow classes. In addition, snowpack emission is highly sensitive to grain size, so estimation of a climatologic grain size seems essential in the field of radiometric observation of snow, and conclusively is a unique topic of research.

Due to low spatial resolution of PM remote sensing observations, specifically in passive microwave observations, distinct materials occupying a single pixel produce mixed signatures [103]. Accurate estimation of surface geophysical properties and enhancement of spatial resolution in passive microwave observations requires modeling of the mixed signatures of land covers in a footprint/grid cell [110]. To date, different techniques for the decomposition of signature and subpixel mapping of endmembers in multi-spectral and hyperspectral images have been developed. In optical remote sensing (multi or hyperspectral), spectral unmixing provides spatially detailed information by decomposing a mixed spectral signature into its endmembers fractional abundance [103]. Optical remote sensing observations have multiple spectral bands that allow employing linear and unlinear unmixing techniques to derive endmembers and their abundances. However, in PM observations, spectral resolution is not sufficient to solve the unmixing by similar proposed methods in multi- and hyperspectral images. For instance, the limited number of sensitive frequencies to snowpack properties in PM remote sensing does not let us employ developed approaches for endmember detection. To date, the disaggregation of passive radiometry-derived products has been employed in soil moisture products, including satellite-based, geoinformation-based, and model-based methods [153]; however, little interest has been found in the disaggregation of PM-derived SWE products. Investigations of the application of disaggregation methods for PM SWE retrieval while coupling emission knowledge would be a remarkable research topic.

Spatial resolution enhancement [3] can be also achieved by geostatistical solutions that have been proposed for carrying out subpixel mapping of land cover and so increasing the estimation accuracy in a pixel; however, as mentioned earlier, sub-pixel mapping of retrieved SWE is still a big challenge and there is only limited research on this topic, especially in regional applications. Successful implementations of geostatistical downscaling methods, such as adaptive area to point regression kriging (AATPRK) by Wang et al. [225], originally designed as a pan-sharpening tool, and geographically weighted area to point regression kriging (GWATPRK) by Jin et al. [93], which builds on the AATPRK method by employing geographically weighted regression (GWR), can be tested on SWE products to investigate their suitability.

References

[1] G-portal: Global portal system. https://gportal.jaxa.jp/gpr/. Accessed: 2019-04-08.

[2] Canadian cryospheric information network:snow water equivalent. https://ccin.ca/ccw/snow/current/swe. Accessed: 2019-04-03.

[3] Copernicus imaging microwave radiometer: the passive microwave sattelite mission for eu copernicus. https://cimr.eu. Accessed: 2019-01-15.

[4] Globsnow snow products. http://www.globsnow.info. Accessed: 2019-04-08.

[5] K. M. Andreadis, P. Storck, and D. P. Lettenmaier. Modeling snow accumulation and ablation processes in forested environments. *Water Resources Research*, 45(5), 2009.

[6] R. Armstrong, M. Brodzik, K. Knowles, and M. Savoie. Global monthly ease-grid snow water equivalent climatology. *Digital media*, 2005.

[7] R. L. Armstrong and E. Brun. *Snow and climate: physical processes, surface energy exchange and modeling.* Cambridge University Press, 2008.

[8] L. Arnaud, G. Picard, N. Champollion, F. Domine, J. Gallet, E. Lefebvre, M. Fily, and J. Barnola. Measurement of vertical profiles of snow specific surface area with a 1 cm resolution using infrared reflectance: instrument description and validation. *Journal of Glaciology*, 57(201):17–29, 2011.

[9] J. Aschbacher. *Land surface studies and atmospheric effects by satellite microwave radiometry.* PhD thesis, Univ. of Innsbruck, 1993.

[10] A. P. Barrett. *National operational hydrologic remote sensing center snow data assimilation system (SNODAS) products at NSIDC.* National Snow and Ice Data Center, Cooperative Institute for Research in , 2003.

[11] K. J. Bormann, R. D. Brown, C. Derksen, and T. H. Painter. Estimating snow-cover trends from space. *Nature Climate Change*, 8(11):924, 2018.

[12] B. Brasnett. A global analysis of snow depth for numerical weather prediction. *Journal of Applied Meteorology*, 38(6):726–740, 1999.

[13] M. J. Brodzik, B. Billingsley, T. Haran, B. Raup, and M. H. Savoie. Ease-grid 2.0: Incremental but significant improvements for earth-gridded data sets. *ISPRS International Journal of Geo-Information*, 1(1):32–45, 2012.

[14] R. Brown, D. Tapsoba, and C. Derksen. Evaluation of snow water equivalent datasets over the saint-maurice river basin region of southern québec. *Hydrological Processes*, 32(17):2748–2764, 2018.

[15] R. D. Brown, B. Brasnett, and D. Robinson. Gridded north american monthly snow depth and snow water equivalent for gcm evaluation. *Atmosphere-Ocean*, 41(1):1–14, 2003.

[16] L. Brucker, G. Picard, and M. Fily. Snow grain-size profiles deduced from microwave snow emissivities in antarctica. *Journal of Glaciology*, 56(197):514–526, 2010.

[17] L. Brucker, C. Hiemstra, H.-P. Marshall, K. Elder, R. De Roo, M. Mousavi, F. Bliven, W. Peterson, J. Deems, P. Gadomski, et al. A first overview of snowex ground-based remote sensing activities during the winter 2016–2017. In *Geoscience and Remote Sensing Symposium (IGARSS), 2017 IEEE International*, pages 1391–1394. IEEE, 2017.

[18] E. Brun, E. Martin, V. Simon, C. Gendre, and C. Coleou. An energy and mass model of snow cover suitable for operational avalanche forecasting. *Journal of Glaciology*, 35(121):333–342, 1989.

[19] E. Brun, P. David, M. Sudul, and G. Brunot. A numerical model to simulate snow-cover stratigraphy for operational avalanche forecasting. *Journal of Glaciology*, 38 (128):13–22, 1992.

[20] S. Chandrasekhar. *Radiative transfer*. Courier Corporation, 2013.

[21] A. Chang and L. Tsang. A neural network approach to inversion of snow water equivalent from passive microwave measurements. *Hydrology Research*, 23(3):173–182, 1992.

[22] A. Chang, J. Foster, and D. Hall. Effects of forest on the snow parameters derived from microwave measurements during the boreas winter field campaign. *Hydrological Processes*, 10(12):1565–1574, 1996.

[23] A. Chang, J. Foster, R. Kelly, E. Josberger, R. Armstrong, and N. Mognard. Analysis of ground-measured and passive-microwave-derived snow depth variations in midwinter across the northern great plains. *Journal of Hydrometeorology*, 6(1):20–33, 2005.

[24] A. T. Chang, R. Kelly, J. L. Foster, and T. Koike. Estimation of snow depth from amsr-e in the game/ceop siberia experiment region. In *Geoscience and Remote Sensing Symposium, 2004. IGARSS'04. Proceedings. 2004 IEEE International*, volume 6, pages 3670–3673. IEEE, 2004.

[25] A. T. C. Chang, J. L. Foster, D. K. Hall, A. Rango, and B. K. Hartline. Snow Water Equivalent Estimation By Microwave Radiometry. *Cold Regions Scientific Publishing Company*, 5:259–267, 1982.

[26] A. T. C. Chang, J. Foster, and D. Hall. NIMBUS-7 SMMR Derived Global Snow Cover Parameters. In *Annals of Glaciology*, volume 235, pages 39–44, 1987.

[27] W. Chang, S. Tan, J. Lemmetyinen, L. Tsang, X. Xu, and S. H. Yueh. Dense media radiative transfer applied to snowscat and snowsar. *IEEE Journal of Selected Topics in Applied Earth Observations and Remote Sensing*, 7(9):3811–3825, 2014.

[28] J. Cohen and D. Rind. The effect of snow cover on the climate. *Journal of Climate*, 4(7):689–706, 1991.

[29] J. Cohen, J. Lemmetyinen, J. Pulliainen, K. Heinilä, F. Montomoli, J. Seppänen, and M. T. Hallikainen. The effect of boreal forest canopy in satellite snow mappinga multisensor analysis. *IEEE Transactions on Geoscience and Remote Sensing*, 53(12): 6593–6607, 2015.

[30] S. Colbeck. A simulation of the enrichment of atmospheric pollutants in snow cover runoff. *Water Resources Research*, 17(5):1383–1388, 1981.

[31] S. Colbeck. An overview of seasonal snow metamorphism. *Reviews of Geophysics*, 20(1):45–61, 1982.

[32] S. Colbeck. Theory of metamorphism of dry snow. *Journal of Geophysical Research: Oceans*, 88(C9):5475–5482, 1983.

[33] S. Colbeck. others. 1990. the international classification for seasonal snow on the ground. wallingford, oxon, international association of scientific hydrology. *International Commission on Snow and Ice*, 7.

[34] A. Denoth. Snow dielectric measurements. *Advances in Space Research*, 9(1):233–243, 1989.

[35] C. Derksen. The contribution of amsr-e 18.7 and 10.7 ghz measurements to improved boreal forest snow water equivalent retrievals. *Remote Sensing of Environment*, 112 (5):2701–2710, 2008.

[36] C. Derksen, A. Walker, and B. Goodison. A comparison of 18 winter seasons of in situ and passive microwave-derived snow water equivalent estimates in western canada. *Remote Sensing of Environment*, 88(3):271–282, 2003.

[37] C. Derksen, P. Toose, A. Rees, L. Wang, M. English, A. Walker, and M. Sturm. Development of a tundra-specific snow water equivalent retrieval algorithm for satellite passive microwave data. *Remote Sensing of Environment*, 114(8):1699–1709, 2010.

[38] C. Derksen, P. Toose, J. Lemmetyinen, J. Pulliainen, A. Langlois, N. Rutter, and M. Fuller. Evaluation of passive microwave brightness temperature simulations and snow water equivalent retrievals through a winter season. *Remote Sensing of Environment*, 117:236–248, 2012.

[39] C. Derksen, R. Brown, L. Mudryk, and K. Luojus. Snowpex the satellite snow product intercomparison and evaluation experiment methods and protocols for intercomparing and validating swe. Technical report, European Space Agency, 07 2014.

[40] C. Derksen, J. Lemmetyinen, P. Toose, A. Silis, J. Pulliainen, and M. Sturm. Physical properties of arctic versus subarctic snow: Implications for high latitude passive microwave snow water equivalent retrievals. *Journal of Geophysical Research: Atmospheres*, 119(12):7254–7270, 2014.

[41] D. R. DeWalle and A. Rango. *Principles of snow hydrology.* Cambridge University Press, 2008.

[42] K. F. Dewey and R. Heim. Satellite observations of variations in southern hemisphere snow cover. 1983.

[43] A. J. Dietz, C. Kuenzer, U. Gessner, and S. Dech. Remote sensing of snow–a review of available methods. *International Journal of Remote Sensing*, 33(13):4094–4134, 2012.

[44] S. L. Dingman. *Physical hydrology.* Prentice Hall, 1994.

[45] J. Dong, J. P. Walker, and P. R. Houser. Factors affecting remotely sensed snow water equivalent uncertainty. *Remote Sensing of Environment*, 97(1):68–82, 2005.

[46] M. Durand and D. Liu. The need for prior information in characterizing snow water equivalent from microwave brightness temperatures. *Remote Sensing of Environment*, 126:248–257, 2012.

[47] M. Durand and S. A. Margulis. Feasibility test of multifrequency radiometric data assimilation to estimate snow water equivalent. *Journal of Hydrometeorology*, 7(3): 443–457, 2006.

[48] M. Durand and S. A. Margulis. Correcting first-order errors in snow water equivalent estimates using a multifrequency, multiscale radiometric data assimilation scheme. *Journal of Geophysical Research: Atmospheres*, 112(D13), 2007.

[49] M. Durand, E. J. Kim, and S. A. Margulis. Quantifying uncertainty in modeling snow microwave radiance for a mountain snowpack at the point-scale, including stratigraphic effects. *IEEE Transactions on Geoscience and Remote Sensing*, 46(6): 1753–1767, 2008.

[50] M. Durand, E. J. Kim, and S. A. Margulis. Radiance assimilation shows promise for snowpack characterization. *Geophysical Research Letters*, 36(2), 2009.

[51] M. Durand, E. J. Kim, S. A. Margulis, and N. P. Molotch. A first-order characterization of errors from neglecting stratigraphy in forward and inverse passive microwave modeling of snow. *IEEE Geoscience and Remote Sensing Letters*, 8(4):730–734, 2011.

[52] S. A. Edlund, M.-k. Woo, and K. L. Young. Climate, hydrology and vegetation patterns hot weather creek, ellesmere island, arctic canada: Paper presented at the 8th northern res. basins symposium/workshop (abisko, sweden-march 1990). *Hydrology Research*, 21(4-5):273–286, 1990.

[53] M. A. El-Rayes and F. T. Ulaby. Microwave dielectric spectrum of vegetation-part i: Experimental observations. *IEEE Transactions on Geoscience and Remote Sensing*, (5):541–549, 1987.

[54] C. Elachi and J. J. Van Zyl. *Introduction to the physics and techniques of remote sensing*, volume 28. John Wiley & Sons, 2006.

[55] K. Elder, D. Cline, G. E. Liston, and R. Armstrong. Nasa cold land processes experiment (clpx 2002/03): Field measurements of snowpack properties and soil moisture. *Journal of Hydrometeorology*, 10(1):320–329, 2009.

[56] Environment and C. C. C. (ECCC). Eureka weather station, canadian climate normal, 1981-2010. Technical report, Environment Canada, 2017.

[57] R. Essery and J. Pomeroy. Vegetation and topographic control of wind-blown snow distributions in distributed and aggregated simulations for an arctic tundra basin. *Journal of Hydrometeorology*, 5(5):735–744, 2004.

[58] R. Essery, S. Morin, Y. Lejeune, and C. B. Ménard. A comparison of 1701 snow models using observations from an alpine site. *Advances in water resources*, 55: 131–148, 2013.

[59] P. E. Farnes, N. R. Peterson, B. E. Goodison, and R. P. Richards. Metrication of manual snow sampling equipment by western snow conference metrication committee. In *Proceedings of the Western Snow Conference*, volume 50, pages 120–132, 1982.

[60] P. Ferrazzoli and L. Guerriero. Passive microwave remote sensing of forests: A model investigation. *IEEE Transactions on Geoscience and Remote Sensing*, 34(2):433–443, 1996.

[61] P. Ferrazzoli, L. Guerriero, and J.-P. Wigneron. Simulating l-band emission of forests in view of future satellite applications. *IEEE Transactions on Geoscience and Remote Sensing*, 40(12):2700–2708, 2002.

[62] C. Fierz, R. L. Armstrong, Y. Durand, P. Etchevers, E. Greene, D. M. McClung, K. Nishimura, P. K. Satyawali, and S. A. Sokratov. *The international classification for seasonal snow on the ground*, volume 25. UNESCO/IHP Paris, 2009.

[63] M. G. Flanner and C. S. Zender. Linking snowpack microphysics and albedo evolution. *Journal of Geophysical Research: Atmospheres*, 111(D12), 2006.

[64] C. G. Fletcher, P. J. Kushner, A. Hall, and X. Qu. Circulation responses to snow albedo feedback in climate change. *Geophysical Research Letters*, 36(9), 2009.

[65] B. A. Forman and R. H. Reichle. Using a support vector machine and a land surface model to estimate large-scale passive microwave brightness temperatures over snow-covered land in north america. *IEEE Journal of Selected Topics in Applied Earth Observations and Remote Sensing*, 8(9):4431–4441, 2015.

[66] J. Foster, D. Hall, A. Chang, and A. Rango. An overview of passive microwave snow research and results. *Reviews of Geophysics*, 22(2):195–208, 1984.

[67] J. Foster, A. Chang, D. Hall, and A. Rango. Derivation of snow water equivalent in boreal forests using microwave radiometry. *Arctic*, pages 147–152, 1991.

[68] J. Foster, G. Liston, R. Koster, R. Essery, H. Behr, L. Dumenil, D. Verseghy, S. Thompson, D. Pollard, and J. Cohen. Snow cover and snow mass intercomparisons of general circulation models and remotely sensed datasets. *Journal of Climate*, 9 (2):409–426, 1996.

[69] J. Foster, A. Chang, and D. Hall. Comparison of snow mass estimates from a prototype passive microwave snow algorithm, a revised algorithm and a snow depth climatology. *Remote sensing of environment*, 62(2):132–142, 1997.

[70] J. Foster, D. Hall, R. Kelly, and L. Chiu. Seasonal snow extent and snow mass in south america using smmr and ssm/i passive microwave data (1979–2006). *Remote Sensing of Environment*, 113(2):291–305, 2009.

[71] J. L. Foster, C. Sun, J. P. Walker, R. Kelly, A. Chang, J. Dong, and H. Powell. Quantifying the uncertainty in passive microwave snow water equivalent observations. *Remote Sensing of Environment*, 94(2):187–203, jan 2005. ISSN 00344257. doi: 10.1016/j.rse.2004.09.012. URL http://linkinghub.elsevier.com/retrieve/pii/S0034425704002950.

[72] J. L. Foster, C. Sun, J. P. Walker, R. Kelly, A. Chang, J. Dong, and H. Powell. Quantifying the uncertainty in passive microwave snow water equivalent observations. *Remote Sensing of environment*, 94(2):187–203, 2005.

[73] J. L. Foster, D. K. Hall, J. B. Eylander, G. A. Riggs, S. V. Nghiem, M. Tedesco, E. Kim, P. M. Montesano, R. E. Kelly, K. A. Casey, et al. A blended global snow product using visible, passive microwave and scatterometer satellite data. *International journal of remote sensing*, 32(5):1371–1395, 2011.

[74] A. Frei, M. Tedesco, S. Lee, J. Foster, D. K. Hall, R. Kelly, and D. A. Robinson. A review of global satellite-derived snow products. *Advances in Space Research*, 50(8): 1007–1029, 2012.

[75] J.-C. Gallet, F. Domine, C. Zender, and G. Picard. Measurement of the specific surface area of snow using infrared reflectance in an integrating sphere at 1310 and 1550 nm. *The Cryosphere*, 3(2):167–182, 2009.

[76] A. Gelfan, J. Pomeroy, and L. Kuchment. Modeling forest cover influences on snow accumulation, sublimation, and melt. *Journal of Hydrometeorology*, 5(5):785–803, 2004.

[77] A. Gelman, H. S. Stern, J. B. Carlin, D. B. Dunson, A. Vehtari, and D. B. Rubin. *Bayesian data analysis*. Chapman and Hall/CRC, 2013.

[78] J. Giddings and E. LaChapelle. Diffusion theory applied to radiant energy distribution and albedo of snow. *Journal of geophysical research*, 66(1):181–189, 1961.

[79] B. Goodison and A. Walker. Use of snow cover derived from satellite passive microwave data as an indicator of climate change. *Annals of glaciology*, 17:137–142, 1993.

[80] J. P. Grant, K. Saleh-Contell, J.-P. Wigneron, M. Guglielmetti, Y. H. Kerr, M. Schwank, N. Skou, and A. A. Van de Griend. Calibration of the l-meb model over a coniferous and a deciduous forest. *IEEE Transactions on Geoscience and Remote Sensing*, 46(3):808–818, 2008.

[81] T. C. Grenfell and S. G. Warren. Representation of a nonspherical ice particle by a collection of independent spheres for scattering and absorption of radiation. *Journal of Geophysical Research: Atmospheres*, 104(D24):31697–31709, 1999.

[82] N. Grody. Relationship between snow parameters and microwave satellite measurements: Theory compared with advanced microwave sounding unit observations from 23 to 150 ghz. *Journal of Geophysical Research: Atmospheres*, 113(D22), 2008.

[83] D. K. Hall, R. E. Kelly, J. L. Foster, and A. T. Chang. Estimation of snow extent and snow properties. *Encyclopedia of hydrological sciences*, 2006.

[84] M. Hallikainen, F. Ulaby, and M. Abdel-Razik. Measurements of the dielectric properties of snow in the 4-18 ghz frequency range. In *Microwave Conference, 1982. 12th European*, pages 151–156. IEEE, 1982.

[85] M. T. Hallikainen. Microwave radiometry of snow. *Advances in Space Research*, 9 (1):267–275, 1989.

[86] M. T. Hallikainen, F. T. Ulaby, M. C. Dobson, M. A. El-Rayes, and L.-K. Wu. Microwave dielectric behavior of wet soil-part 1: Empirical models and experimental observations. *IEEE Transactions on Geoscience and Remote Sensing*, (1):25–34, 1985.

[87] M. T. Hallikainen, F. T. Ulaby, and T. E. Van Deventer. Extinction behavior of dry snow in the 18-to 90-ghz range. *IEEE Transactions on Geoscience and Remote Sensing*, GE-25(6):737–745, 1987.

[88] M. T. Hallikainen, P. Halme, M. Takala, and J. Pulliainen. Combined active and passive microwave remote sensing of snow in finland. In *Geoscience and Remote Sensing Symposium, 2003. IGARSS'03. Proceedings. 2003 IEEE International*, volume 2, pages 830–832. Ieee, 2003.

[89] J. P. Hollinger, J. L. Peirce, and G. A. Poe. Ssm/i instrument evaluation. *IEEE Transactions on Geoscience and Remote Sensing*, 28(5):781–790, 1990.

[90] H. Huang, L. Tsang, E. G. Njoku, A. Colliander, T.-H. Liao, and K.-H. Ding. Propagation and scattering by a layer of randomly distributed dielectric cylinders using monte carlo simulations of 3d maxwell equations with applications in microwave interactions with vegetation. *IEEE Access*, 5:11985–12003, 2017.

[91] K. Imaoka, M. Kachi, A. Shibata, M. Kasahara, Y. Iida, Y. Tange, K. Nakagawa, and H. Shimoda. Five years of amsr-e monitoring and successive gcom-w1/amsr2 instrument. In *Sensors, Systems, and Next-Generation Satellites XI*, volume 6744, page 67440J. International Society for Optics and Photonics, 2007.

[92] K. Imaoka, M. Kachi, M. Kasahara, N. Ito, K. Nakagawa, and T. Oki. Instrument performance and calibration of amsr-e and amsr2. *International archives of the photogrammetry, remote sensing and spatial information science*, 38(8):13–18, 2010.

[93] Y. Jin, Y. Ge, J. Wang, G. Heuvelink, and L. Wang. Geographically weighted area-to-point regression kriging for spatial downscaling in remote sensing. *Remote Sensing*, 10(4):579, 2018.

[94] Y.-Q. Jin. *Electromagnetic scattering modelling for quantitative remote sensing.* World Scientific, 1993.

[95] R. Jordan. A one-dimensional temperature model for a snow cover: Technical documentation for sntherm. 89. Technical report, COLD REGIONS RESEARCH AND ENGINEERING LAB HANOVER NH, 1991.

[96] E. G. Josberger and N. M. Mognard. A passive microwave snow depth algorithm with a proxy for snow metamorphism. *Hydrological Processes*, 16(8):1557–1568, 2002.

[97] T. Kawanishi, T. Sezai, Y. Ito, K. Imaoka, T. Takeshima, Y. Ishido, A. Shibata, M. Miura, H. Inahata, and R. W. Spencer. The advanced microwave scanning radiometer for the earth observing system (amsr-e), nasda's contribution to the eos for global energy and water cycle studies. *IEEE Transactions on Geoscience and Remote Sensing*, 41(2):184–194, 2003.

[98] R. Kelly. The amsr-e snow depth algorithm: Description and initial results. *Journal of the Remote Sensing Society of Japan*, 29(1):307–317, 2009.

[99] R. Kelly, A. Chang, L. Tsang, and C. Chen. Parameterization of snowpack grain size for global satellite microwave estimates of snow depth. In *Geoscience and Remote Sensing Symposium, 2002. IGARSS'02. 2002 IEEE International*, volume 1, pages 686–688. IEEE, 2002.

[100] R. Kelly, A. Chang, L. Tsang, and J. Foster. A prototype AMSR-E global snow area and snow depth algorithm. *IEEE Transactions on Geoscience and Remote Sensing*, 41(2):230–242, feb 2003. ISSN 0196-2892. doi: 10.1109/TGRS.2003.809118. URL `http://ieeexplore.ieee.org/lpdocs/epic03/wrapper.htm?arnumber=1196041`.

[101] R. E. Kelly, N. Saberi, and Q. Li. The amsr2 satellite-based microwave snow algorithm (smsa) to estimate regional to global snow depth and snow water equivalent. In *AGU Fall Meeting Abstracts*, 2017.

[102] M. C. Kennedy and A. O'Hagan. Bayesian calibration of computer models. *Journal of the Royal Statistical Society: Series B (Statistical Methodology)*, 63(3):425–464, 2001.

[103] N. Keshava and J. F. Mustard. Spectral unmixing. *IEEE signal processing magazine*, 19(1):44–57, 2002.

[104] J. King, R. Kelly, A. Kasurak, C. Duguay, G. Gunn, N. Rutter, T. Watts, and C. Derksen. Spatio-temporal influence of tundra snow properties on ku-band (17.2 ghz) backscatter. *Journal of Glaciology*, 61(226):267–279, 2015.

[105] K. Knowles, M. Savoie, R. Armstrong, and M. Brodzik. Amsr-e/aqua daily ease-grid brightness temperatures. *Digital media*, 2006.

[106] A. Kontu, J. Lemmetyinen, J. Vehviläinen, L. Leppänen, and J. Pulliainen. Coupling snowpack-modeled grain size parameters with the hut snow emission model. *Remote sensing of environment*, 194:33–47, 2017.

[107] Q. Krol and H. Löwe. Relating optical and microwave grain metrics of snow: the relevance of grain shape. *The Cryosphere*, 10(EPFL-ARTICLE-225444):2847–2863, 2016.

[108] N. Kruopis, J. Praks, A. N. Arslan, H. M. Alasalmi, J. T. Koskinen, and M. T. Hallikainen. Passive microwave measurements of snow-covered forest areas in emac'95. *IEEE Transactions on Geoscience and Remote Sensing*, 37(6):2699–2705, 1999.

[109] K. F. Kunzi, S. Patil, and H. Rott. Snow-cover parameters retrieved from nimbus-7 scanning multichannel microwave radiometer (smmr) data. *IEEE Transactions on Geoscience and Remote Sensing*, (4):452–467, 1982.

[110] L. Kurvonen and M. Hallikainen. Influence of land-cover category on brightness temperature of snow. *IEEE Transactions on geoscience and remote sensing*, 35(2): 367–377, 1997.

[111] A. Langlois, A. Royer, F. Dupont, A. Roy, K. Goïta, and G. Picard. Improved corrections of forest effects on passive microwave satellite remote sensing of snow over boreal and subarctic regions. *IEEE Transactions on Geoscience and Remote Sensing*, 49(10):3824–3837, 2011.

[112] A. Langlois, A. Royer, C. Derksen, B. Montpetit, F. Dupont, and K. Goïta. Coupling the snow thermodynamic model snowpack with the microwave emission model of layered snowpacks for subarctic and arctic snow water equivalent retrievals. *Water Resources Research*, 48(12), 2012.

[113] F. Larue, A. Royer, D. De Sève, A. Langlois, A. Roy, and L. Brucker. Validation of globsnow-2 snow water equivalent over eastern canada. *Remote sensing of environment*, 194:264–277, 2017.

[114] F. Larue, A. Royer, D. D. Sève, A. Roy, and E. Cosme. Assimilation of passive microwave amsr-2 satellite observations in a snowpack evolution model over northeastern canada. *Hydrology and Earth System Sciences*, 22(11):5711–5734, 2018.

[115] L. Legagneux, A. Cabanes, and F. Dominé. Measurement of the specific surface area of 176 snow samples using methane adsorption at 77 k. *Journal of Geophysical Research: Atmospheres*, 107(D17):ACH–5, 2002.

[116] M. Lehning, P. Bartelt, B. Brown, C. Fierz, and P. Satyawali. A physical snowpack model for the swiss avalanche warning: Part ii. snow microstructure. *Cold regions science and technology*, 35(3):147–167, 2002.

[117] J. Lemmetyinen, J. Pulliainen, A. Rees, A. Kontu, Y. Qiu, and C. Derksen. Multiple-layer adaptation of hut snow emission model: Comparison with experimental data. *IEEE Transactions on Geoscience and Remote Sensing*, 48(7):2781–2794, 2010.

[118] J. Lemmetyinen, A. Kontu, J. Pulliainen, J. Vehviläinen, K. Rautiainen, A. Wiesmann, C. Mätzler, C. Werner, H. Rott, T. Nagler, et al. Nordic snow radar experiment. *Geoscientific Instrumentation, Methods and Data Systems*, 5(2):403–415, 2016.

[119] J. Lemmetyinen, M. Schwank, K. Rautiainen, A. Kontu, T. Parkkinen, C. Mätzler, A. Wiesmann, U. Wegmüller, C. Derksen, P. Toose, et al. Snow density and ground permittivity retrieved from l-band radiometry: Application to experimental data. *Remote sensing of environment*, 180:377–391, 2016.

[120] J. Lemmetyinen, C. Derksen, H. Rott, G. Macelloni, J. King, M. Schneebeli, A. Wiesmann, L. Leppänen, A. Kontu, and J. Pulliainen. Retrieval of effective correlation length and snow water equivalent from radar and passive microwave measurements. *Remote Sensing*, 10(2):170, 2018.

[121] D. Li, M. Durand, and S. A. Margulis. Potential for hydrologic characterization of deep mountain snowpack via passive microwave remote sensing in the kern river basin, sierra nevada, usa. *Remote sensing of environment*, 125:34–48, 2012.

[122] D. Li, M. Durand, and S. A. Margulis. Estimating snow water equivalent in a sierra nevada watershed via spaceborne radiance data assimilation. *Water Resources Research*, 53(1):647–671, 2017.

[123] Q. Li and R. E. Kelly. Correcting satellite passive microwave brightness temperatures in forested landscapes using satellite visible reflectance estimates of forest transmissivity. *IEEE Journal of Selected Topics in Applied Earth Observations and Remote Sensing*, 10(9):3874–3883, 2017.

[124] D. Liang, X. Xu, L. Tsang, K. M. Andreadis, and E. G. Josberger. The effects of layers in dry snow on its passive microwave emissions using dense media radiative transfer theory based on the quasicrystalline approximation (qca/dmrt). *IEEE Transactions on Geoscience and Remote Sensing*, 46(11):3663–3671, 2008.

[125] K. G. Libbrecht. The physics of snow crystals. *Reports on progress in physics*, 68(4): 855, 2005.

[126] G. E. Liston. Representing subgrid snow cover heterogeneities in regional and global models. *Journal of climate*, 17(6):1381–1397, 2004.

[127] G. E. Liston and M. Sturm. Winter precipitation patterns in arctic alaska determined from a blowing-snow model and snow-depth observations. *Journal of hydrometeorology*, 3(6):646–659, 2002.

[128] H. Löwe and G. Picard. Microwave scattering coefficient of snow in memls and dmrt-ml revisited: the relevance of sticky hard spheres and tomography-based estimates of stickiness. *The Cryosphere*, 9(6):2101–2117, 2015.

[129] J. MacQueen et al. Some methods for classification and analysis of multivariate observations. In *Proceedings of the fifth Berkeley symposium on mathematical statistics and probability*, volume 1, pages 281–297. Oakland, CA, USA, 1967.

[130] V. Mahat and D. G. Tarboton. Representation of canopy snow interception, unloading and melt in a parsimonious snowmelt model. *Hydrological processes*, 28(26): 6320–6336, 2014.

[131] D. Marks, K. R. Cooley, D. C. Robertson, and A. Winstral. Long-term snow database, reynolds creek experimental watershed, idaho, united states. *Water Resources Research*, 37(11):2835–2838, 2001.

[132] S. J. Marshall. *The cryosphere*. Princeton University Press, 2011.

[133] C. Mätzler. Applications of the interaction of microwaves with the natural snow cover. *Remote sensing reviews*, 2(2):259–387, 1987.

[134] C. Mätzler. Passive microwave signatures of landscapes in winter. *Meteorology and Atmospheric Physics*, 54(1-4):241–260, 1994.

[135] C. Matzler. Microwave permittivity of dry snow. *IEEE Transactions on Geoscience and Remote Sensing*, 34(2):573–581, 1996.

[136] C. Matzler. Microwave properties of ice and snow. In *Solar System Ices*, pages 241–257. Springer, 1998.

[137] C. Mätzler. Relation between grain-size and correlation length of snow. *Journal of Glaciology*, 48(162):461–466, 2002.

[138] C. Mätzler. Notes on microwave radiation from snow samples and emission of layered snowpacks. Technical report, Inst. Appl. Phys., Univ. Bern, Bern, Switzerland, 2004.

[139] C. Mätzler. *Thermal microwave radiation: applications for remote sensing*. IET, 2006. ISBN 9780863415739.

[140] C. Mätzler and A. Wiesmann. Extension of the microwave emission model of layered snowpacks to coarse-grained snow. *Remote Sensing of Environment*, 70(3):317–325, 1999.

[141] C. Matzler, E. Schanda, and W. Good. Towards the definition of optimum sensor specifications for microwave remote sensing of snow. *IEEE Transactions on Geoscience and Remote Sensing*, (1):57–66, 1982.

[142] T. Mo, B. Choudhury, T. Schmugge, J. Wang, and T. Jackson. A model for microwave emission from vegetation-covered fields. *Journal of Geophysical Research: Oceans*, 87(C13):11229–11237, 1982.

[143] B. Montpetit, A. Royer, A. Langlois, M. Chum, P. Cliche, A. Roy, N. Champollion, G. Picard, F. Domine, and R. Obbard. In-situ measurements for snow grain size and shape characterization using optical methods. In *Proc. Eastern Snow Conf*, volume 68, pages 173–188, 2011.

[144] L. Mudryk, C. Derksen, P. Kushner, and R. Brown. Characterization of northern hemisphere snow water equivalent datasets, 1981–2010. *Journal of Climate*, 28(20): 8037–8051, 2015.

[145] J. Muñoz, J. Infante, T. Lakhankar, R. Khanbilvardi, P. Romanov, N. Krakauer, and A. Powell. Synergistic use of remote sensing for snow cover and snow water equivalent estimation. *British Journal of Environment and Climate Change*, 3(4): 612, 2013.

[146] T. Nagler, G. Bippus, C. Derksen, R. Fernandes, and K. Luojus. The satellite snow product intercomparison and evaluation experiment report on 1 st international satellite snow products intercomparison workshop (isspi -1). Technical report, NOAA Center for Weather Climate Prediction (NCWCP), 07 2014.

[147] U. Nakaya and J. Marshall. Snow crystals. *American Journal of Physics*, 22:573–573, 1954.

[148] E. G. Njoku, T. J. Jackson, V. Lakshmi, T. K. Chan, and S. V. Nghiem. Soil moisture retrieval from amsr-e. *IEEE transactions on Geoscience and remote sensing*, 41(2): 215–229, 2003.

[149] T. H. Painter, N. P. Molotch, M. Cassidy, M. Flanner, and K. Steffen. Contact spectroscopy for determination of stratigraphy of snow optical grain size. *Journal of Glaciology*, 53(180):121–127, 2007.

[150] J. Pan, M. Durand, M. Sandells, J. Lemmetyinen, E. J. Kim, J. Pulliainen, A. Kontu, and C. Derksen. Differences between the hut snow emission model and memls and their effects on brightness temperature simulation. *IEEE Trans. Geoscience and Remote Sensing*, 54(4):2001–2019, 2016.

[151] J. Pan, M. T. Durand, B. J. Vander Jagt, and D. Liu. Application of a Markov Chain Monte Carlo algorithm for snow water equivalent retrieval from passive microwave measurements. *Remote Sensing of Environment*, 192:150–165, 2017. ISSN 00344257. doi: 10.1016/j.rse.2017.02.006. URL `http://dx.doi.org/10.1016/j.rse.2017.02.006`.

[152] M. Pardé, K. Goïta, A. Royer, and F. Vachon. Boreal forest transmissivity in the microwave domain using ground-based measurements. *IEEE Geoscience and Remote Sensing Letters*, 2(2):169–171, 2005.

[153] J. Peng, A. Loew, O. Merlin, and N. E. Verhoest. A review of spatial downscaling of satellite remotely sensed soil moisture. *Reviews of Geophysics*, 55(2):341–366, 2017.

[154] G. Picard and M. Fily. Surface melting observations in antarctica by microwave radiometers: Correcting 26-year time series from changes in acquisition hours. *Remote sensing of environment*, 104(3):325–336, 2006.

[155] G. Picard, L. Brucker, A. Roy, F. Dupont, M. Fily, A. Royer, and C. Harlow. Simulation of the microwave emission of multi-layered snowpacks using the dense media radiative transfer theory: the dmrt-ml model. *Geoscientific Model Development*, 6 (4):1061–1078, 2013.

[156] G. Picard, M. Sandells, and H. Löwe. Smrt: an active–passive microwave radiative transfer model for snow with multiple microstructure and scattering formulations (v1. 0). *Geoscientific Model Development*, 11(7):2763–2788, 2018.

[157] B. Pinzer and M. Schneebeli. Snow metamorphism under alternating temperature gradients: Morphology and recrystallization in surface snow. *Geophysical research letters*, 36(23), 2009.

[158] M. Proksch, H. Löwe, and M. Schneebeli. Density, specific surface area, and correlation length of snow measured by high-resolution penetrometry. *Journal of Geophysical Research: Earth Surface*, 120(2):346–362, 2015.

[159] J. Pulliainen. Mapping of snow water equivalent and snow depth in boreal and sub-arctic zones by assimilating space-borne microwave radiometer data and ground-based observations. *Remote sensing of Environment*, 101(2):257–269, 2006.

[160] J. Pulliainen and M. Hallikainen. Retrieval of regional snow water equivalent from space-borne passive microwave observations. *Remote sensing of environment*, 75(1): 76–85, 2001.

[161] J. Pulliainen, J.-P. Karna, and M. Hallikainen. Development of geophysical retrieval algorithms for the mimr. *IEEE Transactions on Geoscience and Remote Sensing*, 31 (1):268–277, 1993.

[162] J. T. Pulliainen, J. Grandell, and M. T. Hallikainen. Hut snow emission model and its applicability to snow water equivalent retrieval. *IEEE Transactions on Geoscience and Remote Sensing*, 37(3):1378–1390, 1999.

[163] Y. Qiu, J. Shi, J. Lemmetyinen, A. Kontu, J. Pulliainen, H. Guo, L. Jiang, J. R. Wang, M. Hallikainen, and L. Zhang. The atmosphere influence to amsr-e measurements over snow-covered areas: Simulation and experiments. In *Geoscience and Remote Sensing Symposium, 2009 IEEE International, IGARSS 2009*, volume 2, pages II–610. Ieee, 2009.

[164] A. Rees, J. Lemmetyinen, C. Derksen, J. Pulliainen, and M. English. Observed and modelled effects of ice lens formation on passive microwave brightness temperatures over snow covered tundra. *Remote Sensing of Environment*, 114(1):116–126, 2010.

[165] A. Rees, M. English, C. Derksen, P. Toose, and A. Silis. Observations of late winter canadian tundra snow cover properties. *Hydrological processes*, 28(12):3962–3977, 2014.

[166] W. G. Rees. *Remote sensing of snow and ice.* CRC press, 2005.

[167] R. H. Reichle. Data assimilation methods in the earth sciences. *Advances in water resources*, 31(11):1411–1418, 2008.

[168] M. Richardson, I. Davenport, and R. Gurney. Global snow mass measurements and the effect of stratigraphic detail on inversion of microwave brightness temperatures. In *The Earth's Hydrological Cycle*, pages 785–812. Springer, 2013.

[169] S. Rosenfeld and N. Grody. Anomalous microwave spectra of snow cover observed from special sensor microwave/imager measurements. *Journal of Geophysical Research: Atmospheres*, 105(D11):14913–14925, 2000.

[170] A. Roy, A. Royer, J.-P. Wigneron, A. Langlois, J. Bergeron, and P. Cliche. A simple parameterization for a boreal forest radiative transfer model at microwave frequencies. *Remote Sensing of Environment*, 124:371–383, 2012.

[171] A. Roy, G. Picard, A. Royer, and B. Montpetit. Brightness temperature simulations of the Canadian seasonal snowpack driven by measurements of the snow specific surface area. *IEEE Transactions on Geoscience and Remote Sensing*, 51(9):4692–4704, 2013. URL `http://ieeexplore.ieee.org/xpls/abs{_}all.jsp?arnumber=6476000`.

[172] A. Roy, A. Royer, B. Montpetit, P. Bartlett, and A. Langlois. Snow specific surface area simulation using the one-layer snow model in the canadian land surface scheme (class). *The Cryosphere*, 7(3):961–975, 2013.

[173] A. Roy, A. Royer, B. Montpetit, and A. Langlois. Microwave snow emission modeling of boreal forest environments. In *Geoscience and Remote Sensing Symposium (IGARSS), 2015 IEEE International*, pages 754–757. IEEE, 2015.

[174] V. Roy, K. Goïta, A. Royer, A. E. Walker, and B. E. Goodison. Snow water equivalent retrieval in a canadian boreal environment from microwave measurements using the hut snow emission model. *IEEE Transactions on Geoscience and Remote Sensing*, 42(9):1850–1859, 2004.

[175] A. Royer, K. Goïta, J. Kohn, and D. De Sève. Monitoring dry, wet, and no-snow conditions from microwave satellite observations. *IEEE Geoscience and Remote Sensing Letters*, 7(4):670–674, 2010.

[176] A. Royer, A. Roy, B. Montpetit, O. Saint-Jean-Rondeau, G. Picard, L. Brucker, and A. Langlois. Comparison of commonly-used microwave radiative transfer models for snow remote sensing. *Remote sensing of environment*, 190:247–259, 2017.

[177] N. Saberi and R. Kelly. An evaluation of dmrt-ml for amsr2 estimates of snow depth. In *Geoscience and Remote Sensing Symposium (IGARSS), 2014 IEEE International*, pages 1943–1946. IEEE, 2014.

[178] N. Saberi, R. Kelly, P. Toose, A. Roy, and C. Derksen. Modeling the observed microwave emission from shallow multi-layer tundra snow using dmrt-ml. *Remote Sensing*, 9(12):1327, 2017.

[179] J. Sacks, W. J. Welch, T. J. Mitchell, and H. P. Wynn. Design and analysis of computer experiments. *Statistical science*, pages 409–423, 1989.

[180] M. Sandells, R. Essery, N. Rutter, L. Wake, L. Leppänen, and J. Lemmetyinen. Microstructure representation of snow in coupled snowpack and microwave emission models. *The Cryosphere*, 11(1):229–246, 2017.

[181] E. Santi, S. Pettinato, S. Paloscia, P. Pampaloni, G. Fontanelli, A. Crepaz, and M. Valt. Monitoring of alpine snow using satellite radiometers and artificial neural networks. *Remote sensing of environment*, 144:179–186, 2014.

[182] E. Santi, S. Paloscia, P. Pampaloni, S. Pettinato, M. Brogioni, C. Xiong, and A. Crepaz. Analysis of microwave emission and related indices over snow using experimental data and a multilayer electromagnetic model. *IEEE Transactions on Geoscience and Remote Sensing*, 55(4):2097–2110, 2017.

[183] E. Schanda. *Physical fundamentals of remote sensing*. Springer Science & Business Media, 1986.

[184] E. Schanda, C. Matzler, and K. Kunzi. Microwave remote sensing of snow cover. *International Journal of Remote Sensing*, 4(1):149–158, 1983.

[185] T. J. Schmugge and T. J. Jackson. A dielectric model of the vegetation effects on the microwave emission from soils. *IEEE Transactions on Geoscience and Remote Sensing*, 30(4):757–760, 1992.

[186] J. R. Schott. *Remote sensing: the image chain approach*. Oxford University Press on Demand, 2007.

[187] R. A. Schowengerdt. *Remote sensing: models and methods for image processing*. Elsevier, 2006.

[188] P. Sellers, F. Hall, H. Margolis, B. Kelly, D. Baldocchi, G. den Hartog, J. Cihlar, M. G. Ryan, B. Goodison, P. Crill, et al. The boreal ecosystem–atmosphere study (boreas): an overview and early results from the 1994 field year. *Bulletin of the American Meteorological Society*, 76(9):1549–1577, 1995.

[189] M. C. Serreze, M. P. Clark, R. L. Armstrong, D. A. McGinnis, and R. S. Pulwarty. Characteristics of the western united states snowpack from snowpack telemetry (snotel) data. *Water Resources Research*, 35(7):2145–2160, 1999.

[190] E. A. Sharkov. *Passive microwave remote sensing of the Earth: physical foundations*. Springer Science & Business Media, 2003.

[191] S.-E. Shih, K.-H. Ding, J. Kong, Y. Yang, R. Davis, J. Hardy, and R. Jordan. Modeling of millimeter wave backscatter of time-varying snowcover. *Progress In Electromagnetics Research*, 16:305–330, 1997.

[192] P. Singh. *Snow and glacier hydrology*, volume 37. Springer Science & Business Media, 2001.

[193] O. Slaymaker and R. Kelly. *The cryosphere and global environmental change*. John Wiley & Sons, 2009.

[194] A. M. Snauffer, W. W. Hsieh, A. J. Cannon, and M. A. Schnorbus. Improving gridded snow water equivalent products in British Columbia, Canada: Multi-source data fusion by neural network models. *Cryosphere*, 12(3):891–905, 2018. ISSN 19940424. doi: 10.5194/tc-12-891-2018.

[195] M. Sturm and C. Benson. Scales of spatial heterogeneity for perennial and seasonal snow layers. *Annals of Glaciology*, 38:253–260, 2004.

[196] M. Sturm and C. S. Benson. Vapor transport, grain growth and depth-hoar development in the subarctic snow. *Journal of Glaciology*, 43(143):42–59, 1997.

[197] M. Sturm and G. E. Liston. The snow cover on lakes of the arctic coastal plain of alaska, usa. *Journal of Glaciology*, 49(166):370–380, 2003.

[198] M. Sturm, T. C. Grenfell, and D. K. Perovich. Passive microwave measurements of tundra and taiga snow covers in alaska, usa. *Annals of Glaciology*, 17:125–130, 1993.

[199] M. Sturm, J. Holmgren, and G. E. Liston. A seasonal snow cover classification system for local to global applications. *Journal of Climate*, 8(5):1261–1283, 1995.

[200] M. Sturm, B. Taras, G. E. Liston, C. Derksen, T. Jonas, and J. Lea. Estimating snow water equivalent using snow depth data and climate classes. *Journal of Hydrometeorology*, 11(6):1380–1394, 2010.

[201] M. Takala, K. Luojus, J. Pulliainen, C. Derksen, J. Lemmetyinen, J.-P. Kärnä, J. Koskinen, and B. Bojkov. Estimating northern hemisphere snow water equivalent for climate research through assimilation of space-borne radiometer data and ground-based measurements. *Remote Sensing of Environment*, 115(12):3517–3529, 2011.

[202] A. Tarantola. *Inverse problem theory and methods for model parameter estimation*, volume 89. siam, 2005.

[203] M. Tedesco. *Remote sensing of the cryosphere.* John Wiley & Sons, 2014.

[204] M. Tedesco and J. Jeyaratnam. A new operational snow retrieval algorithm applied to historical amsr-e brightness temperatures. *Remote Sensing*, 8(12):1037, 2016.

[205] M. Tedesco and E. J. Kim. Intercomparison of electromagnetic models for passive microwave remote sensing of snow. *IEEE Transactions on Geoscience and Remote Sensing*, 44(10):2654–2666, 2006.

[206] M. Tedesco and P. S. Narvekar. Assessment of the nasa amsr-e swe product. *IEEE Journal of Selected Topics in Applied Earth Observations and Remote Sensing*, 3(1): 141–159, 2010.

[207] M. Tedesco, R. Kelly, J. Foster, and A. Chang. Amsr-e/aqua daily l3 global snow water equivalent ease-grids. version 2. *AE_DySno. Boulder, Colorado USA. NASA National Snow and Ice Data Center Distributed Active Archive Center. doi: http://dx. doi. org/10.5067/AMSR-E/AE_DYSNO*, 2, 2004.

[208] M. Tedesco, J. Pulliainen, M. Takala, M. Hallikainen, and P. Pampaloni. Artificial neural network-based techniques for the retrieval of swe and snow depth from ssm/i data. *Remote sensing of Environment*, 90(1):76–85, 2004.

[209] M. Tedesco, M. Brodzik, R. Armstrong, M. Savoie, and J. Ramage. Pan arctic terrestrial snowmelt trends (1979–2008) from spaceborne passive microwave data and correlation with the arctic oscillation. *Geophysical Research Letters*, 36(21), 2009.

[210] M. Tiuri, A. Sihvola, E. Nyfors, and M. Hallikaiken. The complex dielectric constant of snow at microwave frequencies. *IEEE Journal of oceanic Engineering*, 9(5):377–382, 1984.

[211] J. Tong, S. J. Dery, P. L. Jackson, and C. Derksen. Testing snow water equivalent retrieval algorithms for passive microwave remote sensing in an alpine watershed of western canada. *Canadian Journal of Remote Sensing*, 36(sup1):S74–S86, 2010.

[212] P. Toose. Report 1: Pamarcmip 2011 airborne microwave radiometer data processing (service contract: Km040-11-1110r 0). Technical report, Environment Canada, 2011.

[213] A. M. Toure, K. Goïta, A. Royer, E. J. Kim, M. Durand, S. A. Margulis, and H. Lu. A case study of using a multilayered thermodynamical snow model for radiance assimilation. *IEEE Transactions on Geoscience and Remote Sensing*, 49(8):2828–2837, 2011.

[214] L. Tsang, C.-T. T. Chen, A. T. C. Chang, J. Guo, and K. H. K.-H. Ding. Dense media radiative transfer theory based on quasicrystalline approximation with applications to passive microwave remote sensing of snow. *Radio Science*, 35(3):731–749, 2000. ISSN 00486604. doi: 10.1029/1999RS002270.

[215] L. Tsang, J. Pan, D. Liang, Z. Li, D. W. Cline, and Y. Tan. Modeling active microwave remote sensing of snow using dense media radiative transfer (dmrt) theory with multiple-scattering effects. *IEEE Transactions on Geoscience and Remote Sensing*, 45(4):990–1004, 2007.

[216] F. T. Ulaby and R. Jedlicka. Microwave dielectric properties of plant materials. *IEEE Transactions on Geoscience and Remote Sensing*, (4):406–415, 1984.

[217] F. T. Ulaby and W. H. Stiles. The active and passive microwave response to snow parameters: 2. water equivalent of dry snow. *Journal of Geophysical Research: Oceans*, 85(C2):1045–1049, 1980.

[218] F. T. Ulaby, R. K. Moore, and A. K. Fung. *Microwave Remote Sensing-Active and Passive-Volume I-Microwave Remote Sensing Fundamentals and Radiometry (v. 1)*. Addison-Wesley Reading, MA, 1981.

[219] F. T. Ulaby, K. Sarabandi, K. Mcdonald, M. Whitt, and M. C. Dobson. Michigan microwave canopy scattering model. *International Journal of Remote Sensing*, 11 (7):1223–1253, 1990.

[220] B. J. Vander Jagt, M. T. Durand, S. A. Margulis, E. J. Kim, and N. P. Molotch. The effect of spatial variability on the sensitivity of passive microwave measurements to snow water equivalent. *Remote Sensing of Environment*, 136:163–179, 2013.

[221] M. M. Verstraete, B. Pinty, and R. B. Myneni. Potential and limitations of information extraction on the terrestrial biosphere from satellite remote sensing. *Remote Sensing of Environment*, 58(2):201–214, 1996.

[222] V. Vionnet, E. Brun, S. Morin, A. Boone, S. Faroux, P. Le Moigne, E. Martin, and J. Willemet. The detailed snowpack scheme crocus and its implementation in surfex v7. 2. *Geoscientific Model Development*, 5:773–791, 2012.

[223] C. Vuyovich and J. M. Jacobs. Snowpack and runoff generation using amsr-e passive microwave observations in the upper helmand watershed, afghanistan. *Remote sensing of environment*, 115(12):3313–3321, 2011.

[224] C. M. Vuyovich, J. M. Jacobs, C. A. Hiemstra, and E. J. Deeb. Effect of spatial variability of wet snow on modeled and observed microwave emissions. *Remote Sensing of Environment*, 198:310–320, 2017.

[225] Q. Wang, W. Shi, and P. M. Atkinson. Area-to-point regression kriging for pan-sharpening. *ISPRS journal of photogrammetry and remote sensing*, 114:151–165, 2016.

[226] U. Wegmuller and C. Matzler. Rough bare soil reflectivity model. *IEEE Transactions on Geoscience and Remote Sensing*, 37(3):1391–1395, 1999.

[227] B. Wen, L. Tsang, D. P. Winebrenner, and A. Ishimaru. Dense medium radiative transfer theory: comparison with experiment and application to microwave remote sensing and polarimetry. *IEEE Transactions on Geoscience and Remote Sensing*, 28 (1):46–59, 1990.

[228] F. J. Wentz and T. Meissner. Supplement 1 algorithm theoretical basis document for amsr-e ocean algorithms. *NASA: Santa Rosa, CA, USA*, 2007.

[229] A. Wiesmann and C. Mätzler. Documentation for memls 98.2, microwave emission model of layered snowpacks. *Microwave Dept., Inst. Applied Physics, Univ. Bern, Bern, Switzerland, Res. Rep*, (98-2), 1998.

[230] A. Wiesmann and C. Mätzler. Microwave emission model of layered snowpacks. *Remote Sensing of Environment*, 70(3):307–316, 1999.

[231] J.-P. Wigneron, Y. Kerr, P. Waldteufel, K. Saleh, M.-J. Escorihuela, P. Richaume, P. Ferrazzoli, P. De Rosnay, R. Gurney, J.-C. Calvet, et al. L-band microwave emission of the biosphere (l-meb) model: Description and calibration against experimental data sets over crop fields. *Remote Sensing of Environment*, 107(4):639–655, 2007.

[232] M. Woo, A. Walker, D. Yang, and B. Goodison. Pixel-scale ground snow survey for passive microwave study of the arctic snow cover. In *Proc. 52nd Eastern Snow Conference*, pages 51–57, 1995.

[233] M.-k. Woo and K. L. Young. Hydrology of a small drainage basin with polar oasis environment, fosheim peninsula, ellesmere island, canada. *Permafrost and Periglacial Processes*, 8(3):257–277, 1997.

[234] M.-k. Woo, R. Heron, P. Marsh, and P. Steer. Comparison of weather station snowfall with winter snow accumulation in high arctic basins. *Atmosphere-Ocean*, 21(3):312–325, 1983.

[235] Working-Group-On-Snow-Classification., S. Colbeck, and E. Morris. The international classification for seasonal snow on the ground. prepared by the working group. chairman: S. colbeck. Technical report, 1990.

[236] X. Xiao, T. Zhang, X. Zhong, W. Shao, and X. Li. Support vector regression snow-depth retrieval algorithm using passive microwave remote sensing data. *Remote Sensing of Environment*, 210:48–64, 2018.

[237] Y. Xue, B. A. Forman, and R. H. Reichle. Estimating snow mass in north america through assimilation of advanced microwave scanning radiometer brightness temperature observations using the catchment land surface model and support vector machines. *Water Resources Research*, 54(9):6488–6509, 2018.